

**Flanders**  
State of  
the Art

14\_147\_3  
FHR reports

# Agenda for the Future – Historical evolution of tides and morphology in the Scheldt Estuary

Subreport 3  
Calibration and validation of historical hydrodynamic models

DEPARTMENT  
MOBILITY &  
PUBLIC  
WORKS

[www.flandershydraulicsresearch.be](http://www.flandershydraulicsresearch.be)

# Agenda for the Future – Historical evolution of tides and morphology in the Scheldt Estuary

## Subreport 3 – Calibration and validation of historical hydrodynamic models

Stark, J.; Maximova, T.; Dujardin, A.; Smolders, S.; Vandenbruwaene, W.; Mostaert, F.

Legal notice

Flanders Hydraulics Research is of the opinion that the information and positions in this report are substantiated by the available data and knowledge at the time of writing.  
 The positions taken in this report are those of Flanders Hydraulics Research and do not reflect necessarily the opinion of the Government of Flanders or any of its institutions.  
 Flanders Hydraulics Research nor any person or company acting on behalf of Flanders Hydraulics Research is responsible for any loss or damage arising from the use of the information in this report.

Copyright and citation

© The Government of Flanders, Department of Mobility and Public Works, Flanders Hydraulics Research 2020  
 D/2020/3241/27

This publication should be cited as follows:

**Stark, J.; Maximova, T.; Dujardin, A.; Smolders, S.; Vandenbruwaene, W.; Mostaert, F. (2020).** Agenda for the Future – Historical evolution of tides and morphology in the Scheldt Estuary: Subreport 3 – Calibration and validation of historical hydrodynamic models. Version 3.0. FHR Reports, 14\_147\_3. Flanders Hydraulics Research: Antwerp.

Reproduction of and reference to this publication is authorized provided the source is acknowledged correctly.

Document identification

Customer:	VNSC	Ref.:	WL2020R14_147_3
Keywords (3-5):	Tides, morphology, Long-term evolution, Scheldt Estuary, Numerical modelling		
Text (p.):	59	Appendices (p.):	37
Confidentiality:	<input checked="" type="checkbox"/> No	<input checked="" type="checkbox"/> Available online	

Author(s):	Stark, J.; Maximova, T.; Dujardin, A.
------------	---------------------------------------

Control

	Name	Signature
Reviser(s):	Smolders, S.	Getekend door: Sven Smolders (Signature) Getekend op: 2020-01-30 14:53:56 +01:00 Reden: Ik keur dit document goed <i>Sven Smolders</i>
Project leader:	Vandenbruwaene, W.	Getekend door: Wouter Vandenbruwaene (S) Getekend op: 2020-01-23 12:11:26 +01:00 Reden: Ik keur dit document goed <i>Wouter Vandenbruwaene</i>

Approval

Head of Division:	Mostaert, F.	Getekend door: Frank Mostaert (Signature) Getekend op: 2020-01-30 14:40:09 +01:00 Reden: Ik keur dit document goed <i>Frank Mostaert</i>
-------------------	--------------	---



## Abstract

This study on historical evolution of tides and morphology in the Scheldt Estuary is part of the Agenda for the Future research program (AvdT studie: *'historische evolutie getij en morfologie Schelde estuarium'*). The general objective of this AvdT study is to improve insights on the interactions between changes in estuarine morphology and changes in estuarine tidal hydrodynamics. This subreport handles the calibration and validation of five historical models (i.e., for 1930, 1960, 1980, 2001 and 2013) that are constructed in TELEMAC-3D, making use of the available Scaldis model of the Scheldt Estuary and the Belgian coastal zone. The model mesh of this Scaldis model is adapted to include historical tidal branches and intertidal areas, as well as present and future flood control areas. The model calibration consists of simultaneous adjustments of the bottom friction coefficients in the five models to obtain the friction field with the best overall performance. The historical models are then used to compute tidal characteristics, with a special focus on characteristics that could not be obtained from historical water level measurements, such as flow velocities, tidal discharges, tidal prisms and tidal asymmetry. Ultimately, it is intended that the historical models are used to assess the hydrodynamic impact of specific morphological developments or geometrical changes, using scenario analyses.



# Contents

Abstract .....	III
Contents .....	V
List of Tables .....	VII
List of Figures.....	VIII
1 Introduction.....	1
1.1 Study background.....	1
1.2 Report outline.....	2
1.3 Units and reference plane .....	2
2 Available measurement data.....	3
2.1 Water levels.....	3
2.2 Discharges.....	4
3 Continental shelf model .....	5
3.1 Continental Shelf Model (CSM) .....	5
3.2 Zuidelijke Noordzee Model (ZUNO) .....	6
4 Scaldis model.....	7
4.1 Software .....	7
4.2 Model grid .....	7
4.3 Topo-bathymetry.....	8
4.4 Bottom Friction.....	11
4.5 Salinity .....	11
4.6 Boundary conditions.....	12
4.6.1 Selection of simulation periods .....	12
4.6.2 Upstream discharge boundary .....	16
4.6.3 Downstream water level boundary .....	17
4.6.4 Correction of the water level boundary conditions from the CSM-ZUNO model.....	18
4.7 Model settings.....	22
5 Model calibration .....	23
5.1 Methodology .....	23
5.2 Initial model results with the Scaldis2013 bottom friction field .....	25
5.3 Model calibration based on bottom friction adjustments .....	27
6 Model validation.....	34

6.1	1930 model.....	34
6.2	1960 model.....	34
6.3	1980 model.....	36
6.4	2001 model.....	37
6.5	2013 model.....	37
6.6	Discussion of the model performance .....	41
7	Tidal characteristics .....	42
7.1	Vertical tide .....	43
7.2	Horizontal tide .....	45
7.3	Tidal wave celerity.....	47
7.4	Tidal asymmetry .....	50
8	Discussion and conclusions .....	53
8.1	Model performance.....	53
8.2	Historical development of tidal characteristics.....	54
8.3	Outlook.....	56
9	References.....	57
10	Appendices .....	A1
10.1	Grid adaptation.....	A2
10.2	Sensitivity Analysis: grid adaptation.....	A7
10.3	Sensitivity Analysis: effect of discharge at Bath .....	A9
10.4	Initial model performance with the Scaldis2013 bottom friction field.....	A11
10.5	Evaluation of peak discharges in simulation period.....	A16
10.6	Results of calibration runs: RMSE of HW, LW, $T_{HW}$ and $T_{LW}$ .....	A20
10.7	Sensitivity analysis: viscosity coefficient .....	A35

## List of Tables

Table 1 – Water level stations with available measurements.....	4
Table 2 – Source datasets for topo-bathymetrical maps. ....	8
Table 3 – Overview of the historical ecotopes and elevation classes assigned to them. ....	9
Table 4 – Mean spring tidal range and mean neap tidal range at Vlissingen used as reference for each period. .....	14
Table 5 – Mean high water level, mean low water level, mean sea level (calculated from high and low waters only) and mean tidal range for the selected simulation periods and yearly averages. ....	15
Table 6 – Applied model settings .....	22
Table 7 – Calibration parameters used in cost function.....	24
Table 8 – Weight of tidal stations in cost calculation per estuarine section.....	24
Table 9 – Manning coefficients per friction zone used in calibration runs. ....	28
Table 10 – Outcome cost function for the Western Scheldt friction zone.....	29
Table 11 – Outcome cost function for the Lower Sea Scheldt friction zone .....	30
Table 12 – Outcome cost function for the Upper Sea Scheldt friction zone.....	31
Table 13 – Outcome cost function equally averaged over the five historical models and over all tidal stations. .....	33
Table 14 – Overview of model simulations for sensitivity analysis of diffusion coefficients. ....	A36

## List of Figures

Figure 1 – Water level and discharge stations .....	3
Figure 2 – CSM model grid (in WGS84) .....	5
Figure 3 – ZUNO model grid .....	6
Figure 4 – Model domain.....	7
Figure 5 – Historical ecotope map of the Upper Sea Scheldt and Durme river for 1930.....	10
Figure 6 – Historical ecotope map of the Upper Sea Scheldt and Durme river for 1960.....	10
Figure 7 – Map of the Manning’s friction coefficients in the calibrated Scaldis2013 model.....	11
Figure 8 – Initial salinity field.....	12
Figure 9 – Difference between measured and modelled high- and low water levels for each of the five years. .....	13
Figure 10 – Cumulative distribution of tidal amplitudes at Vlissingen for the period 2001-2010, with the average spring tidal amplitude and average neap tidal amplitude according to Vanlierde et al. (2016) indicated in red.....	14
Figure 11 – Input discharge conditions at Merelbeke or Gentbrugge (Upper Sea Scheldt) for the five historical models .....	16
Figure 12 – Input discharge conditions at Dendermonde (Dender) for the five historical models .....	16
Figure 13 – Input discharge conditions at the Zenne for the five historical models.....	16
Figure 14 – Input discharge conditions at the Dijle for the five historical models.....	17
Figure 15 – Input discharge conditions at the Grote Nete and Kleine Nete (combined) for the five historical models .....	17
Figure 16 – Nesting of Scaldis model in ZUNO. ....	18
Figure 17 – Difference between measured and modelled high- and low water levels at Vlissingen for the 1930 model before (top) and after (bottom) the additional surge component was implemented. ....	19
Figure 18 – Difference between measured and modelled high- and low water levels at Vlissingen for the 1960 model before (top) and after (bottom) the additional surge component was implemented. ....	20
Figure 19 – Difference between measured and modelled high- and low water levels at Vlissingen for the 1980 model before (top) and after (bottom) the additional surge component was implemented. ....	20
Figure 20 – Difference between measured and modelled high- and low water levels at Vlissingen for the 2001 model before (top) and after (bottom) the additional surge component was implemented. ....	21
Figure 21 – Difference between measured and modelled high- and low water levels at Vlissingen for the 2013 model before (top) and after (bottom) the additional surge component was implemented. ....	21
Figure 22 – Map of the friction zones used for the stepwise calibration of the historical models.....	27
Figure 23 – Outcome of the cost function for calibration runs cal01, cal02 and cal03 (compared to run c2) in which the bottom friction coefficients in the entire estuary are varied.....	29

Figure 24 – Outcome of the cost function for calibration runs cal11, cal12, cal13, cal14, cal15 and cal16 (compared to run cal01) in which the bottom friction coefficients in the Lower and Upper Sea Scheldt are varied.....	30
Figure 25 – Outcome of the cost function for calibration runs cal21, cal22, cal23, cal24 and cal25 (compared to run cal14) in which the bottom friction coefficients in the Upper Sea Scheldt are varied.....	31
Figure 26 – Outcome of the cost function for calibration runs cal01, cal14 and cal25 relative to initial model simulation c2. ....	33
Figure 27 – HW BIAS, LW BIAS, THW BIAS and TLW BIAS for the 1930 model with the calibrated friction field from simulation cal25.....	35
Figure 28 – HW BIAS, LW BIAS, THW BIAS and TLW BIAS for the 1960 model with the calibrated friction field from simulation cal25.....	36
Figure 29 – HW BIAS, LW BIAS, THW BIAS and TLW BIAS for the 1980 model with the calibrated friction field from simulation cal25.....	38
Figure 30 – HW BIAS, LW BIAS, THW BIAS and TLW BIAS for the 2001 model with the calibrated friction field from simulation cal25.....	39
Figure 31 – HW BIAS, LW BIAS, THW BIAS and TLW BIAS for the 2013 model with the calibrated friction field from simulation cal25.....	40
Figure 32 – Locations and cross-sections at which tidal characteristics are computed .....	42
Figure 33 – Modelled historical development in mean high water level (top), mean low water level (mid) and mean tidal range (bottom). ....	44
Figure 34 – Modelled historical development in mean tidal prism. ....	45
Figure 35 – Modelled historical development in mean cross-sectional averaged flood velocities (top) and maximum cross-sectional averaged ebb-velocities (bottom) for mean tide. ....	46
Figure 36 – Modelled historical development in maximum cross-sectional averaged flood velocities (top) and maximum cross-sectional averaged ebb-velocities (bottom) for mean tide. ....	47
Figure 37 – Modelled historical development in mean tidal propagation for high tide (top) and low tide (bottom), expressed as the phase difference at each location with Vlissingen.....	48
Figure 38 – Modelled historical development in mean tidal wave celerity for high tide (top) and low tide (bottom), based on the high- and low water time-differences between downstream and upstream neighboring stations.....	49
Figure 39 – Evolution of the observed historical development of the tidal wave celerity of high tide (top) and low tide (bottom) with the model results plotted along with them. ....	49
Figure 40 – Modelled historical development in mean tidal asymmetry based on the ratio between the duration of the falling and rising tide (top), based on the ratio between peak cross-sectional averaged flood and ebb velocities (mid) and based on the third-order velocity moment $\gamma_0$ (bottom). ....	51
Figure 41 – Evolution of the observed historical development of the vertical tidal asymmetry based on the duration of the falling and rising tide in the Western Scheldt and Lower Sea Scheldt, with the model results plotted along with them.....	52
Figure 42 – Evolution of the observed historical development of the vertical tidal asymmetry based on the duration of the falling and rising tide in the Upper Sea Scheldt, with the model results plotted along with them. ....	52
Figure 43 – Model grid for the downstream part of the Western Scheldt .....	A2

Figure 44 – Model grid for the upstream part of the Western Scheldt and Lower Sea Scheldt .....	A2
Figure 45 – Model grid for the Sea Scheldt, Durme and Rupel .....	A3
Figure 46 – Model grid for the Upper Sea Scheldt .....	A3
Figure 47 – Model grid for the Durme.....	A4
Figure 48 – Bathymetry of the Durme in 1930.....	A4
Figure 49 – Bathymetry of the Durme in 1960.....	A5
Figure 50 – Model grid for the Rupel (upstream Wintam).....	A5
Figure 51 – Bathymetry of the Rupel upstream Wintam in 1930 .....	A6
Figure 52 – Bathymetry of the Rupel upstream Wintam in 2001 .....	A6
Figure 53 – Average water level difference along the estuary between a model simulation with the newly adapted grid (newgrid) and the original grid (r2d_v20_2013).....	A7
Figure 54 – Average high water level difference along the estuary between a model simulation with the newly adapted grid (newgrid) and the original grid (r2d_v20_2013). .....	A8
Figure 55 – Average low water level difference along the estuary between a model simulation with the newly adapted grid (newgrid) and the original grid (r2d_v20_2013). .....	A8
Figure 56 – Average effect of omitting the discharge at Bath on water level time series along the estuary. ....	A9
Figure 57 – Average effect of omitting the discharge at Bath on water level time series along the estuary. ....	A10
Figure 58 – Average effect of omitting the discharge at Bath on water level time series along the estuary. ....	A10
Figure 59 – HWL BIAS (top) and LWL BIAS (bottom) for the 1930 model with the Scaldis2013 friction field. ....	A11
Figure 60 – HWL BIAS (top) and LWL BIAS (bottom) for the 1960 model with the Scaldis2013 friction field. ....	A11
Figure 61 – HWL BIAS (top) and LWL BIAS (bottom) for the 1980 model with the Scaldis2013 friction field. ....	A12
Figure 62 – HWL BIAS (top) and LWL BIAS (bottom) for the 2001 model with the Scaldis2013 friction field. ....	A12
Figure 63 – HWL BIAS (top) and LWL BIAS (bottom) for the 2013 model with the Scaldis2013 friction field. ....	A13
Figure 64 – THW BIAS (top) and TLW BIAS (bottom) for the 1930 model with the Scaldis2013 friction field. ....	A13
Figure 65 – THW BIAS (top) and TLW BIAS (bottom) for the 1960 model with the Scaldis2013 friction field. ....	A14
Figure 66 – THW BIAS (top) and TLW BIAS (bottom) for the 1980 model with the Scaldis2013 friction field. ....	A14
Figure 67 – THW BIAS (top) and TLW BIAS (bottom) for the 2001 model with the Scaldis2013 friction field. ....	A15

Figure 68 – THW BIAS (top) and TLW BIAS (bottom) for the 2013 model with the Scaldis2013 friction field. .... A15

Figure 69 – Discharge induced surge signal at Wetteren for the 1930 simulation period, calculated as the difference between the surge signal at Wetteren and the surge signal at the more downstream located tidal station of Antwerpen. .... A17

Figure 70 – Discharge induced surge signal at Wetteren for the 1960 simulation period, calculated as the difference between the surge signal at Wetteren and the surge signal at the more downstream located tidal station of Antwerpen. .... A17

Figure 71 – Discharge induced surge signal at Wetteren for the 1980 simulation period, calculated as the difference between the surge signal at Wetteren and the surge signal at the more downstream located tidal station of Antwerpen. .... A18

Figure 72 – Discharge induced surge signal at Wetteren for the 2001 simulation period, calculated as the difference between the surge signal at Wetteren and the surge signal at the more downstream located tidal station of Antwerpen. .... A18

Figure 73 – Discharge induced surge signal at Wetteren for the 2013 simulation period, calculated as the difference between the surge signal at Wetteren and the surge signal at the more downstream located tidal station of Antwerpen. .... A19

Figure 74 – HWL RMSE (top) and LWL RMSE (bottom) for calibration runs cal01-cal03 with the 1930 model. .... A20

Figure 75 – THW RMSE (top) and TLW RMSE (bottom) for calibration runs cal01-cal03 with the 1930 model. .... A20

Figure 76 – HWL RMSE (top) and LWL RMSE (bottom) for calibration runs cal01-cal03 with the 1960 model. .... A21

Figure 77 – THW RMSE (top) and TLW RMSE (bottom) for calibration runs cal01-cal03 with the 1960 model. .... A21

Figure 78 – HWL RMSE (top) and LWL RMSE (bottom) for calibration runs cal01-cal03 with the 1980 model. .... A22

Figure 79 – THW RMSE (top) and TLW RMSE (bottom) for calibration runs cal01-cal03 with the 1980 model. .... A22

Figure 80 – HWL RMSE (top) and LWL RMSE (bottom) for calibration runs cal01-cal03 with the 2001 model. .... A23

Figure 81 – THW RMSE (top) and TLW RMSE (bottom) for calibration runs cal01-cal03 with the 2001 model. .... A23

Figure 82 – HWL RMSE (top) and LWL RMSE (bottom) for calibration runs cal01-cal03 with the 2013 model. .... A24

Figure 83 – THW RMSE (top) and TLW RMSE (bottom) for calibration runs cal01-cal03 with the 2013 model. .... A24

Figure 84 – HWL RMSE (top) and LWL RMSE (bottom) for calibration runs cal01 and cal11-cal16 with the 1930 model. .... A25

Figure 85 – THW RMSE (top) and TLW RMSE (bottom) for calibration runs cal01 and cal11-cal16 with the 1930 model. .... A25

Figure 86 – HWL RMSE (top) and LWL RMSE (bottom) for calibration runs cal01 and cal11-cal16 with the 1960 model. .... A26

Figure 87 – THW RMSE (top) and TLW RMSE (bottom) for calibration runs cal01 and cal11-cal16 with the 1960 model.....	A26
Figure 88 – HWL RMSE (top) and LWL RMSE (bottom) for calibration runs cal01 and cal11-cal16 with the 1980 model.....	A27
Figure 89 – THW RMSE (top) and TLW RMSE (bottom) for calibration runs cal01 and cal11-cal16 with the 1980 model.....	A27
Figure 90 – HWL RMSE (top) and LWL RMSE (bottom) for calibration runs cal01 and cal11-cal16 with the 2001 model.....	A28
Figure 91 – THW RMSE (top) and TLW RMSE (bottom) for calibration runs cal01 and cal11-cal16 with the 2001 model.....	A28
Figure 92 – HWL RMSE (top) and LWL RMSE (bottom) for calibration runs cal01 and cal11-cal16 with the 2013 model.....	A29
Figure 93 – THW RMSE (top) and TLW RMSE (bottom) for calibration runs cal01 and cal11-cal16 with the 2013 model.....	A29
Figure 94 – HWL RMSE (top) and LWL RMSE (bottom) for calibration runs cal01, cal14 and cal21-cal25 with the 1930 model. ....	A30
Figure 95 – THW RMSE (top) and TLW RMSE (bottom) for calibration runs cal01, cal14 and cal21-cal25 with the 1930 model. ....	A30
Figure 96 – HWL RMSE (top) and LWL RMSE (bottom) for calibration runs cal01, cal14 and cal21-cal25 with the 1960 model. ....	A31
Figure 97 – THW RMSE (top) and TLW RMSE (bottom) for calibration runs cal01, cal14 and cal21-cal25 with the 1960 model. ....	A31
Figure 98 – HWL RMSE (top) and LWL RMSE (bottom) for calibration runs cal01, cal14 and cal21-cal25 with the 1980 model. ....	A32
Figure 99 – THW RMSE (top) and TLW RMSE (bottom) for calibration runs cal01 and cal11-cal16 with the 1980 model.....	A32
Figure 100 – HWL RMSE (top) and LWL RMSE (bottom) for calibration runs cal01, cal14 and cal21-cal25 with the 2001 model. ....	A33
Figure 101 – THW RMSE (top) and TLW RMSE (bottom) for calibration runs cal01, cal14 and cal21-cal25 with the 2001 model. ....	A33
Figure 102 – HWL RMSE (top) and LWL RMSE (bottom) for calibration runs cal01, cal14 and cal21-cal25 with the 2013 model. ....	A34
Figure 103 – THW RMSE (top) and TLW RMSE (bottom) for calibration runs cal01, cal14 and cal21-cal25 with the 2013 model. ....	A34
Figure 104 – Impact of variations in the viscosity coefficient on HWL BIAS (top) and LWL BIAS (bottom) for calibration runs cal25 and sa31-sa34 with the 1930 model.....	A37

# 1 Introduction

## 1.1 Study background

This study forms Subreport 3 of the Agenda for the Future study: ‘historical evolution of tides and morphology in the Scheldt Estuary (AvdT studie: *‘historische evolutie getij en morfologie Schelde estuarium’*). The general objective of this AvdT study is to improve insights on the interactions between changes in estuarine morphology and changes in estuarine tidal hydrodynamics. This should aid (morphological) management of the estuary by obtaining a better understanding of the hydro-morphodynamic functioning of the estuarine system as a whole. Subreport 3 describes the calibration of the historical models that are used to assess the impact of morphological changes on tidal hydrodynamics in the Scheldt Estuary. In particular, five historical models are constructed (i.e., for 1930, 1960, 1980, 2001 and 2013) in TELEMAC-3D based on the previously validated Scaldis 2013 TELEMAC-3D model (Smolders et al., 2016).

Knowledge on the influence of morphological changes on tidal hydrodynamics in the Scheldt Estuary is of crucial importance for estuarine (morphological) management. Human-induced estuarine changes (e.g. embankments, de-embankments, dredging, sand mining, navigation channel realignments, etc.) directly or indirectly alter the estuarine morphology and geometry, potentially inducing hydrodynamic changes in tidal range, tidal prism and tidal asymmetry. Changes in tidal characteristics may on their hand have an impact on the estuarine functionality. For example, changes in high water levels can directly be related to safety against flooding, while tidal asymmetry is of particular importance to sediment transport and hence the estuarine morphological development. Other functions, related to the accessibility of the ports along the estuary or the environmental status of the estuary, are also influenced by tidal characteristics.

### Historical changes

Historical human-induced impacts on the estuarine morphology of the Scheldt Estuary typically consisted of stepwise embankments of former intertidal areas (predominantly in the Western Scheldt) as well as channel straightening (in the Sea Scheldt), while deepening and dredging of the navigation channels occurred frequently from the 1970s onward (e.g. Jeuken et al., 2007; Van Braeckel et al., 2012; Vandenbruwaene et al., 2020). Since the 1970s, the navigation channel has been enlarged and deepened three times during the first (1970-1976), second (1997-1998) and third enlargement (2008-2011). Large quantities of sediment were dredged from the estuarine channels in the Western Scheldt and Sea Scheldt for these channel enlargements. The dredged sediment was removed from the estuarine system during the first enlargement, whereas it was reallocated within the estuary from the second enlargement onwards. Systematical sand mining has also been common practice from the 1950s onwards (Jeuken et al., 2007; Van Braeckel et al., 2012). In conclusion, historical human-induced changes to the estuarine morphology first mainly resulted from changes to the estuary geometry, whereas the last decades mainly consisted of direct alterations to the estuarine morphology.

More recently, geometrical changes to the estuary have been enforced again as restoration of intertidal areas along the estuary is implemented as a strategy to re-establish the coastal defense value as well as the ecological functions provided by tidal flats and tidal marshes. Several de-embankments were recently implemented or will be realized in the upcoming years. Besides, restoration of intertidal areas along the Belgian part of the Scheldt Estuary is part of the Sigma-plan and includes the creation of flood control areas that are designed with specific inlet and outlet culvert systems to generate a so-called controlled reduced tide, which means that only limited tidal exchange between the estuary and the flood control area is allowed to optimize both the flood defense value as well as the ecological functioning (e.g., Cox et al., 2006; Maris et al., 2007).

The morphological evolution of the estuary over the last century is assessed in more detail in Subreport 2 of this study (Vandenbruwaene et al., 2020). In particular, Subreport 2 describes the historical development of tidal characteristics in the Scheldt Estuary in comparison to the historical morphological changes based on an extensive data-analysis. Furthermore, the historical tidal characteristics along the Lower Sea Scheldt and Upper Sea Scheldt are presented for the period 1888-2013 in Subreport 1 of this study (Vandenbruwaene et al., 2019).

### Previous modelling studies

Regarding the hydrodynamic impact of large-scale historical morphological changes, the effect of historical channel realignments and of fictitious de-embankments of historical branches and marshes along the Scheldt Estuary has been assessed in previous modelling studies (e.g. Jeuken et al., 2004; Coen et al., 2008; Maximova et al., 2010). These studies showed that the presence of historical estuarine areas (i.e., former intertidal storage areas and side-branches) generally leads to a reduction in tidal range and high water levels along the estuary. They also indicated that the presence of historical estuarine areas generally increases the tidal prism downstream and reduces the tidal prism upstream of the additional estuarine areas. Conversely, another recent modelling study in which fictitious intertidal area changes were implemented in the Scheldt Estuary suggested that adding intertidal storage in the upstream part of the estuary may induce a tidal prism decrease far downstream as a result of a second-order effect due to reduced tidal range (Stark et al., 2017). This latter study also showed that the impact of intertidal areas on tidal asymmetry largely depends on intertidal area elevation and hence may alter over time as these areas grow vertically. Furthermore, the decadal scale hydro-morphological modelling study by Jeuken et al. (2004) showed that the initial impact of newly created intertidal areas on tidal asymmetry and sediment transport through the estuarine channels may be different from or even opposite of the decadal scale impact.

## 1.2 Report outline

The hydrodynamic data used for the model calibration and validation is briefly presented in Section 2. Section 3 describes the coastal shelf model and North Sea model that are used to generate the offshore boundary conditions for the Scaldis TELEMAC-3D model. A description of the Scaldis model and the used model input, including the implemented topo-bathymetries and the selection of the boundary conditions, is given in Section 4. The simultaneous calibration of the five historical models is presented in Section 5, after which the model is validated in Section 6. Finally, Section 7 describes the tidal characteristics that could be obtained with the numerical models, including historical tidal prisms and tidal asymmetries along the estuary.

## 1.3 Units and reference plane

Water levels and bottom elevations are expressed in meter TAW (Tweede Algemene Waterpassing). A bathymetric depth is defined as positive below the reference plane (0 m TAW), while water levels are positive above the reference plane. The horizontal coordinate system is RD Parijs.

## 2 Available measurement data

### 2.1 Water levels

Water level data at several tidal stations along the Scheldt estuary, including measured high and low waters, were received from the HIC department of Flanders Hydraulics Research for 1930, 1960, 1980, 2001 and 2013. Table 1 lists the stations for which measured high and low water levels are available. Figure 1 shows the location of these stations. All water level data were converted to m TAW.

Figure 1 – Water level and discharge stations

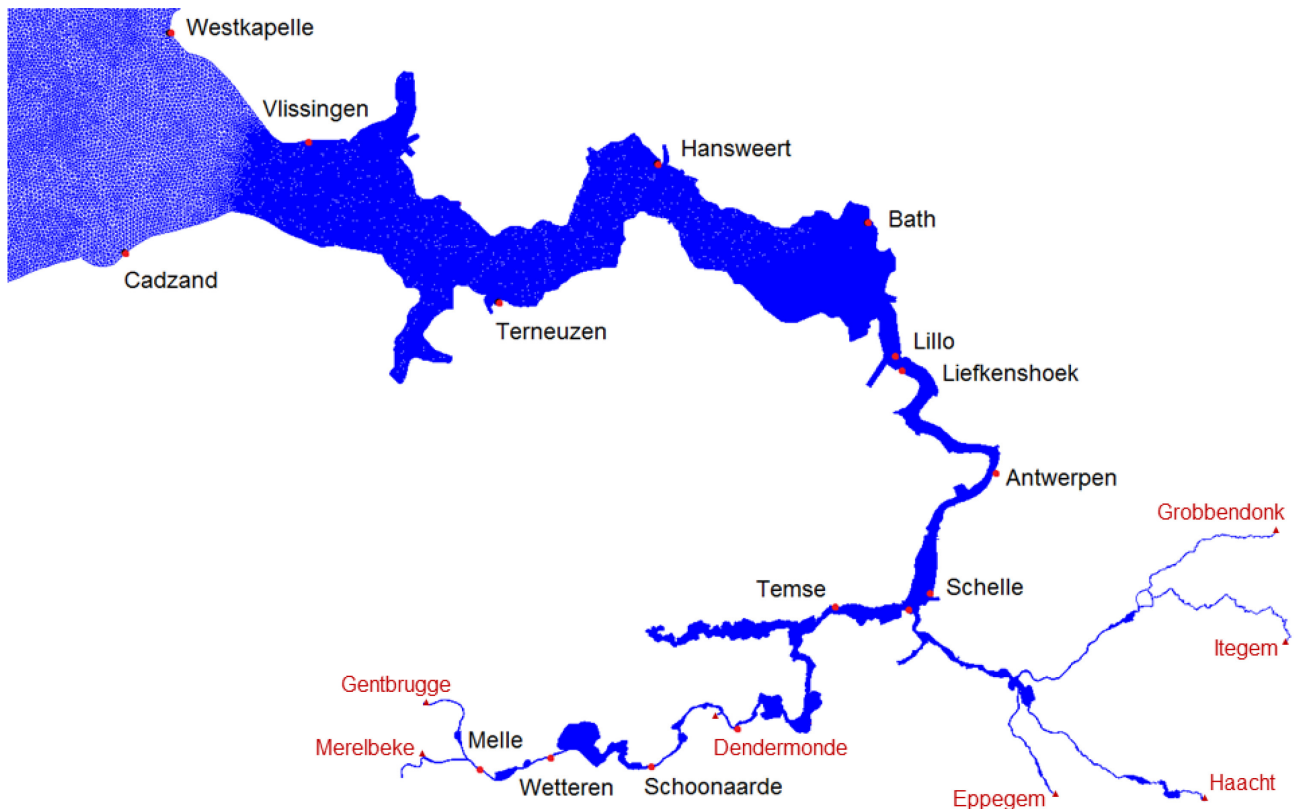


Table 1 – Water level stations with available measurements

Station	Year	Data source
<b>Vlissingen</b>	1930, 1960, 1980, 2001, 2013	<i>Hydrological Information Centre (HIC)</i>
<b>Terneuzen</b>	1930, 1960, 1980, 2001, 2013	
<b>Hansweert</b>	1930, 1960, 1980, 2001, 2013	
<b>Bath</b>	1930, 1960, 1980, 2001, 2013	
<b>Liefkenshoek / Lillo</b>	1960, 1980, 2001, 2013	
<b>Antwerpen</b>	1930, 1960, 1980, 2001, 2013	
<b>Schelle/Hingene</b>	1930, 1980, 2001	
<b>Temse</b>	1930, 1960, 2001, 2013	
<b>Dendermonde</b>	1930, 1960, 1980, 2001, 2013	
<b>Schoonaarde</b>	1930, 1960, 1980, 2001, 2013	
<b>Wetteren</b>	1930, 1960, 1980, 2001, 2013	
<b>Melle</b>	1930, 1980, 2001, 2013	

## 2.2 Discharges

Daily measured discharges are available (digitized) for the Upper Sea Scheldt (Melle), Zenne (Epepegem), Dijle (Haacht), Grote Nete (Itegem), Kleine Nete (Grobbendonk) and Dender (Dendermonde / Appels) tributaries from 1970 onwards.

In addition, daily measured discharges for the Upper Sea Scheldt (Gentbrugge), Zenne (Epepegem), Dijle (Haacht), Grote Nete (Itegem), Kleine Nete (Grobbendonk) and Dender (Dendermonde) are available for the period between 1-1-1954 until 1-4-1954 from a previous study (Dujardin et al., 2017).

The locations of the discharge measurements are also indicated in Figure 1.

## 3 Continental shelf model

### 3.1 Continental Shelf Model (CSM)

The Continental Shelf Model that is used to generate boundary conditions for the regional scale ZUNO-model has an orthogonal grid constructed from sphere coordinates in the spherical coordinate system ED50. It includes the continental shelf from 48° to 62.25° northern latitude and from 12° western longitude to 13° eastern longitude. The model includes the North sea, the Wadden Sea, Eems, Dollard, the Channel, the Keltic sea, the Irish sea, Skagerrak, Kattegat and is bordered by the Atlantic Ocean (Figure 2). The grid has resolution of 9.3 to 6.5 km in the west-east direction and 9.25 km in the south-north direction (Leyssen et al., 2012).

The model is driven at the outer ocean boundaries by astronomical water levels defined by 11 tidal components: M2, S2, N2, K2, O1, K1, Q1, P1, NU2, L2 and SA.

More information about the CSM model can be found in Leyssen et al. (2012) and Maximova et al. (2016).

---

Figure 2 – CSM model grid (in WGS84)

---



## 3.2 Zuidelijke Noordzee Model (ZUNO)

The southern North Sea (Zuidelijke Noordzee) model is a curvilinear model in the RD Parijs coordinate system. It includes the southern North Sea and the Channel, bounded by a northern boundary between Aberdeen (Great Britain) and Hanstholm (Denmark) and a southern boundary between Bournemouth (Great Britain) and Cherbourg (France) in the South-West (Figure 3). The model resolution is approximately 4.5 to 6 km along the English coast, 2.5 to 4 km in the Channel and the German Bight and 1 to 2 km along the Dutch coast (Leyssen et al., 2012).

The boundary conditions at the sea boundaries of the ZUNO model come from the CSM model. In particular, water levels calculated by the CSM model are implemented at corresponding boundary points of the ZUNO model without interpolation. In addition, there are 12 open river boundaries in ZUNO. Constant discharges are specified there for the harmonic runs.

More information about the ZUNO model and the nesting of the ZUNO model in the CSM model is given in Leyssen et al. (2012) and Maximova et al. (2016).

Harmonic CSM and ZUNO runs (without wind and with constant discharges) are performed for the different years. The same initial salinity field, calculated for 2013 through an elongated model run (see Maximova et al., 2016), is used in these runs. The ZUNO model runs are used to generate (harmonic) water level boundary conditions for the detailed Scaldis model of the Scheldt Estuary and to select a simulation period for each year (see Section 4). Surge effects are later on added artificially, by imposing a time-dependent surge based on water level differences between an initial Scaldis model run and tidal water level measurements at Vlissingen.

---

Figure 3 – ZUNO model grid



## 4 Scaldis model

### 4.1 Software

The hydrodynamic model for this project is developed in the TELEMAC modeling software (version V7P2). TELEMAC is a finite element model, in which the model domain is discretized into an unstructured grid of triangular elements. Therefore, it can relatively easily be locally refined in a specific area and the complex geometry of the study area can be taken into account.

More detailed information on the TELEMAC modelling system in general can be found in Hervouet (2007) or the TELEMAC user manual (see: <http://wiki.opentelemac.org>).

### 4.2 Model grid

The Scaldis model grid used in this report is largely adopted from the grid of the calibrated Scaldis model described in Smolders et al. (2016). However, all historical intertidal areas and tributaries that used to be or became part of the estuary (in the period from 1930 to 2013) are added to the grid (Figure 4). This way, the same grid can be used for all modelled years. In case a certain intertidal area or tributary was not part of the estuary in a certain year, a (very high) supratidal bathymetry is assigned to the area.

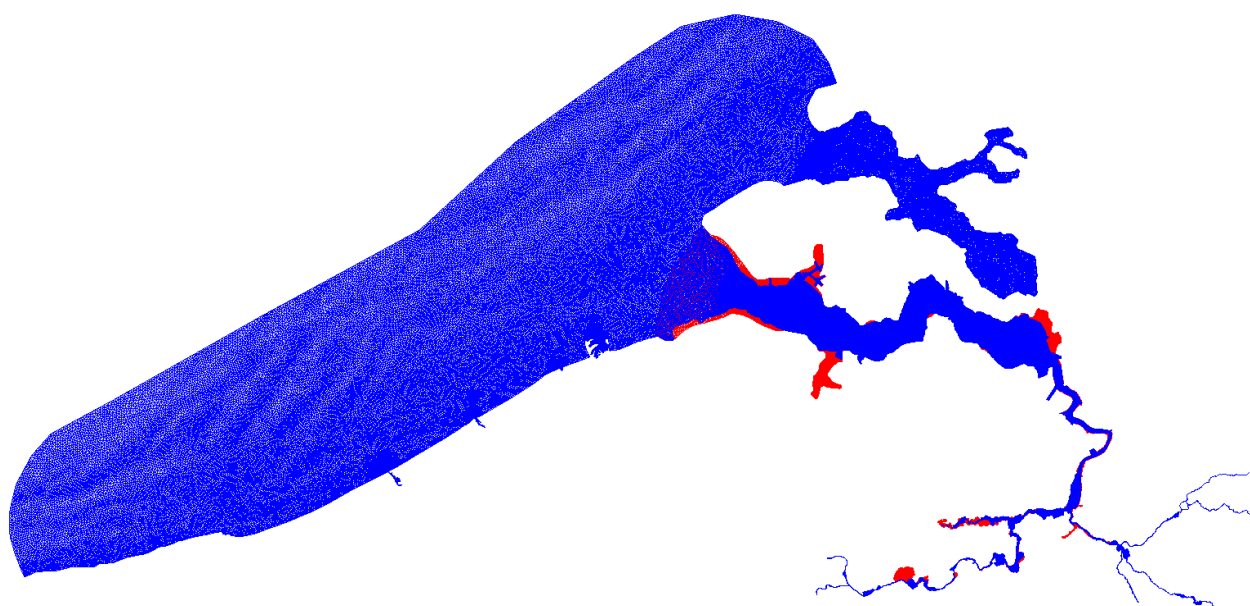
The adapted model grid used in this study consists of 600,977 nodes and 1,156,546 elements in 1 layer. There are 5 vertical layers in the 3D model, implying there are 3,004,885 nodes in total.

A more detailed overview of the adaptations to the model grid as well as a comparison of model results obtained with the original Scaldis grid and with the newly constructed grid used in this report is presented in Appendix 10.2. This comparison shows that the influence of altering the Scaldis mesh on the tidal propagation is negligible.

---

Figure 4 – Model domain (blue: original Scaldis model; red: adapted grid)

---



### 4.3 Topo-bathymetry

The topo-bathymetries of the Scheldt Estuary that are used in the historical models are presented in Subreport 2 of this study (Vandenbruwaene et al., 2020). This subreport also describes the construction of the 1930, 1960, 1980 and 2001 topo-bathymetries. Furthermore, the topo-bathymetry of the 2013 model is adopted from the already available Scaldis 2013 model presented by Smolders et al. (2016).

For the Western Scheldt, full topo-bathymetrical maps of the intertidal and supratidal parts are available for all historical models from 1930 up until 2013. For the Sea Scheldt however, full topo-bathymetric maps including the intertidal and supratidal areas are only available from 2000 onwards (i.e., topo-bathymetries for the 2001 and 2013 models). This implies that the historical elevation of intertidal areas in the remaining topo-bathymetries must be implemented differently. Therefore, historical ecotope maps published by the INBO (Van Braeckel et al., 2012) are used to assign elevations to intertidal areas in the historical topo-bathymetries for which no bathymetric data is available (i.e., topo-bathymetries for the 1930, 1960 and 1980 models). Figure 5 and Figure 6 show these historical ecotope maps for 1930 and 1960.

#### Data source

The bathymetrical data of the Sea Scheldt and the coastal zone were copied from the aMT GIS database and from the Flanders Hydraulics GIS database, although bathymetrical data of the Western Scheldt were originally provided by RWS (Table 2). Bathymetrical data of the offshore area and the Eastern Scheldt are adopted from the Scaldis2013 model in all historical models. The source datasets of this existing Scaldis 2013 model are given by Smolders et al., (2016).

Table 2 – Source datasets for topo-bathymetrical maps.

Year	Western Scheldt + mouth area	Sea Scheldt
1930	<ul style="list-style-type: none"> <li>• monding_wes_1938_rd_taw**</li> <li>• wes_bth_1931_rws_rds_nap**</li> </ul>	<ul style="list-style-type: none"> <li>• boz_bth_taw_mt_1930_5m*</li> <li>• bez_bth_taw_mt_1930_5m*</li> <li>• tbr_bth_taw_mt_1930_5m*</li> <li>• 1930 ecotope map (Van Braeckel et al., 2012)</li> </ul>
1960	<ul style="list-style-type: none"> <li>• monding_wes_1959_rd_taw**</li> <li>• wes_bth_1960_rws_rds_nap**</li> </ul>	<ul style="list-style-type: none"> <li>• Bezboz60taw*</li> <li>• tbr_bth_taw_mt_1960_5m*</li> <li>• 1960 ecotope map (Van Braeckel et al., 2012)</li> </ul>
1980	<ul style="list-style-type: none"> <li>• monding_wes_1980_rd_taw**</li> <li>• wes_bth_1980_rws_rds_nap**</li> </ul>	<ul style="list-style-type: none"> <li>• bez_bth_taw_mt_19801981_5m*</li> <li>• boz_bth_taw_mt_1980_5m*</li> <li>• tbr_bth_taw_mt_1980_5m*</li> <li>• 1960 + 2010 ecotope maps (Van Braeckel et al., 2012)</li> </ul>
2001	<ul style="list-style-type: none"> <li>• monding_wes_2001_rd_taw**</li> <li>• wes_bth_2001_rws_rds_nap**</li> </ul>	<ul style="list-style-type: none"> <li>• bez_bth_taw_mt_2002_5m*</li> <li>• boz_bth_taw_mt_2001_5m*</li> <li>• tbr_bth_taw_mt_19952000_1m*</li> </ul>
2013	see: Smolders et al. (2016)	

\* source: \\wm162458\data\GISdata\frame\bth\frame\_bth\_etr89utm31n.gdb

\*\* source: \\Masterarchief\tob\

## Assigning bottom elevations based on ecotope classes

To assign bottom elevations based on the habitat maps by Van Braeckel et al. (2012), the ecotope classes from these maps are first converted to elevation classes as is shown in Table 3. In this step, subtidal habitats are also included as an elevation class to obtain an accurate interpolation between the available bathymetric data and the assigned elevations based on habitat types afterwards. As there is no habitat map available for 1980, the boundaries between the various elevation classes are constructed artificially through linear interpolation between the boundaries in the habitat maps of 2010 and 1960 (i.e., the 1980 boundaries between ecotope classes are assumed at 2/5<sup>th</sup> of the distance between the 1960 and 2010 boundaries). Intertidal areas that were embanked between 1960 and 1980 are of course excluded from the topo-bathymetric maps.

Table 3 – Overview of the historical ecotopes and elevation classes assigned to them.

Ecotopes as defined by INBO (Dutch)	Ecotope as defined by INBO (English)	Assigned elevation class
‘Bedijkt schor’	‘Embanked marsh’	Marsh
‘Diep subtidaal’	‘Deep subtidal’	Subtidal
‘Gecontroleerd vloeisysteem’	‘Embanked cultivated flood system’	Levee / High
‘GOG’	‘Flood control area’	Levee / High
‘Matig diep subtidaal’	‘Less deep subtidal’	Subtidal
‘Ondiep subtidaal’	‘Shallow subtidal’	Subtidal
‘Open water vloeisysteem’	‘Open cultivated flood system’	High (or marsh)*
‘Schor’	‘Marsh’	Marsh
‘Slik’	‘Tidal flat’	Tidal flat
‘Vloeisysteem’	‘Cultivated flood system’	High (or marsh)*

*\*Areas that were identified as ‘cultivated flood system’ and ‘open cultivated flood system’ ecotopes are initially assigned to the ‘marsh’ elevation class. However, these areas were typically only subjected to tidal forcing occasionally during winter periods when temporary summer levees were breached and/or drainage gates were opened (Van Braeckel et al., 2012). As the calibration periods are all in summer (See: §4.6.1), when these flood systems were cultivated and not subjected to tidal forcing, a higher supratidal elevation is assigned to these areas for the model calibration in Section 5.*

Bottom level elevations are assigned at the boundaries between the various ecotope classes in Table 3, following a similar methodology as in Vandenbruwaene et al. (2013):

- 1) The boundaries between all subtidal elevation classes and the tidal flat elevation class are defined at the local MLWL on every 100 m.
- 2) For 1930, the ‘marsh’ elevation class and the boundaries between the ‘deep / shallow / less deep subtidal’ elevation classes and the ‘marsh’ elevation class or between the ‘tidal flat’ and ‘marsh’ elevation classes are defined at the local MHWL – 0.05 m (Van Braeckel, 2016).
- 3) For 1960, the ‘marsh’ elevation class and the boundaries between the ‘deep / shallow / less deep subtidal’ elevation classes and the ‘marsh’ elevation class or between the ‘tidal flat’ and ‘marsh’ elevation classes are defined at the local MHWL + 0.05 m (based on empirical data by Temmerman et al., 2003).
- 4) For 1980, the ‘marsh’ elevation class and the boundaries between the ‘deep / shallow / less deep subtidal’ elevation classes and the ‘marsh’ elevation class or between the ‘tidal flat’ and ‘marsh’ elevation classes are defined at the local MHWL + 0.1728 m (based on empirical data by Temmerman et al., 2003).
- 5) The ‘levee / high’ elevation class is assigned with a supratidal elevation and does not affect the hydrodynamic simulations.
- 6) The elevation contours as described above are interpolated on a 5 x 5 m grid of the entire estuary, including the subtidal areas, using inverse distance weighting as interpolation method. Hence, the historical tidal flat elevations are estimated based on interpolation between local MLWL (at the

subtidal edges of the tidal flats) and approximately local MHWL (at the marsh edge of the tidal flats). Historical marsh elevations are set constant to a level close to MHWL (similar levels as described in steps 2-4 above). The subtidal parts of these maps are only used to obtain a smooth transition with the available bathymetric maps of the subtidal parts of the estuary.

- 7) Finally, the elevation maps of the intertidal areas are merged with the available bathymetric data of the subtidal areas. This way, a smooth topo-bathymetry of the full estuary (intertidal and subtidal) is created for each year.

Figure 5 – Historical ecotope map of the Upper Sea Scheldt and Durme river for 1930.

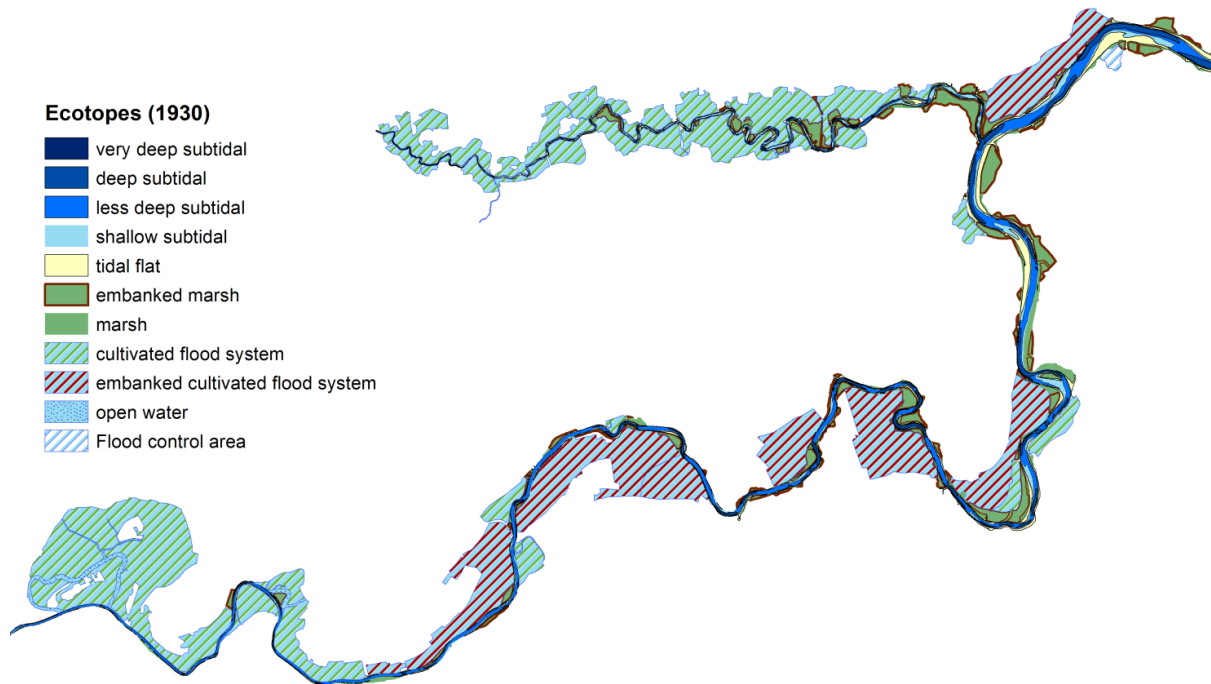
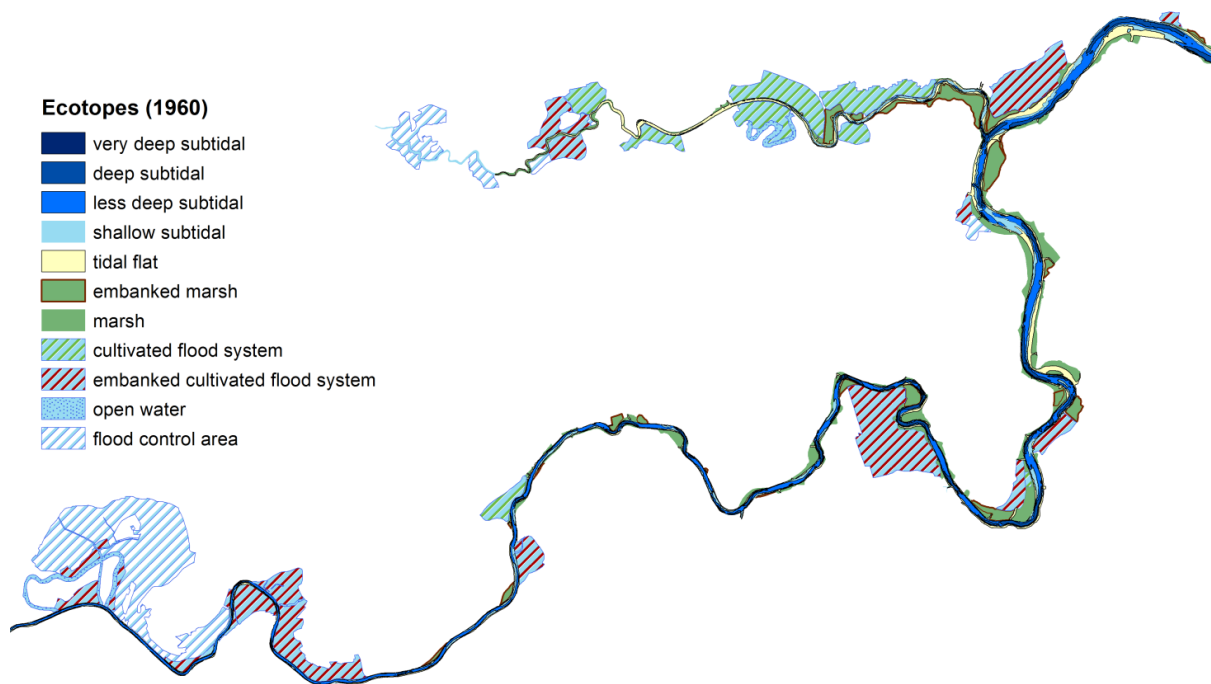


Figure 6 – Historical ecotope map of the Upper Sea Scheldt and Durme river for 1960.



## 4.4 Bottom Friction

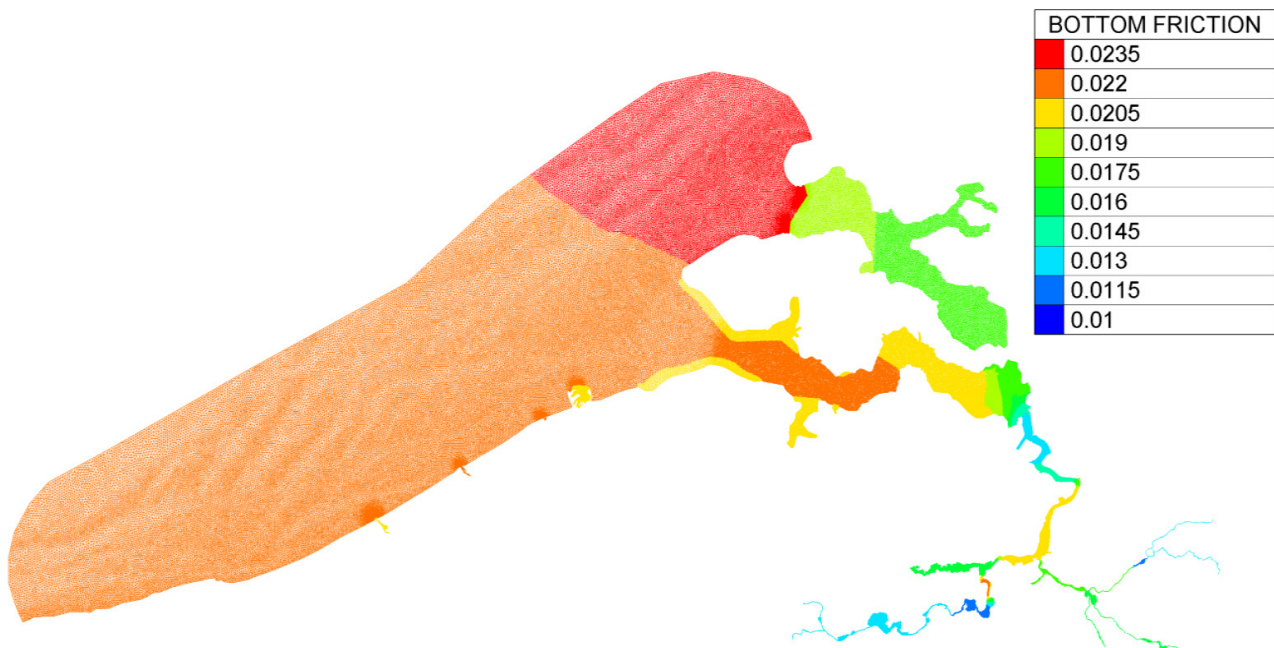
Bottom friction is implemented by assigning spatially varying Manning’s roughness coefficients to the model grid. TELEMAC converts these Manning’s coefficients to dimensionless bottom friction coefficients based on:

$$c_f = \frac{2gn^2}{h^{1/3}}$$

in which  $c_f$  is a dimensionless friction coefficient,  $g$  [ $\text{m}\cdot\text{s}^{-2}$ ] is the gravity acceleration,  $h$  [m] is the water depth and  $n$  [ $\text{s}\cdot\text{m}^{-1/3}$ ] the Manning’s friction coefficient.

Initially, a calibrated bottom friction field from the Scaldis2013 model by Smolders et al. (2016) is used for all historical models (Figure 7). However, the bottom friction coefficient will be used as a calibration parameter for the calibration of the historical models later on in this report.

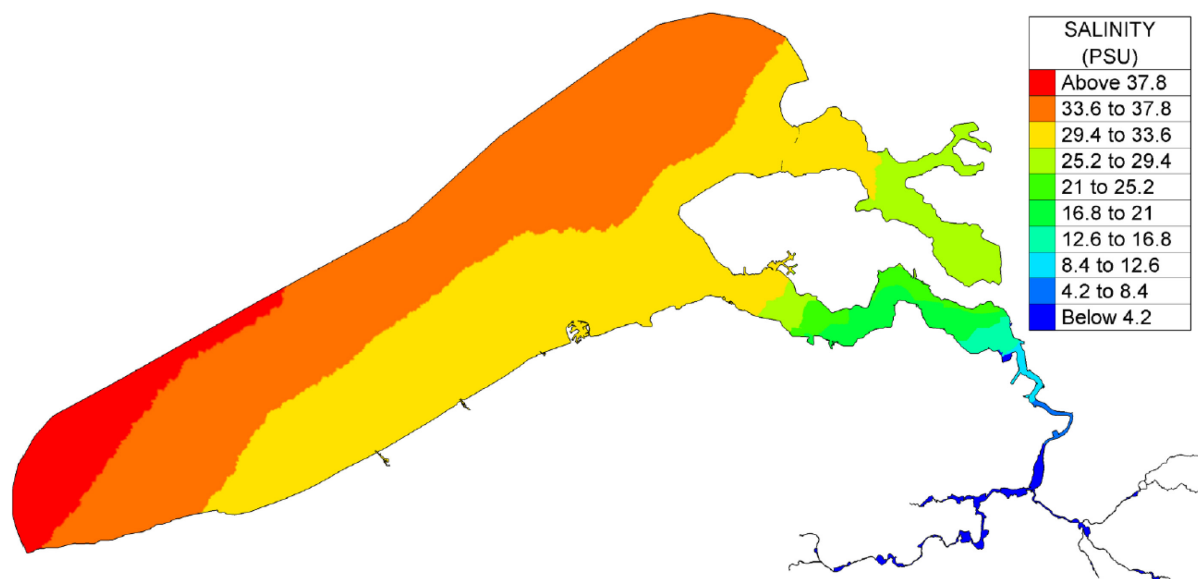
Figure 7 – Map of the Manning’s friction coefficients in the calibrated Scaldis2013 model by Smolders et al. (2016).



## 4.5 Salinity

Salinity is schematized as an active tracer in the TELEMAC-3D model. A similar initial salinity field is used in all simulations (Figure 8), regardless of the year of the historical simulation. The salinity field is adopted from the 2013 Scaldis model described in Smolders et al. (2016). It was based on a combination of salinity measurements and corrected model results from the ZUNO model. Besides, sensitivity analyses in that study showed that the impact of salinity-induced density gradients on water levels in the estuary is up to 0.10 m.

Figure 8 – Initial salinity field (Smolders et al., 2016).



## 4.6 Boundary conditions

### 4.6.1 Selection of simulation periods

A simulation period of 1 month (2 spring-neap cycles) needs to be selected for each historical model (i.e., 1930, 1960, 1980, 2001 and 2013). This is done based on the results of the historical CSM-ZUNO model runs as the CSM-ZUNO model results will be implemented as a downstream boundary condition later on (§4.6.3).

In the selection procedure, it is intended that the surge at Vlissingen (difference between the measured high/low waters and the modelled astronomical tide in the CSM-ZUNO model) is as small as possible for the selected periods. The surge at Vlissingen is calculated by subtracting the modelled high- and low waters in the CSM-ZUNO runs from the measured high and low waters for each of the five years. Figure 9 shows these differences in high and low water levels between model and measurement for each year. In general, the high and low water levels are best represented during summer when the surge is weakest.

Secondly, the mean spring tidal amplitude and mean neap tidal amplitude at Vlissingen, as presented in the decadal overviews of the tidal characteristics (Vekemans, 1946; Codde & De Keyser, 1963; Claessens & Belmans, 1984; Taverniers & Mostaert, 2009; Vanlierde et al., 2016) must be reached in the selected simulation period for each respective year (Table 4). Analysis of the measured 2001-2010 water level time series at Vlissingen demonstrates that the average spring tidal amplitude of 4.45 m as presented in Vanlierde et al. (2016) corresponds to the P85-P90 percentile of all tidal amplitudes in this time period. Similarly, the mean neap tidal amplitude of 2.96 m (Vanlierde et al., 2016) corresponds to the P10-P15 percentile of all tidal amplitudes in the measured 2001-2010 time-series (Figure 10). Based on this outcome, the selection procedure of the simulation period must assure that: (1) the reported average spring and neap amplitudes of the specific decade are reached within the simulation period; (2) and that the P10 and P90 values of the modelled tidal amplitudes in the selected simulation period closely match the P10 and P90 values of the measured tidal amplitudes in the specific decade.

The selection algorithm and resulting simulation periods are presented below.

Figure 9 – Difference between measured and modelled high- and low water levels for each of the five years.

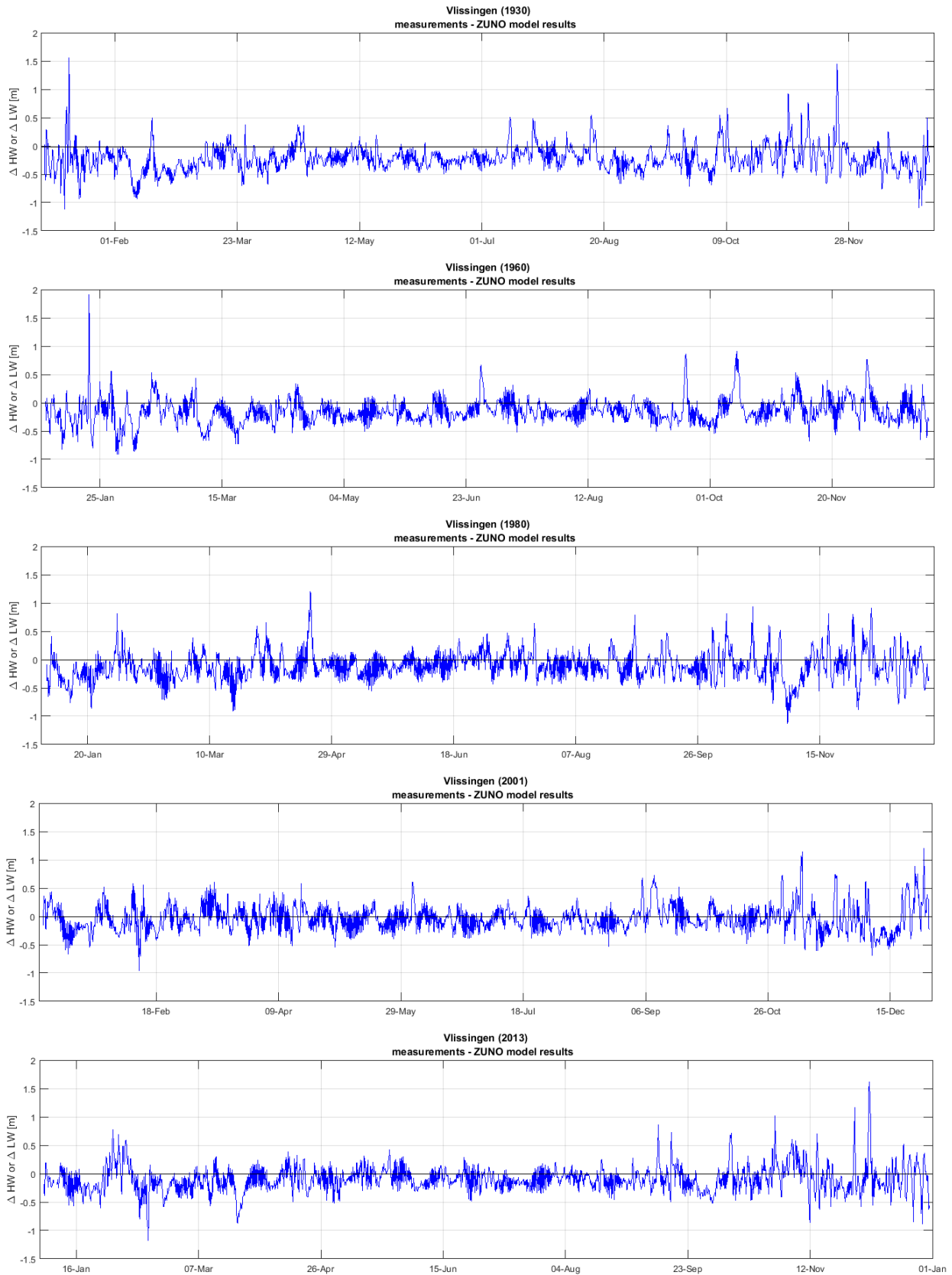


Figure 10 – Cumulative distribution of tidal amplitudes at Vlissingen for the period 2001-2010, with the average spring tidal amplitude and average neap tidal amplitude according to Vanlierde et al. (2016) indicated in red.

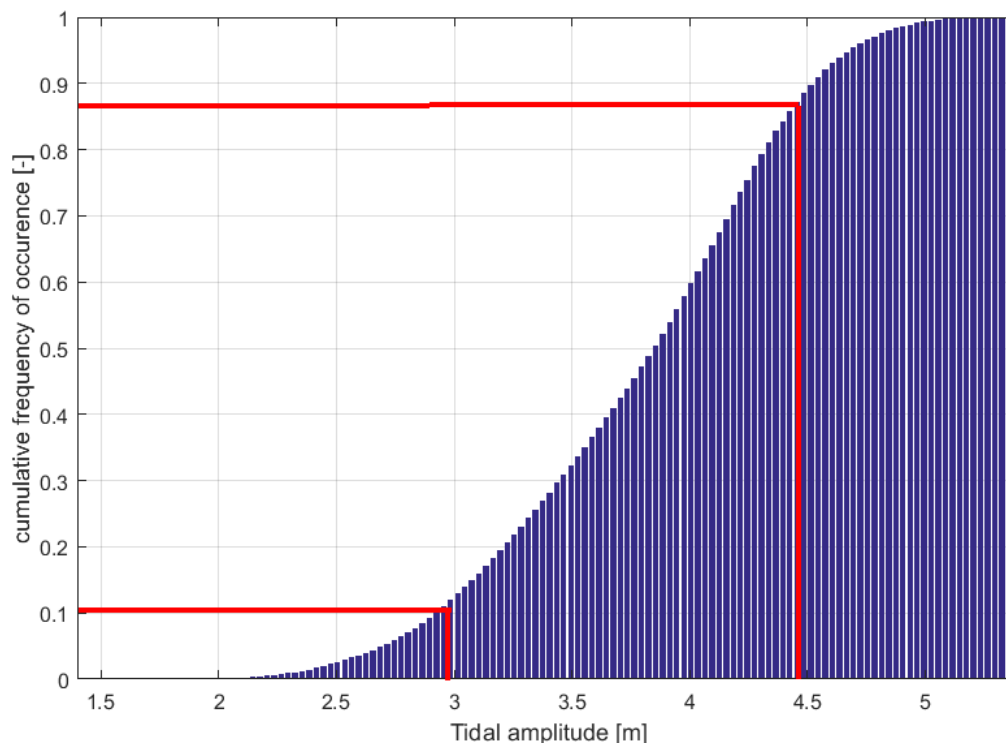


Table 4 – Mean spring tidal range and mean neap tidal range at Vlissingen used as reference for each period.

Period	Mean spring tidal range [m]	Mean neap tidal range [m]	Reference
1931-1940	4.35	2.92	<i>Vekemans, 1946</i>
1951-1960	4.43	2.97	<i>Codde &amp; De Keyser, 1963</i>
1971-1980	4.49	3.05	<i>Claessens &amp; Belmans, 1984</i>
2001-2010	4.45	2.96	<i>Vanlierde et al., 2016</i>

### Selection algorithm

The following methodology is followed to obtain a simulation period for each of the five years:

1. A moving window is applied to every possible period of 29.5 days within each simulated year, after which the P90 and P10 percentiles of the tidal amplitudes at Vlissingen are computed based on the CSM-ZUNO model results for each of these 29.5-day moving windows.
2. A logical test is applied to check whether the reported average spring- and neap tidal amplitudes at Vlissingen of the specific decade are reached within each 29.5-day period of the model simulation (i.e., check whether the *highest/lowest* simulated tidal amplitudes in the 29.5-day period are *higher/lower* than the average *spring/neap* amplitudes based on the decadal overviews in Table 4).  
 → Periods in which these decadal averages of the spring- and neap tidal amplitudes are not reached are excluded.

3. A second logical test is applied to check whether the P10 and P90 percentiles of the tidal amplitudes at Vlissingen of each 29.5-day period closely match the yearly P10 and P90 percentiles of the tidal amplitudes. Therefore, the simulated P10 and P90 percentiles of each 29.5-day period are compared with the measured P10 and P90 values of the tidal amplitudes of the specific year of interest by means of a relative difference.
  - Periods for which the relative difference of P10 or P90 is larger than 5% are excluded.
4. The RMSE of the modelled and measured high- and low water levels at Vlissingen is computed for each of the remaining 29.5-days periods.
  - Out of the remaining periods, the 29.5-day period with the lowest RMSE is selected as simulation period.

### Resulting simulation periods

This procedure results in the following simulation periods (including a 3-day spin-up period for the hydrodynamic computation as the simulations start from a constant water level):

- 1930: 18-7-1930 => 21-8-1930
- 1960: 05-8-1960 => 07-9-1960
- 1980: 24-7-1980 => 27-8-1980
- 2001: 31-7-2001 => 02-9-2001
- 2013: 12-7-2013 => 14-8-2013

For these periods, modeled water level time series from the harmonic CSM-ZUNO model runs are imposed at the downstream boundary of the Scaldis model.

The mean high water level, mean low water level, mean sea level (i.e., calculated from high and low waters only) and mean tidal range at Vlissingen are presented in Table 5 for each of the five simulation periods and compared with the 1930, 1960, 1980, 2001 and 2013 yearly averaged values. It is noted that the 1960 and especially the 1930 simulation period consist of relatively high water levels compared to the yearly averages (i.e., MHWL, MLWL and MSL are all above the yearly averages), which partly cancels out the effect of sea level rise between the selected simulation periods. In particular, the mean sea level differences between the simulation periods are limited to < 0.03 m. However, the tidal range does vary up to 0.20 m between the five simulation periods.

In a next step, a time-varying surge is added to these harmonic boundary conditions based on differences in high- and low water level at Vlissingen between measurements and results of a first Scaldis run for each year (see §4.6.4).

Table 5 – Mean high water level, mean low water level, mean sea level (calculated from high and low waters only) and mean tidal range for the selected simulation periods and yearly averages.

Period	MHWL [m TAW]		MLWL [m TAW]		MSL [m TAW]		Mean TR [m]	
	Full year	Sim. Period	Full year	Sim. Period	Full year	Sim. Period	Full year	Sim. Period
1930	4.18	4.34	0.48	0.58	2.33	2.46	3.69	3.76
1960	4.34	4.43	0.46	0.54	2.40	2.49	3.87	3.90
1980	4.40	4.46	0.49	0.51	2.44	2.48	3.92	3.96
2001	4.44	4.41	0.58	0.57	2.51	2.49	3.87	3.84
2013	4.39	4.43	0.52	0.51	2.45	2.47	3.87	3.93

#### 4.6.2 Upstream discharge boundary

Time series of measured discharges are defined at the upstream model boundaries (see §2.2) for 1980, 2001 and 2013. For the 1930 and 1960 models, average discharges are used based on daily discharge measurements from 1-1-1954 until 1-4-1954 obtained from Dujardin et al. (2017). The discharge boundary conditions for each of the tributaries are shown in Figure 11 – Figure 15.

Figure 11 – Input discharge conditions at Merelbeke or Gentbrugge (Upper Sea Scheldt) for the five historical models

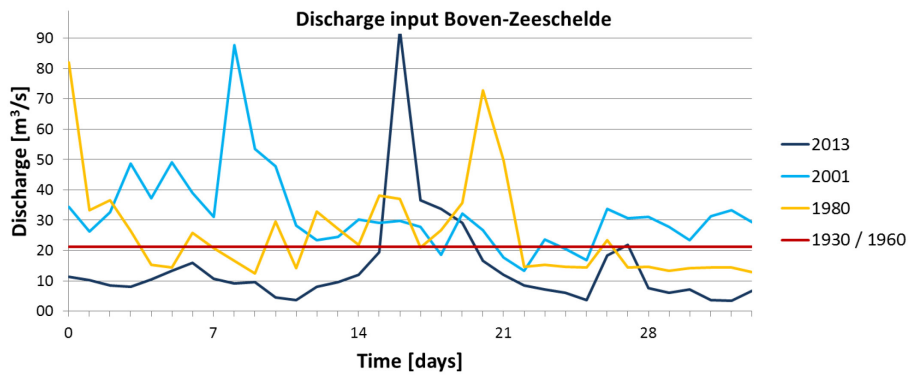


Figure 12 – Input discharge conditions at Dendermonde (Dender) for the five historical models

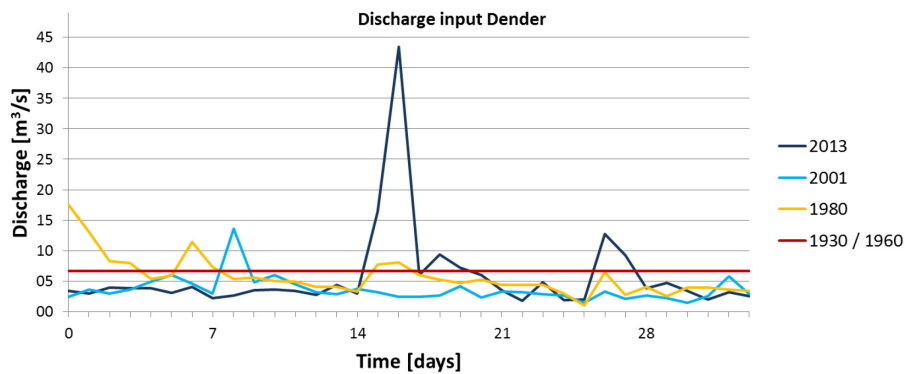


Figure 13 – Input discharge conditions at the Zenne for the five historical models

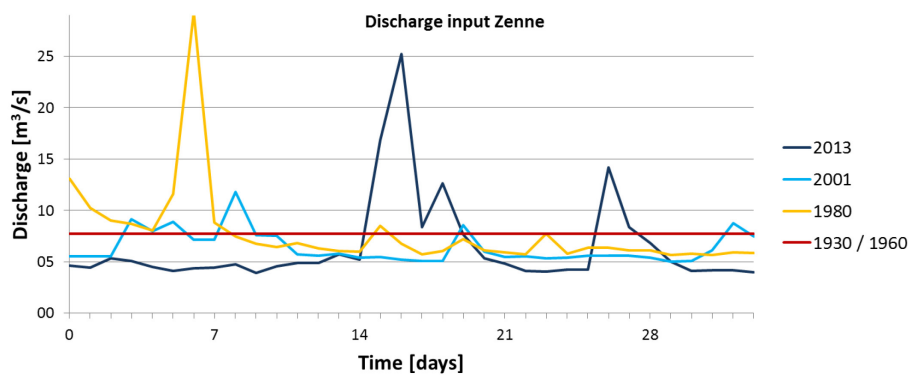


Figure 14 – Input discharge conditions at the Dijle for the five historical models

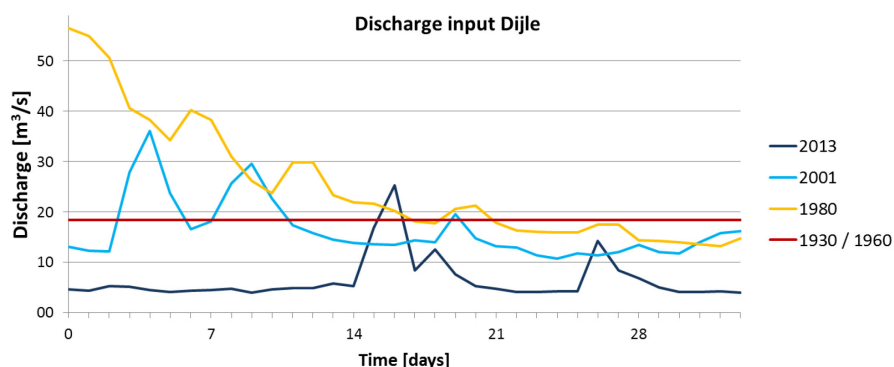
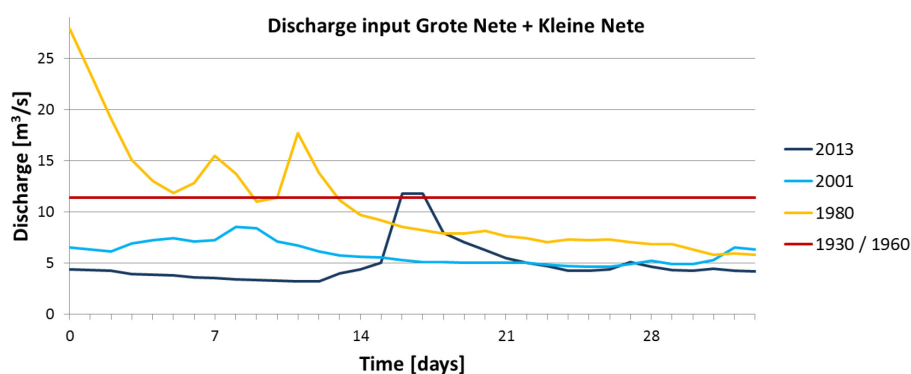


Figure 15 – Input discharge conditions at the Grote Nete and Kleine Nete (combined) for the five historical models



The upstream discharge boundary of the Upper Sea Scheldt is implemented at Merelbeke for the 2013, 2001 and 1980 models, while it is implemented at Gentbrugge in the 1960 and 1930 models (see Figure 1 for locations). In the latter model periods, the southern Ringvaart channel between Merelbeke and Melle did not yet exist. Similarly, the discharge of the Dender is implemented at the sluices near Dendermonde for the 2013, 2001 and 1980 models, whereas it is implemented at the Oude Dender river branch in Dendermonde for the 1960 and 1930 models.

It is noted that there is no discharge defined at the Spuikanaal in Bath and at the sluices in Terneuzen. Sensitivity analysis showed that the effect of discharges at Bath (e.g. 22 m<sup>3</sup>/s on average between 13-9-2013 and 18-12-2013) on the water levels along the estuary is negligible (i.e., only up to 0.2 cm). See Appendix 10.3.

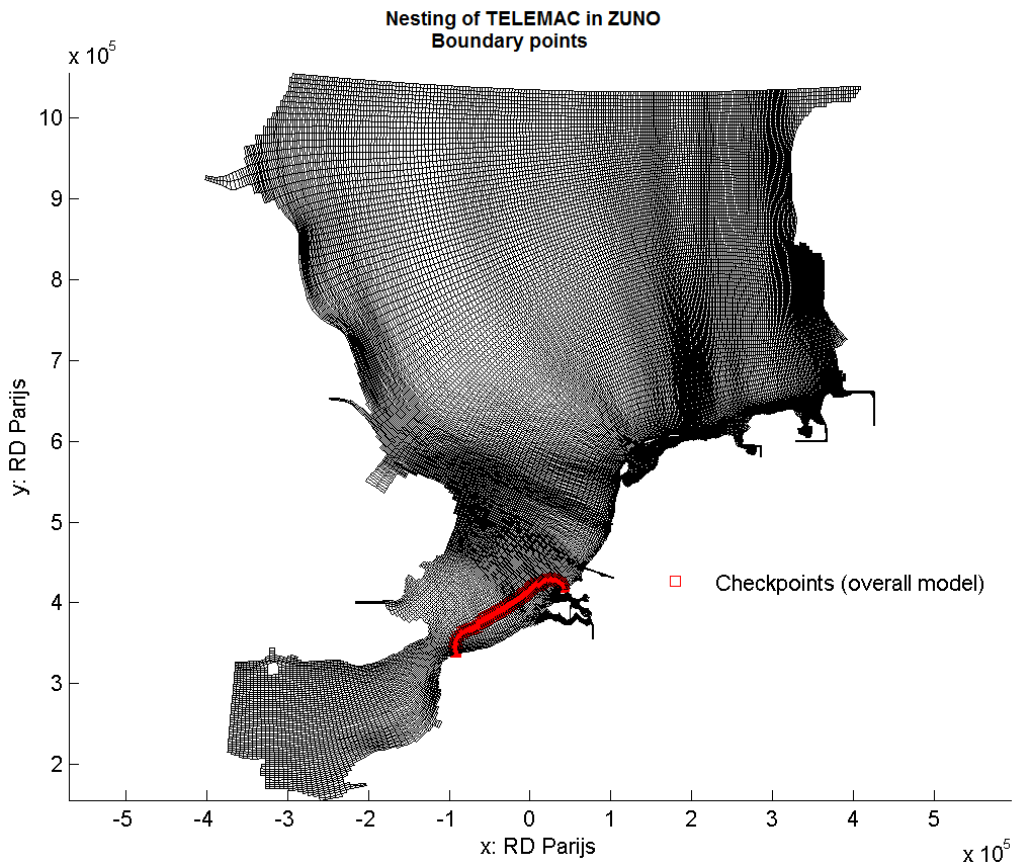
The average discharges from the Kanaal Gent-Terneuzen are even smaller relative to the local tidal prism (e.g. 27 m<sup>3</sup>/s on average between 13-9-2013 and 18-12-2013, but the tidal prism is more than twice as large) and are therefore not expected to have any significant effect on the water levels either.

#### 4.6.3 Downstream water level boundary

The downstream model boundary of the Scaldis model is nested in the regional CSM-ZUNO model of the southern North Sea (Figure 16). Water level time series with a 10 minutes interval are computed with the harmonic CSM-ZUNO model (§3.2), and are imposed at the downstream boundary of the Scaldis model. A modified version of the bord3d.f subroutine is used to allocate values for the water level and salinity at each boundary node (see Smolders et al., 2016).

Next, a time-varying surge component is added to these harmonic boundary conditions based on differences in high- and low water level at Vlissingen between measurements and results of a first Scaldis run for each year (see §4.6.4).

Figure 16 – Nesting of Scaldis model in ZUNO. Scaldis boundary nodes given in red



### Salinity

Furthermore, the salinity boundary conditions at the downstream boundary are also generated by nesting the Scaldis model in the CSM-ZUNO model train. In particular, the historical CSM-ZUNO model results comprise salinity values at the downstream Scaldis model boundary. These values are directly imposed to the (historical) Scaldis models. No further corrections are applied to these boundary conditions.

#### 4.6.4 Correction of the water level boundary conditions from the CSM-ZUNO model

##### Implementation of surge component at the downstream model boundary

Surge effects are implemented based on the results of a first simulation for each historical model at Vlissingen. These simulations are performed with the friction field, boundary conditions and other model settings described in this section (i.e., before altering the friction field during the model calibration). Besides, the model results at Vlissingen are not yet affected much by potential bad representation of the tidal wave in more upstream parts of the estuary.

A difference signal in between the measured and modelled high and low water levels is calculated at Vlissingen for each historical run. A centered moving average technique is then applied so that high and low water levels contribute equally to the difference signal (i.e., assuring that there is no tidal component in the surge signal). In particular, the centered moving average signal is averaged over two tides and always gives equal summed weights to the contributing high waters and low waters.

To correct for the (wind) surge that was present during the simulation periods, as well as for the inaccuracy of the CSM-ZUNO model output at the Scaldis model boundary, the obtained centered moving averages are implemented as surge signals in the historical models prior to the model calibration and validation.

Figure 17 - Figure 21 show the differences between measured and modelled high- and low water levels at Vlissingen, as well as the centered moving averages of the difference signals, for the initial model runs (top plots) and for model runs in which the surge component is added (bottom plots).

On average, the historical models overestimated the high and low water levels at Vlissingen by 0.08-0.10 m before adding the surge component. After adding the surge correction to the boundary conditions, the combined high and low water BIAS reduces to less than 0.01 m for the 1930, 1960, 1980 and 2001 models, and to less than 0.03 m for the 2013 model.

It is noted that the individual HW and LW differences of the 1980 model are characterized by a general underestimation of HW and a general overestimation of LW (Figure 19), implying an underestimated tidal range. This is not corrected for by the added surge signal, which corrects for mean water level variations (i.e., the moving averaged technique is based on both high and low waters).

### Phase shift

Additionally, a comparison between modelled and measured  $T_{HW}$  and  $T_{LW}$  reveals that the initial model results of the five historical models have an average phase lead of 8-13 minutes at Vlissingen (not shown in figures). To resolve this, a 10-minutes phase shift is applied to the imposed time series at the downstream water level boundary prior to the model calibration and validation.

Figure 17 – Difference between measured and modelled high- and low water levels at Vlissingen for the 1930 model before (top) and after (bottom) the additional surge component was implemented.

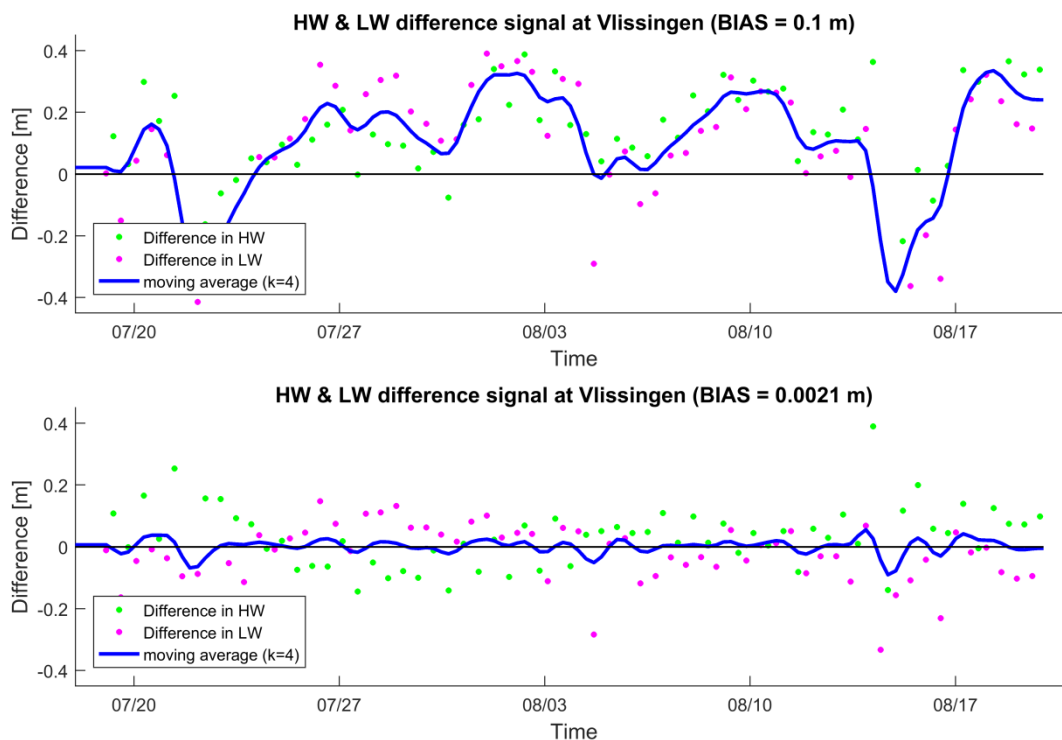


Figure 18 – Difference between measured and modelled high- and low water levels at Vlissingen for the 1960 model before (top) and after (bottom) the additional surge component was implemented.

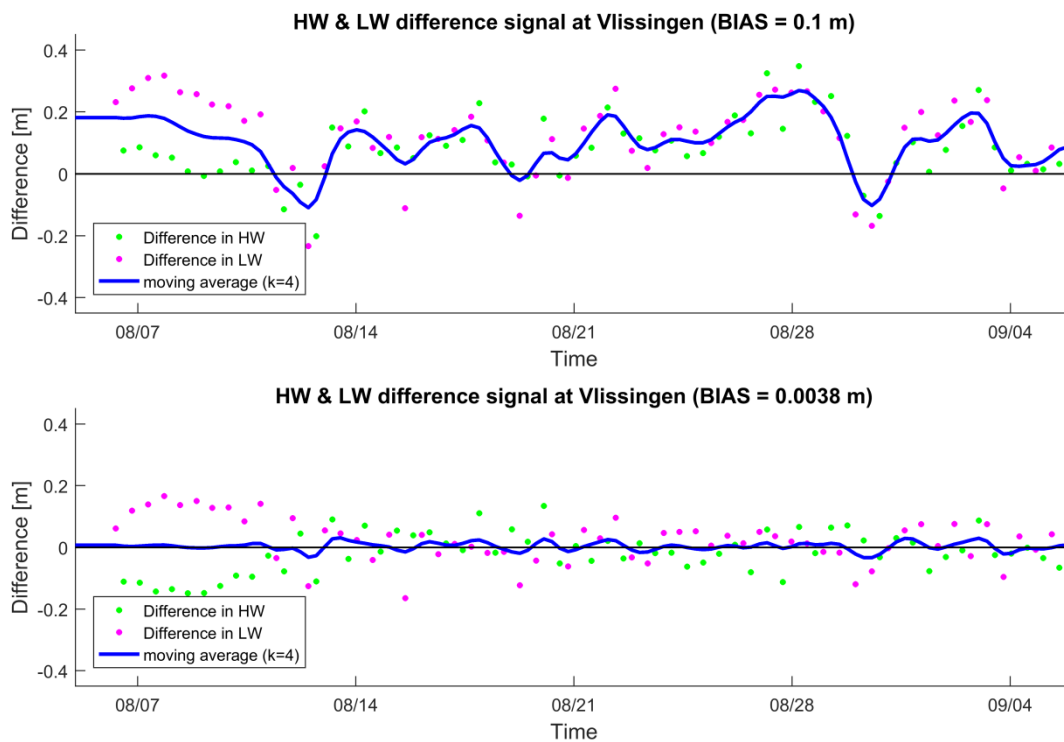


Figure 19 – Difference between measured and modelled high- and low water levels at Vlissingen for the 1980 model before (top) and after (bottom) the additional surge component was implemented.

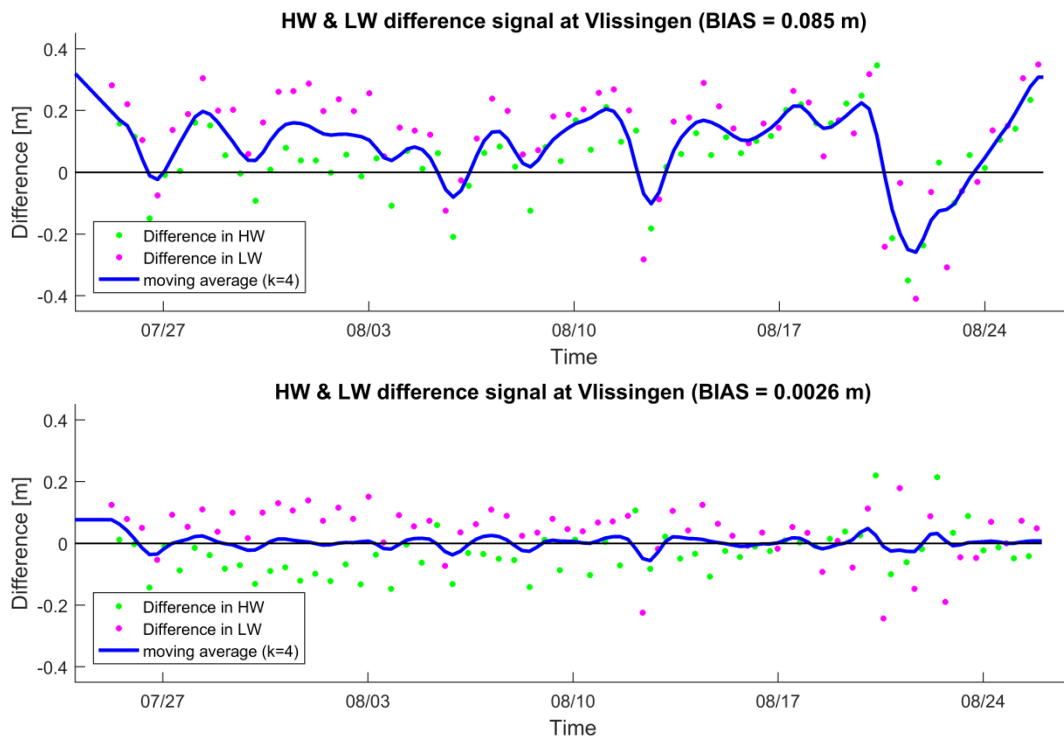


Figure 20 – Difference between measured and modelled high- and low water levels at Vlissingen for the 2001 model before (top) and after (bottom) the additional surge component was implemented.

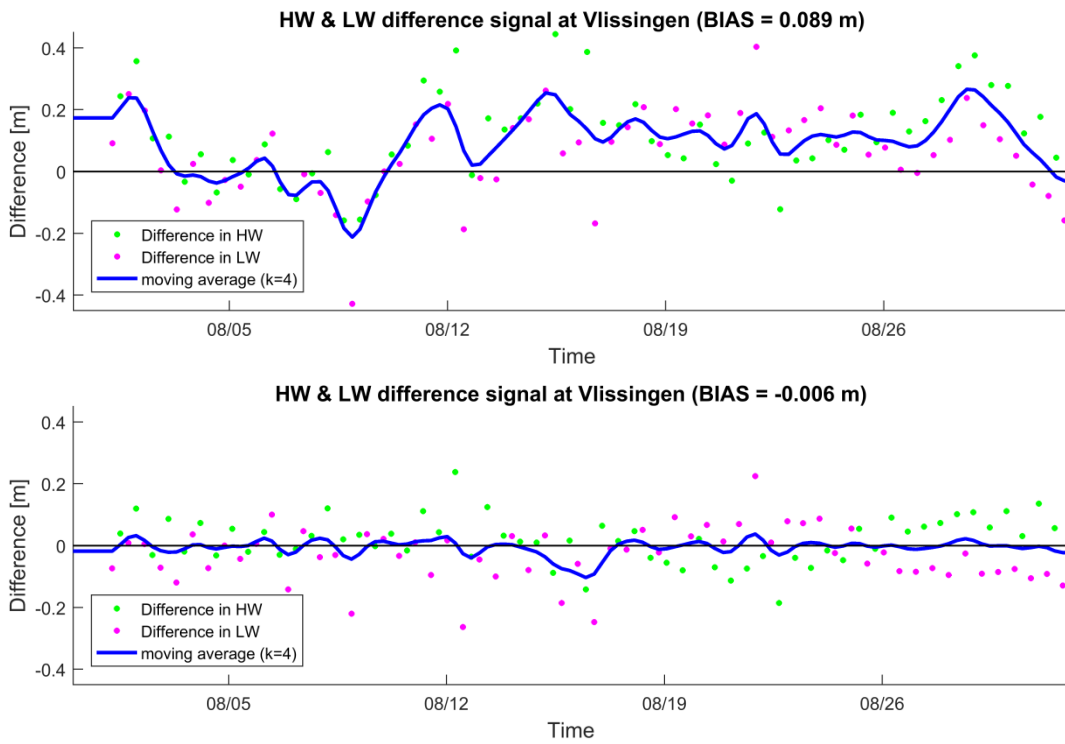
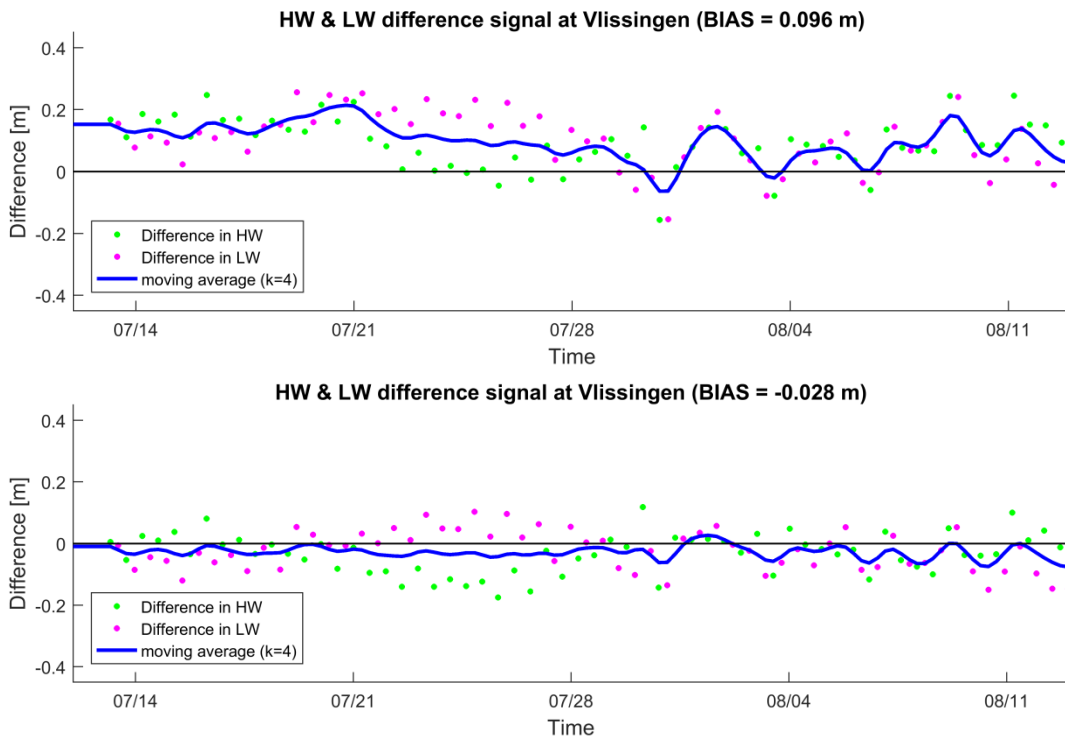


Figure 21 – Difference between measured and modelled high- and low water levels at Vlissingen for the 2013 model before (top) and after (bottom) the additional surge component was implemented.



## 4.7 Model settings

The most important model settings are listed in Table 6. More information regarding the background of these parameter settings, as well as about the calibration and validation of the present-day Scaldis-model is available in Smolders et al., (2016).

Table 6 – Applied model settings

Parameter	Value
Time step	4 s
Initial condition	constant elevation and start with smoothing time
Number of layers in the vertical	5 (3D model)
Version TELEMAC	TELEMAC V7P2
Salt transport	On
Wind	Off
Bottom friction formula	Manning
Bed roughness value	varying roughness field
Friction formula for lateral boundaries	Nikuradse Law
Friction coefficient for lateral boundaries	0.054848
Option for the treatment of tidal flats	1: equations solved everywhere with correction on tidal flats
Treatment of negative depths	2: flux control
Free surface gradient compatibility	0.9
Vertical turbulence model	2: mixing length
Mixing length model	3: Nezu and Nakagawa
Horizontal turbulence model	4: Smagorinski
Coefficient for vertical diffusion of velocities	0.01
Coefficient for horizontal diffusion of velocities	0.01
Scheme for advection of velocities	1: characteristics
Scheme for advection of depth	5: conservative scheme
Scheme for advection of tracers	13: Leo Postma for tidal flats
Scheme for diffusion of velocities	1: implicit (1 is default; 0 cancels the diffusion)
Scheme for diffusion of tracers	1: implicit
Solver	7: GMRES

## 5 Model calibration

### 5.1 Methodology

#### Calibration procedure

First, initial model simulations are performed based on the bottom friction field as it was calibrated for the present-day model (i.e., 2013-model) by Smolders *et al.* (2016). These simulations mainly aim at obtaining a first insight about the model performance and possible adaptations that could be done to the bottom friction field to improve the model performance for the historical models. In particular, these initial model runs are used to check in which parts of the estuary tidal amplification or damping is underestimated or overestimated for each simulated year. Moreover, distinct friction zones for the simultaneous calibration of the historical models are chosen based on the initial model simulations. See §5.2.

After the initial runs are completed, a simultaneous model calibration is performed for all historical models (including the present-day 2013-model) based on adjustment of the spatially varying bottom friction values for all years simultaneously. Hence, the model calibration optimizes the model performance for all years combined while using identical bottom friction fields. Although the 2013 model was already calibrated by Smolders *et al.* (2016), additional calibration runs are also performed for the 2013 model to have a similar friction field for all five historical models. This has the advantage that differences between the model results of the five historical models can solely be attributed to variations in the estuary's geometry and bathymetry. Hence, the potential influence of variable bottom friction fields on modelled historical changes in tidal hydrodynamics can then be discarded. Another advantage of a simultaneous model calibration of the five historical models is that the computational efforts for the model calibration are reduced significantly. Besides, it allows for a check whether the model performance of the existing 2013 model does not deteriorate too much or if it can be further optimized through adaptations to the friction field.

For the first calibration runs, constant friction values are used for the entire estuary. Friction values are then stepwise adjusted for three main friction zones in the estuary: Western Scheldt (up until Bath), Lower Sea Scheldt (up until the Scheldt-Rupel confluence near Schelle) and Upper Sea Scheldt (up until Gentbrugge / Merelbeke). A stepwise calibration implies that the friction field is first calibrated for the Western Scheldt, then for the Lower Sea Scheldt and lastly for the Upper Sea Scheldt. See §5.3.

#### Cost function and calibration targets

The calibration of the historical models is based on HW and LW measurements at the tidal stations listed in Table 1. Although full water level time series are available for years 2001 and 2013, these water level time-series are not used in the calibration process. This way, the calibration of all historical models is done similarly and a simultaneous model calibration for all historical models can be performed. A dimensionless cost function is defined to get one objective factor which represents improvements (decrease) or deterioration (increase) of the model performance. The cost function is expressed in function of the reference run, so a value lower than 1 indicates an improvement:

$$Cost = \sum \frac{Factor_i}{Factor_{i,ref}} Weight_i$$

A combined cost function for all years is used during the calibration process, allowing for a simultaneous calibration of all historical models. Consequently, the outcome of the cost function gives the model performance averaged over all historical models. Hence, the parameter settings (i.e., spatially varying

friction field) that lead to the lowest cost give the best combined model performance over all historical models. However, it does not automatically imply that these settings lead to the best model performance for each individual historical model.

The cost function is applied to the root mean squared error of the modeled high- and low water levels (HWL and LWL), as well as of the timing of the high and low waters ( $T_{HW}$  and  $T_{LW}$ ). The RMSE-values are first averaged over the five historical models for each calibration configuration. The high and low water levels contribute for 75% to the cost function, while the phase or timing of the high waters and low waters contributes for 25%. Furthermore, high water level errors and low water level errors contribute evenly to the cost function (Table 7).

The above-described cost function is utilized at the following tidal stations: Vlissingen, Terneuzen, Hansweert, Bath, Liefkenshoek, Antwerpen, Temse, Dendermonde, Schoonaarde, Wetteren en Melle. As the model calibration is done per estuary section (i.e., Western Scheldt, Lower Sea Scheldt and Upper Sea Scheldt), a combined cost is also calculated per section. For each section, more upstream situated tidal stations get a higher weight than more downstream situated tidal stations (Table 8). Stations from adjacent downstream sections are also included in the cost function to account for potential downstream effects of friction changes in a certain zone.

Table 7 – Calibration parameters used in cost function

Physical Quantity	Error Measure	Weight
High water level [m]	RMSE	37.5%
High water phase [min]	RMSE	12.5%
Low water level [m]	RMSE	37.5%
Low water phase [min]	RMSE	12.5%

Table 8 – Weight of tidal stations in cost calculation per estuarine section.

Tidal Station	Weight in combined cost	Weight in combined cost	Weight in combined cost
	Western Scheldt	Lower Sea Scheldt	Upper Sea Scheldt
Vlissingen	1	-	-
Terneuzen	1	-	-
Hansweert	2	-	-
Bath	2	1	-
Liefkenshoek	-	1	-
Antwerpen	-	2	1
Temse	-	2	1
Dendermonde	-	-	2
Schoonaarde	-	-	2
Wetteren	-	-	2
Melle	-	-	2

### Simulation periods for calibration runs

To reduce computation times for the model calibration runs, the model performance of each calibration run is assessed over a period of 15 days (i.e., instead of 29.5 days) after an initial spin-up period of three days:

- 1930: 21-7-1930 => 05-8-1930
- 1960: 08-8-1960 => 23-8-1960
- 1980: 27-7-1980 => 11-8-1980
- 2001: 02-8-2001 => 17-8-2001
- 2013: 15-7-2013 => 30-7-2013

## 5.2 Initial model results with the Scaldis2013 bottom friction field

Initial model runs are performed for all historical models in which the bottom friction field of the previously calibrated Scaldis 2013 model is used (Figure 7) and in which the additional surge component is implemented at the downstream model boundary (see §4.6.4). As stated before, areas that were classified as cultivated flood systems by Van Braeckel et al. (2012) are excluded from all calibration runs in the historical 1930, 1960 and 1980 models.

Figures depicting the mean errors for high and low water levels, as well as high and low water level phases are included in Appendix 10.4. In particular, Figure 59 until Figure 63 depict the mean errors (BIAS) of each historical model for high and low water levels. Similarly, Figure 64 until Figure 68 depict the mean errors (BIAS) of each historical model for the timing of the high and low waters. The BIAS-values are calculated over a period of two weeks.

The results of the initial model simulations with the Scaldis 2013 friction field can be considered good in the most downstream section of the estuary (i.e., Western Scheldt up until Bath). The under- or overestimation of high and low water levels remains smaller than 0.10 m (which can be considered as good) in this part of the estuary for all but one of the historical models. An exception is the 1980 model in which the tidal range is underestimated along the Western Scheldt and in which the overestimation of the low water levels at Bath reaches 0.20 m. The model performance in the Sea Scheldt is generally worse than in the Western Scheldt, especially in the most upstream part of the estuary.

For the 1930 model, mean errors remain lower than 0.10 m up until Schoonaarde, upstream of which the high water levels are underestimated and the low water levels are overestimated (hence, the tidal range is underestimated). The errors of the high- and low water phase are within -10 and +15 minutes along a large part of the estuary, except for the most upstream part where the high waters have a phase lag of up to 25 minutes.

The model performance of the 1960 model shows different trends. Both high water levels and low water levels are overestimated in the Lower Sea Scheldt (i.e., between Bath and Antwerpen), beyond which the tidal range is also underestimated. The error on the high- and low water level phase remains between -10 and +10 up until Antwerpen for the 1960s model. Further upstream, the phase lag gradually increases to almost 20 minutes for the high waters at Melle and almost 30 minutes for the low waters at Melle.

The 1980 model performs fairly well in the Lower Sea Scheldt (i.e., up until Schelle) given the fact that the tidal range was already underestimated in the Western Scheldt. This underestimation is even stronger in the most upper part of the estuary (i.e., upstream of Dendermonde). For the 1980s model, the high water phase error is between -15 and +15 minutes in the entire estuary, except for the most upstream tidal station of Melle, where the phase lag is a bit larger. The low water phase error remains small up until Schoonaarde, but significantly increases to a phase lag of over 40 minutes in the most upstream part of the estuary.

The model performance of the 2001 model is good in the Lower Sea Scheldt, whereas low water levels are overestimated by about 0.10-0.20 m in the Upper Sea Scheldt. The latter is again an underestimation of the tidal range in this part of the estuary. Furthermore, both the high water phase error and the low water phase error are smaller than the output time step of 10 minutes at all tidal stations along the estuary.

Finally, the 2013 model performs good in the Lower Sea Scheldt and slightly worse in the Upper Sea Scheldt where both high water levels and low water levels are underestimated by up to 0.15 m. As for the 2001 model, the phase lag or phase lead of the modeled high- and low waters in the 2013 model is smaller than the output time step of 10 minutes at all tidal stations along the estuary.

### Potential influence of discharge peaks

With respect to the over- or underestimation of high and low water levels in the upper part of the estuary, it should be stated that upstream discharges from Gentbrugge or Merelbeke (see §4.6.1) can significantly influence high and low water levels in the Upper Sea Scheldt (e.g. Maximova et al., 2009). In particular, peak discharges can increase both high and low water levels by more than one meter in the upper part of the estuary. For the model calibration, the upstream discharges are implemented as daily averages, which could potentially mean that the effect of discharge peaks on the modelled high- and low water levels is underestimated. The upstream boundaries of the 1960 and 1930 models are even forced by constant (mean) discharges, implying that the effect of discharge variation on high and low water levels in the upstream part of the estuary is not included in those model simulations. This may again lead to an underestimation of the high- and low water levels in the upstream part of the estuary in case relatively high discharges occurred during the simulated periods. Similarly, overestimation of high- and low water levels may occur in case the actual upstream discharges that occurred during the simulated periods were much lower than the implemented mean discharge for the 1930 and 1960 models.

Evaluation of the surge signal along the estuary shows that the high peak discharge present during the 2013 simulation period (Figure 11 - Figure 15) induces a significant surge signal in the Upper Sea Scheldt (see Appendix 10.4), potentially leading to an underestimation of the high- and low water levels in the 2013 model. Figure 63 indeed shows an underestimation of both high- and low water levels in the most upstream part of the estuary.

It is noted that an erroneous or oversimplified representation of the actual upstream discharge at Gentbrugge or Merelbeke cannot explain the strong underestimation of the tidal range (i.e., overestimation of low water levels along with an underestimation of high water levels) that is present in some of the historical models in the most upstream part of the estuary.

### 5.3 Model calibration based on bottom friction adjustments

The simultaneous model calibration of the historical models is done based on stepwise adaptations of the bottom friction in three main sections of the estuary. These sections are chosen based on the results of the initial simulations in §5.2. These results suggest that the original Scaldis2013 friction field (Figure 7) can probably be simplified by removing the distinct area of reduced friction in the Lower Sea Scheldt near the Dutch-Belgian border and the stretch of increased friction near St. Amands as they do not seem to have a positive impact on the model performance of the historical models. In particular, the modelled tidal range increase between Bath and Antwerpen is slightly too high in most historical models, while the bottom friction between Temse and Dendermonde seems to be too high for most historical models. Consequently, three large friction zones remain:

- Western Scheldt friction zone from the estuary mouth up until Bath with Manning friction coefficients of 0.021-0.022  $\text{s}\cdot\text{m}^{-1/3}$ .
- Lower Sea Scheldt friction zone from the Dutch-Belgian border up until the Scheldt-Rupel confluence with friction coefficients of approximately 0.016-0.020  $\text{s}\cdot\text{m}^{-1/3}$ .
- Upper Sea Scheldt friction zone from Temse up until the upstream boundary at Merelbeke or Gentbrugge with friction coefficients of 0.012-0.016  $\text{s}\cdot\text{m}^{-1/3}$ .

Figure 22 shows a map of these three zones in the model domain. The friction values are set constant for each friction zone after which a stepwise calibration of the friction values is performed. The bottom friction is first calibrated for the Western Scheldt, then for the Lower Sea Scheldt and finally for the Upper Sea Scheldt. As indicated in Figure 22, the friction coefficients are gradually changing from one zone to the other. The Rupel contributory and its own contributories are given the same friction coefficients as the Lower Sea Scheldt. The bottom friction in the offshore zone and the Eastern Scheldt is not changed during the model calibration. Friction coefficients of the Scaldis 2013 model (Smolders et al., 2016) are used in these areas.

Figure 22 – Map of the friction zones used for the stepwise calibration of the historical models: Western Scheldt (red), Lower Sea Scheldt (green) and Upper Sea Scheldt (blue).

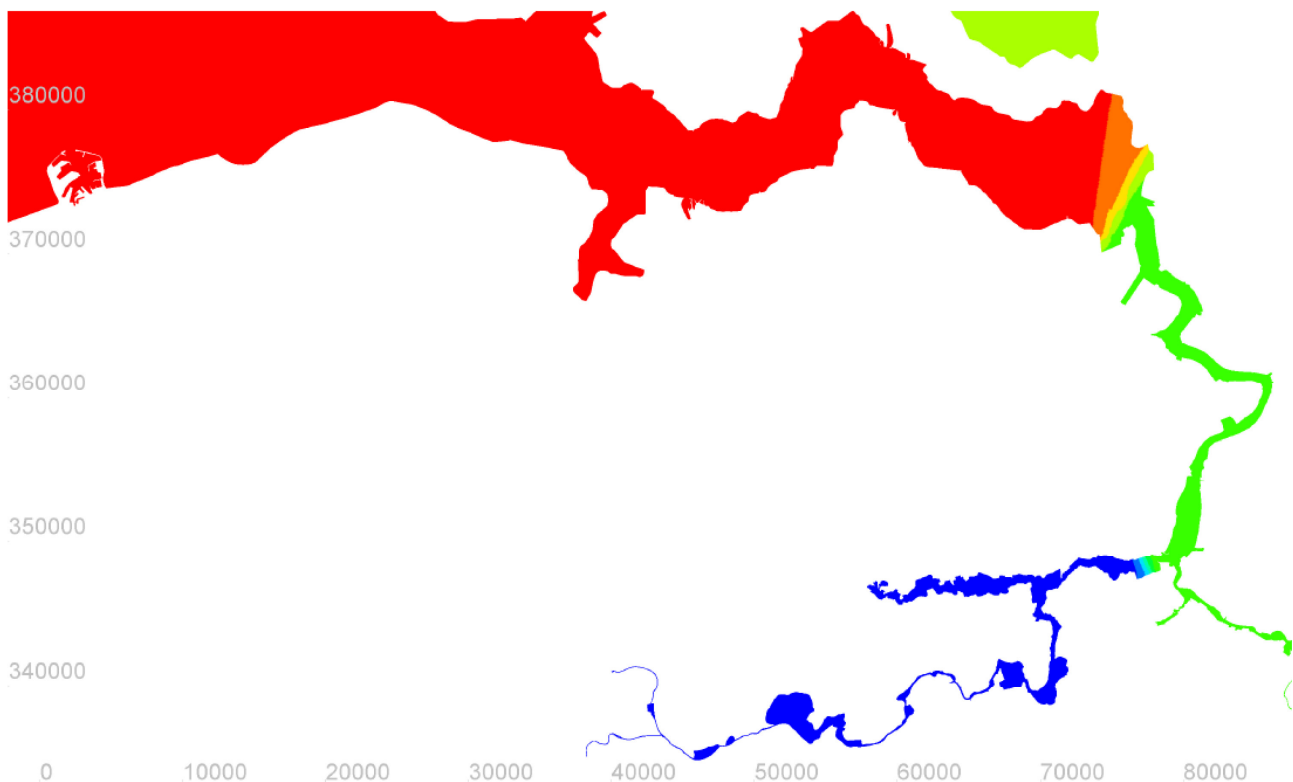


Table 9 lists the Manning coefficients that are used in each section for all performed calibration runs. Note that each calibration configuration is actually simulated with all five historical models. The selection of friction values for the calibration runs is done based on the model performance of the initial model runs with the Scaldis2013 friction field and on insights obtained during the calibration process itself. As the model performance of all historical models is already good in the Western Scheldt section, the Manning bottom friction coefficient is only varied between values of 0.021 to 0.022  $s \cdot m^{-1/3}$  in the calibration runs for the cal0x series in Table 9 (i.e., the calibrated Manning coefficients in the Scaldis2013 model also varies between 0.021 and 0.022  $s \cdot m^{-1/3}$  along the Western Scheldt). In the Lower Sea Scheldt section between the Dutch-Belgian border and the Scheldt-Rupel confluence, Manning coefficients are varied between 0.015 and 0.021  $s \cdot m^{-1/3}$  for the cal1x series in Table 9. Finally, in the Upper Sea Scheldt section upstream of Temse, Manning coefficients are varied between 0.012 and 0.016  $s \cdot m^{-1/3}$  for the cal2x series in Table 9.

The RMSE-values of the high and low water levels, as well as of the high and low water timing are presented in Appendix 10.6 for all calibration runs. In the following paragraphs, we discuss the outcome of the cost function for each of the three estuary sections.

Table 9 – Manning coefficients per friction zone used in calibration runs.

Calibration run	Western Scheldt (mouth – Bath)	Lower Sea Scheldt (Bath – Temse)	Upper Sea Scheldt (Temse – Gentbrugge)
c2	Scaldis2013 friction field	Scaldis2013 friction field	Scaldis2013 friction field
cal01	<b>0.021 <math>s \cdot m^{-1/3}</math></b>	<b>0.021 <math>s \cdot m^{-1/3}</math></b>	<b>0.021 <math>s \cdot m^{-1/3}</math></b>
cal02	<b>0.0215 <math>s \cdot m^{-1/3}</math></b>	<b>0.0215 <math>s \cdot m^{-1/3}</math></b>	<b>0.0215 <math>s \cdot m^{-1/3}</math></b>
cal03	<b>0.022 <math>s \cdot m^{-1/3}</math></b>	<b>0.022 <math>s \cdot m^{-1/3}</math></b>	<b>0.022 <math>s \cdot m^{-1/3}</math></b>
cal11	0.021 $s \cdot m^{-1/3}$	<b>0.020 <math>s \cdot m^{-1/3}</math></b>	<b>0.020 <math>s \cdot m^{-1/3}</math></b>
cal12	0.021 $s \cdot m^{-1/3}$	<b>0.019 <math>s \cdot m^{-1/3}</math></b>	<b>0.019 <math>s \cdot m^{-1/3}</math></b>
cal13	0.021 $s \cdot m^{-1/3}$	<b>0.018 <math>s \cdot m^{-1/3}</math></b>	<b>0.018 <math>s \cdot m^{-1/3}</math></b>
cal14	0.021 $s \cdot m^{-1/3}$	<b>0.017 <math>s \cdot m^{-1/3}</math></b>	<b>0.017 <math>s \cdot m^{-1/3}</math></b>
cal15	0.021 $s \cdot m^{-1/3}$	<b>0.016 <math>s \cdot m^{-1/3}</math></b>	<b>0.016 <math>s \cdot m^{-1/3}</math></b>
cal16	0.021 $s \cdot m^{-1/3}$	<b>0.015 <math>s \cdot m^{-1/3}</math></b>	<b>0.015 <math>s \cdot m^{-1/3}</math></b>
cal21	0.021 $s \cdot m^{-1/3}$	0.017 $s \cdot m^{-1/3}$	<b>0.016 <math>s \cdot m^{-1/3}</math></b>
cal22	0.021 $s \cdot m^{-1/3}$	0.017 $s \cdot m^{-1/3}$	<b>0.015 <math>s \cdot m^{-1/3}</math></b>
cal23	0.021 $s \cdot m^{-1/3}$	0.017 $s \cdot m^{-1/3}$	<b>0.014 <math>s \cdot m^{-1/3}</math></b>
cal24	0.021 $s \cdot m^{-1/3}$	0.017 $s \cdot m^{-1/3}$	<b>0.013 <math>s \cdot m^{-1/3}</math></b>
cal25	0.021 $s \cdot m^{-1/3}$	0.017 $s \cdot m^{-1/3}$	<b>0.012 <math>s \cdot m^{-1/3}</math></b>

### Calibration of bottom friction in Western Scheldt

The calibration of the friction coefficients in the Western Scheldt consists of three simulations in which the bottom friction of the entire estuary is set constant to 0.021, 0.0215 and 0.022  $s \cdot m^{-1/3}$  respectively. The model results are compared with the cost function described in §5.1. The initial model simulations with the Scaldis2013 friction field are used as reference run (or baserun) in the cost function.

Figure 23 shows the outcome of the cost function at each tidal station along the estuary. The combined model performance in the Western Scheldt (up until Bath) is improved slightly compared to the initial model performance if a constant friction value of 0.021  $s \cdot m^{-1/3}$  is used. However, the model performance is worse in the Sea Scheldt if these constant friction values are applied. If a friction value of 0.0215  $s \cdot m^{-1/3}$  or

0.022 s·m<sup>-1/3</sup> is applied, the model performance only improves slightly up until Hansweert, upstream of which the model performance deteriorates.

Table 10 gives the outcome of the cost function for the entire Western Scheldt zone, calculated with the outcome of the cost function in Figure 23 and the station weights in Table 8. The highest weights are assigned to the more upstream located tidal stations of Bath and Hansweert, while lower weights are assigned to the more downstream located tidal stations of Vlissingen and Terneuzen. Based on the outcome of the combined cost function for the tidal stations in the Western Scheldt friction zone, the best model performance in the Western Scheldt is obtained if a friction value of 0.021 s·m<sup>-1/3</sup> is used (simulation cal01).

Figure 23 – Outcome of the cost function for calibration runs cal01, cal02 and cal03 (compared to run c2) in which the bottom friction coefficients in the entire estuary are varied.

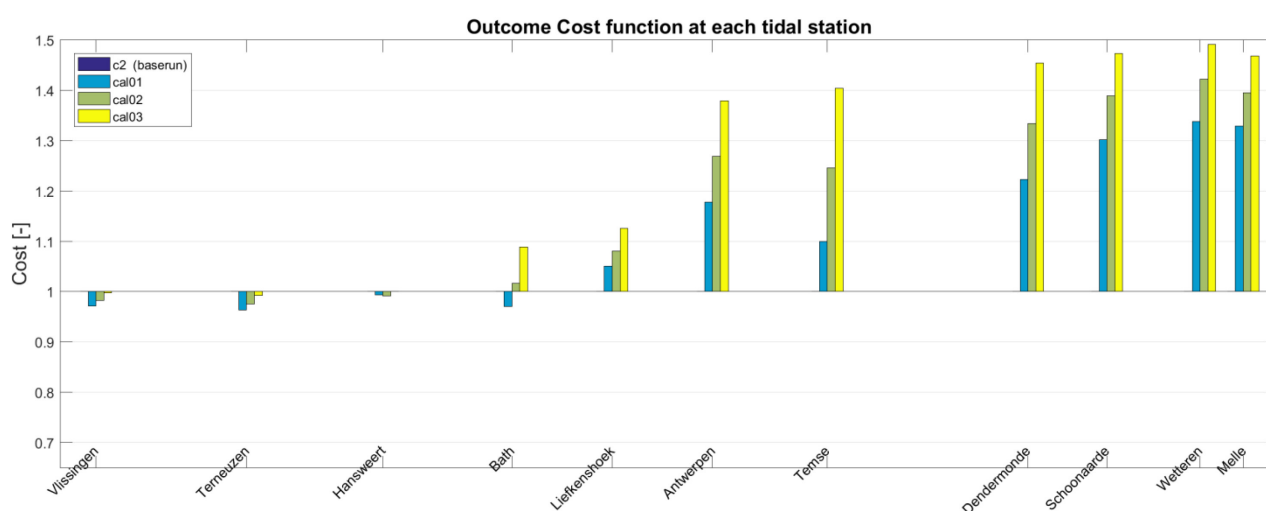


Table 10 – Outcome cost function for the Western Scheldt friction zone

Calibration run	Combined cost
c2 (baserun)	1.000
cal01	0.977
cal02	0.996
cal03	1.028

### Calibration of bottom friction in Lower Sea Scheldt

The calibration of the friction coefficients in the Lower Sea Scheldt consists of six additional simulations in which the bottom friction of the Lower Sea Scheldt and Upper Sea Scheldt is set constant to 0.020, 0.019, 0.018, 0.017, 0.016 and 0.015 s·m<sup>-1/3</sup> respectively (i.e., calibration runs cal11 – cal16). The bottom friction in the Western Scheldt is kept constant at 0.021 s·m<sup>-1/3</sup>. The model results of the calibration runs are compared using the cost function described in §5.1. Calibration run cal01, which gave the best results in the Western Scheldt friction zone, is used as reference run (or baserun) in this cost function. Figure 24 shows the outcome of the cost function at each tidal station along the estuary.

The model performance in the Western Scheldt remains more or less similar to cal01 for all additional calibration runs. In the Lower Sea Scheldt, the model performance improves slightly at Liefkenshoek and more significantly at Antwerpen and Temse, depending on the applied bottom friction coefficients in this

friction zone. Best combined results at Liefkenshoek and Temse are obtained with lower friction coefficients of  $0.015 \text{ s}\cdot\text{m}^{-1/3}$ , while the combined model performance at temse is optimized for friction values of  $0.017 \text{ s}\cdot\text{m}^{-1/3}$ . A comparison with the initial Scaldis2013 bottom friction field (i.e., simulation c2) reveals that all calibration runs have a slightly worse model performance at Liefkenshoek and Antwerpen, but the model performance at Temse can be significantly improved depending on the applied friction values.

Different weights are again assigned to the outcome of the cost function at each tidal station (Table 8) to select a single friction value for the Lower Sea Scheldt friction zone. Higher weights are assigned to the more upstream located tidal stations of Antwerpen and Temse, while lower weights are assigned to the more downstream located tidal stations of Bath and Liefkenshoek. Table 11 gives the outcome of the cost function for the Lower Sea Scheldt friction zone. The best combined model performance for all historical models is obtained with friction coefficients of  $0.015\text{-}0.017 \text{ s}\cdot\text{m}^{-1/3}$  (i.e., cal14, cal15 and cal16). The cost averaged over the four stations along the Lower Sea Scheldt friction zone is lowest for calibration run cal17 with a friction coefficient of  $0.017 \text{ s}\cdot\text{m}^{-1/3}$ . Besides, this calibration run leads to the largest cost reduction at the most upstream located tidal station in the Lower Sea Scheldt friction zone (i.e., Temse) and hence optimizes the model performance at the edge of the Upper Sea Scheldt friction zone.

Figure 24 – Outcome of the cost function for calibration runs cal11, cal12, cal13, cal14, cal15 and cal16 (compared to run cal01) in which the bottom friction coefficients in the Lower and Upper Sea Scheldt are varied.

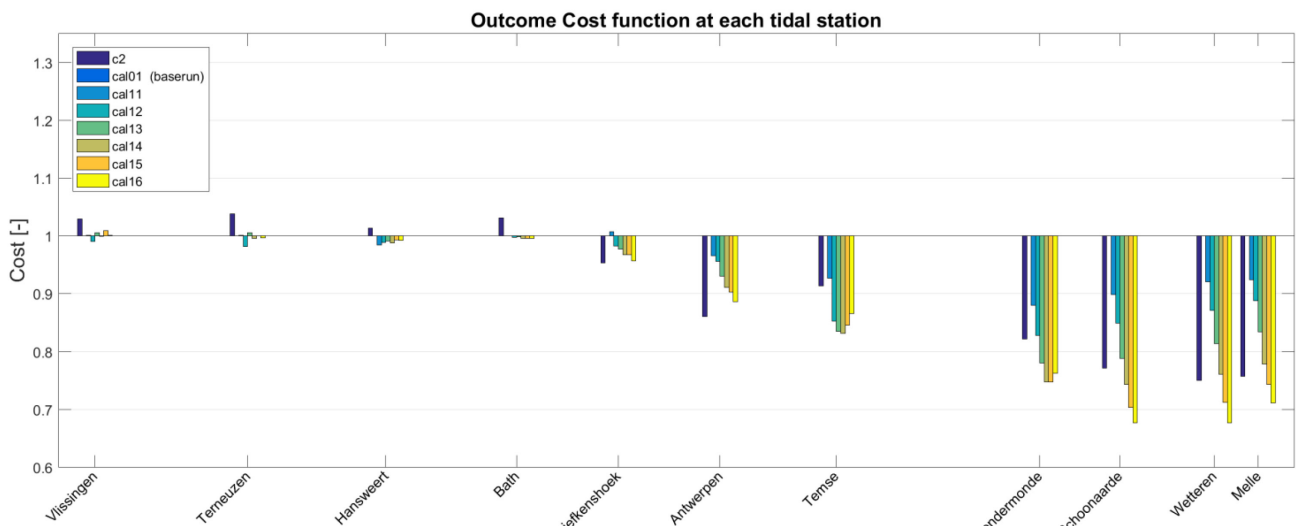


Table 11 – Outcome cost function for the Lower Sea Scheldt friction zone

Calibration run	Combined cost
cal01 (baserun)	1.000
cal11	0.966
cal12	0.933
cal13	0.918
cal14	0.908
cal15	0.910
cal16	0.909
c2	0.922

### Calibration of bottom friction in Upper Sea Scheldt

The calibration of the friction coefficients in the Upper Sea Scheldt consists of five additional simulations in which the bottom friction of the Lower Sea Scheldt and Upper Sea Scheldt is set constant to 0.016, 0.015, 0.014, 0.013 and 0.012  $\text{s}\cdot\text{m}^{-1/3}$  respectively (i.e., calibration runs cal21 – cal25). The bottom friction in the Western Scheldt is kept constant at 0.021  $\text{s}\cdot\text{m}^{-1/3}$ , while the bottom friction in the Lower Sea Scheldt (and Rupel branch) is kept constant at 0.017  $\text{s}\cdot\text{m}^{-1/3}$ . The model results of the calibration runs are compared using the cost function described in §5.1. Calibration run cal14, which gave the best results in the Lower Sea Scheldt friction zone, is used as reference run (or baserun) in this cost function. Figure 25 shows the outcome of the cost function at each tidal station along the estuary.

Figure 25 – Outcome of the cost function for calibration runs cal21, cal22, cal23, cal24 and cal25 (compared to run cal14) in which the bottom friction coefficients in the Upper Sea Scheldt are varied.

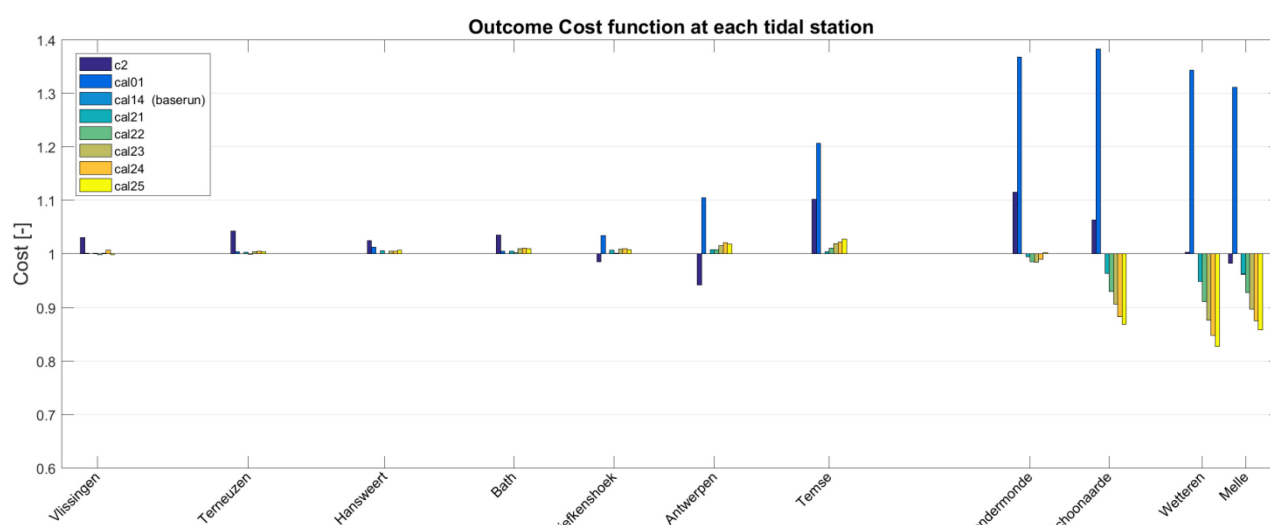


Table 12 – Outcome cost function for the Upper Sea Scheldt friction zone

Calibration run	Combined cost
cal14 (baserun)	1.000
cal21	0.975
cal22	0.953
cal23	0.936
cal24	0.924
cal25	0.916
cal01	1.312
c2	1.038

The model performance up until Antwerpen remains more or less similar to cal01 and cal14 for the additional calibration runs. In the Lower Sea Scheldt, the model performance worsens slightly at Antwerpen and Temse if the bottom friction in the Upper Sea Scheldt is lowered. Conversely, lower bottom friction values improve the model performance in the most upstream located tidal stations in Schoonaarde, Wetteren and Melle. In particular, best combined results at the latter three tidal stations are achieved for the lowest tested bottom friction coefficient (i.e., 0.012  $\text{s}\cdot\text{m}^{-1/3}$ ) in the Upper Sea Scheldt, whereas best

results in the more downstream located tidal stations of Temse and Antwerpen are obtained with a friction coefficient of  $0.017 \text{ s}\cdot\text{m}^{-1/3}$  in the Upper Sea Scheldt section.

As for the previous sections, different weights are again assigned to the outcome of the cost function at each tidal station (Table 8) to select a single friction value for the Upper Sea Scheldt friction zone. Table 11 gives the outcome of the cost function for the Upper Sea Scheldt friction zone. The best combined model performance for all historical models is obtained with the lowest tested friction coefficient of  $0.012 \text{ s}\cdot\text{m}^{-1/3}$  (i.e., cal25). The effect of applying even lower friction coefficients in the Upper Sea Scheldt is not tested in this report.

### Discussion of calibration results based on bottom friction adjustments

Based on the simultaneous model calibration, the average model performance of all five historical models combined is obtained with a Manning coefficient of  $0.021 \text{ s}\cdot\text{m}^{-1/3}$  in the Western Scheldt,  $0.017 \text{ s}\cdot\text{m}^{-1/3}$  in the Lower Sea Scheldt and as low as  $0.012 \text{ s}\cdot\text{m}^{-1/3}$  in the Upper Sea Scheldt. Figure 26 shows the result of the cost function for the calibrated model for all tidal stations relative to the initial Scaldis 2013 bottom friction field. Besides, calibration runs cal01 and cal14 are added to indicate the stepwise improvement of the model performance. In addition, Table 13 gives the outcome of the cost function relative to the initial model simulation (i.e., Scaldis2013 friction field), averaged over the five historical models and equally averaged over all tidal stations (i.e., all tidal stations have the same weight in the cost function). Based on the cost function (i.e., relative change in RMSE-values of HW, LW,  $T_{\text{HW}}$  and  $T_{\text{LW}}$ ) the model calibration resulted in a small improvement of the model performance in the Western Scheldt up until Bath. The RMSE-values for HW and LW itself remain within approximately 0.10 m in the Western Scheldt for all historical models (see: Figure 94 - Figure 103), although slightly higher RMSE-values of up to 0.20 m are present in Bath for the 1930, 1960 and 1980 models. RMSE-values for  $T_{\text{HW}}$  and  $T_{\text{LW}}$  along the Western Scheldt vary between 5 and 15 minutes for all historical models. Between Liefkenshoek and Antwerpen, the calibrated model performs worse than the initial model simulation. Apparently, using a single constant friction coefficient in this section is not sufficient to obtain a similar model accuracy as with the more spatially refined friction field of the Scaldis 2013 model. The RMSE-values of the calibrated models at Liefkenshoek and Antwerpen are generally somewhat higher, especially for the 1930, 1960 and 1980 models. Further upstream, significant improvement of the model performance is obtained by lowering the bottom friction coefficients in the Upper Sea Scheldt to  $0.012 \text{ s}\cdot\text{m}^{-1/3}$ . The RMSE of the HW and LW generally increases along the most upstream part of the Sea Scheldt, where the highest RMSE values are found at the Wetteren and Melle tidal stations. For the 1930, 1960 and 1980 models, HW and LW RMSE values increase up to about 0.25 m and 0.50 m respectively. For the 2001 and 2013 models, HW and LW RMSE values remain somewhat lower and increase up to approximately 0.15 m and 0.25 m respectively. Nevertheless, the average model performance of the five historical models combined has improved significantly in the Upper Sea Scheldt with respect to the initial Scaldis 2013 bottom friction field (Figure 26).

The model performance of each individual historical model (i.e., each year) with the newly calibrated bottom friction coefficients is assessed in the model validation in Section 6.

Figure 26 – Outcome of the cost function for calibration runs cal01, cal14 and cal25 relative to initial model simulation c2.

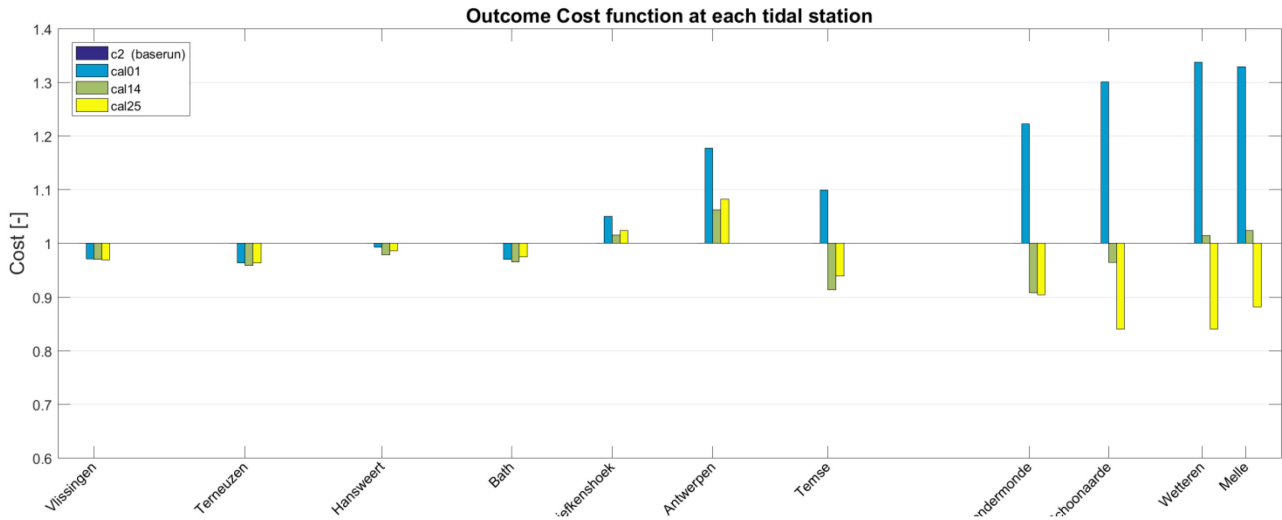


Table 13 – Outcome cost function equally averaged over the five historical models and over all tidal stations.

Calibration run	Combined cost
c2 (baserun)	1.000
cal01	1.129
cal14	0.980
cal25	0.946

## 6 Model validation

The individual validation of the five historical models is presented in this section.

For each historical model, the mean errors of the high waters and low waters are assessed at the same tidal stations as in the model calibration based on a separate validation run. In particular, these validation runs comprise two full spring neap cycles (i.e., 28 days) and hence are twice as long as the calibration runs in Section 5. The selection of the specific simulation periods is discussed in §4.6.1. As full time series of water level measurements are not available for some of the historical models, the model validation is only based on high and low water levels. The mean errors or BIAS-values of the high water levels (BIAS HW), low water levels (BIAS LW), as well as of the high water timing (BIAS  $T_{HW}$ ) and low water timing (BIAS  $T_{LW}$ ) are calculated for each validation run. These parameters give insight on the representation of the tidal propagation and damping or amplification of the tidal wave along the estuary. Besides, RMSE-values were already presented in Section 5 on the model calibration and presented in Appendix 10.6.

### 6.1 1930 model

Figure 27 depicts the HWL and LWL BIAS and the  $T_{HW}$  and  $T_{LW}$  BIAS of the historical 1930 model with the newly calibrated friction field.

The representation of the high and low waters is considered good in the Western Scheldt and Lower Sea Scheldt (i.e. up until Temse). Mean errors on the high- and low water levels remain within  $\pm 0.10$  m. Phase errors of the high and low water levels remain within 5-15 minutes, with the highest phase lag between Bath and Antwerpen. The performance of the 1930 model is slightly worse in the Upper Sea Scheldt, where the mean error of the low water levels shifts from -0.20 m in Dendermonde to almost +0.40 m in Melle. Conversely, high water level errors remain within +0.05 to +0.15 m, implying that the model overestimates the damping of the tidal range along this upstream estuary section. The high water phase errors increase slightly along the Upper Sea Scheldt from +10 minutes in Dendermonde to +25 minutes in Wetteren, whereas the low water phase errors remain between -5 and +10 minutes.

In conclusion, the 1930 reproduces the observed high and low waters along the estuary, except for the overestimated low waters (i.e., overestimated tidal damping) along the most upstream part of the estuary.

### 6.2 1960 model

Figure 28 shows the HWL and LWL BIAS and the  $T_{HW}$  and  $T_{LW}$  BIAS of the historical 1960 model with the bottom friction field as calibrated in Section 5.

The representation of the high and low water levels in the 1960 model is characterized by a common overestimation (i.e., both high- and low water levels are overestimated) in the Lower Sea Scheldt. This mean water level overestimation develops from Hansweert onwards, peaks between Liefkenshoek and Antwerpen where high- and low water levels are overestimated by up to +0.20 m and diminishes towards Temse. Further upstream, the tidal damping along the Upper Sea Scheldt is highly overestimated in the 1960 model. In particular, mean errors of the modelled high water levels change from +0.05 m in Dendermonde to -0.20 m in Wetteren, while the mean errors of the modelled low water levels shift from +0.05 m to as high as +0.35 m along the same estuary stretch. The representation of the high- and low water phase along the estuary is much better as mean errors on the high water phase are within  $\pm 10$  minutes at all tidal stations and mean errors on the low water phase develop from  $\pm 5$  minutes in the

Western Scheldt up to +20 minutes at Wetteren in the Upper Sea Scheldt. Nota that the 1960 model could not be validated at the most upstream tidal station of Melle due to a lack of data.

Overall, the model performance of the historical 1960 model is considered to be limited, with poor representations of the along-estuary variation in high- and low water levels in the Lower and Upper Sea Scheldt.

Figure 27 – HW BIAS, LW BIAS, THW BIAS and TLW BIAS for the 1930 model with the calibrated friction field from simulation cal25.

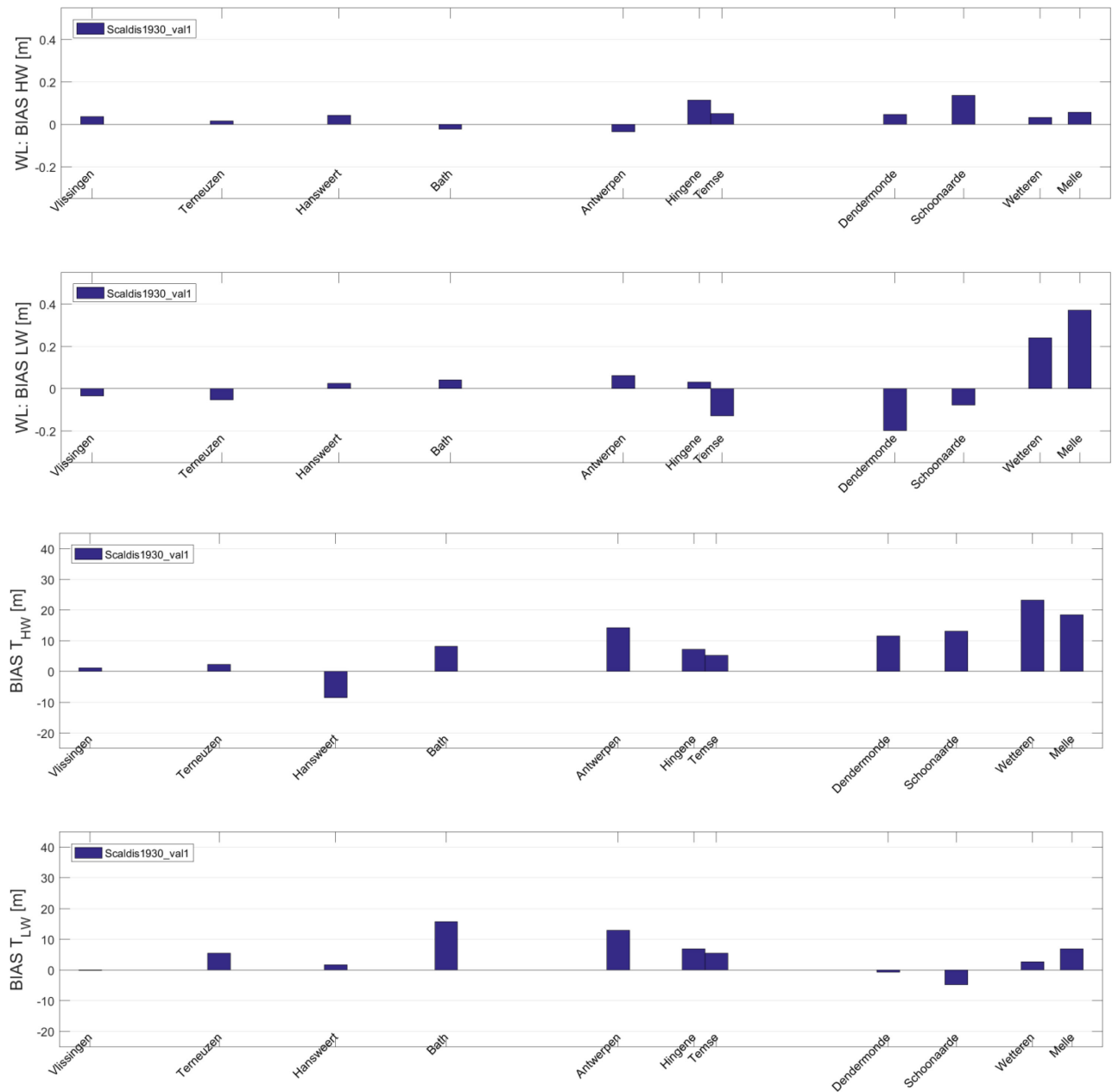
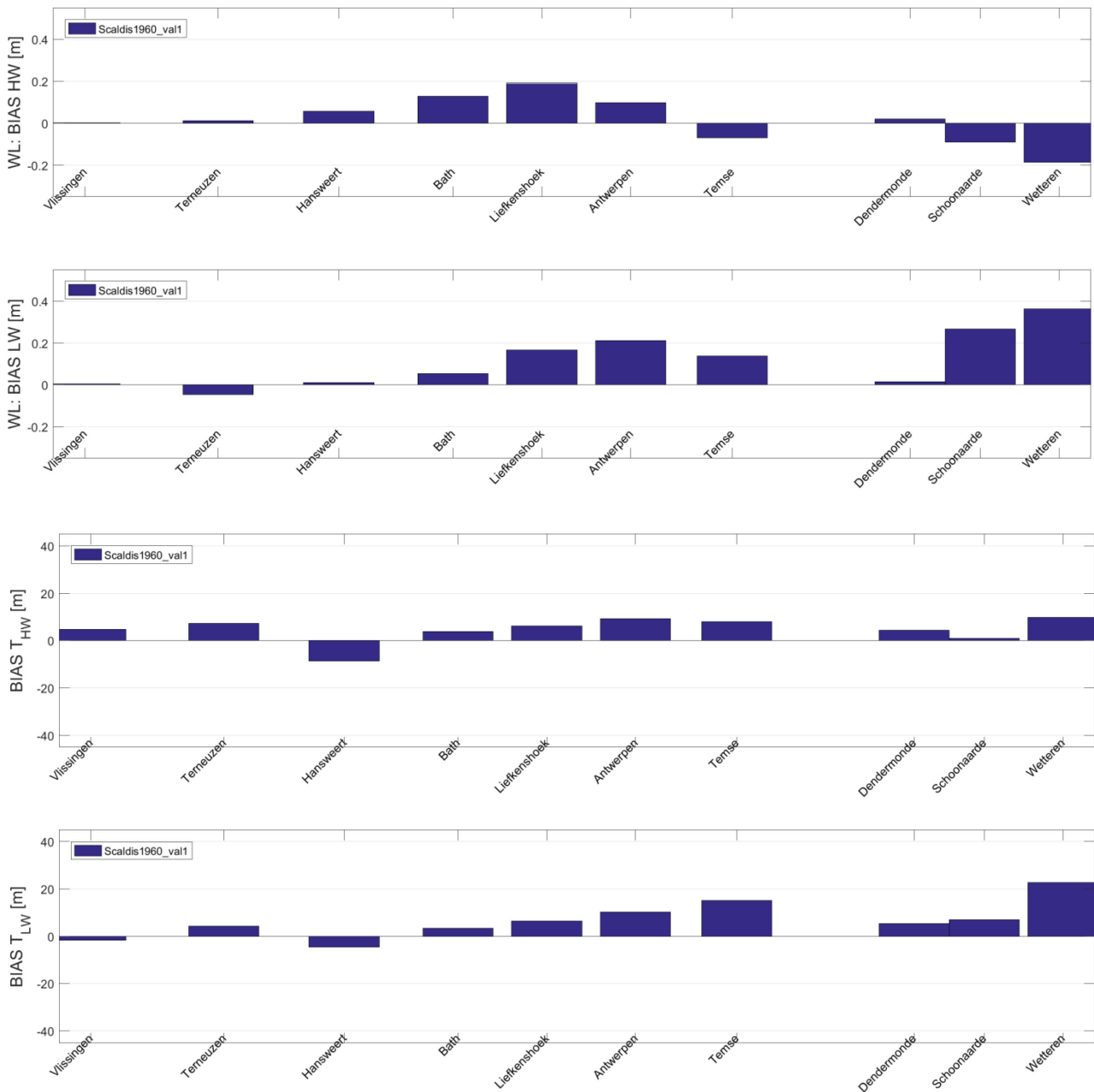


Figure 28 – HW BIAS, LW BIAS, THW BIAS and TLW BIAS for the 1960 model with the calibrated friction field from simulation cal25.



### 6.3 1980 model

Figure 29 shows the HWL and LWL BIAS and the  $T_{HW}$  and  $T_{LW}$  BIAS of the calibrated historical 1980 model with the simultaneously calibrated friction field.

The model performance of the historical 1980 model is characterized by a continuous underestimation of the tidal range throughout the estuary. Even at the most downstream tidal station of Vlissingen, high water levels are underestimated and low water levels are overestimated. Hence, the model performance is affected by the downstream boundary condition, in which the tidal range is not well represented. The underestimation of the tidal range increases along the estuary and is strongest in the most upstream part. Although the 1980 model underrepresents the tidal range throughout the estuary, the model captures the development of high and low waters along the Western Scheldt and Lower Sea Scheldt fairly well. However,

the model performance is poor in the Upper Sea Scheldt, where especially low waters are not well represented. In particular, the mean error on high water levels at Melle increases up to -0.15 m and on low water levels up to +0.55 m at Melle. The underestimation of the tidal range along the estuary is thus mainly the result of higher low waters, rather than lower high waters. The mean phase errors along the estuary remain within  $\pm 15$  minutes for the high waters and within  $\pm 10$  minutes for the low waters. The most upstream tidal stations are again an exception, as phase errors increase to about +20 minutes and +35 minutes for high and low waters respectively.

Overall, the 1980 model is able to reproduce measured tidal propagation along the Western Scheldt and Lower Sea Scheldt, but that the model performance is influenced negatively by an underestimation of the tidal range at the estuary mouth.

## 6.4 2001 model

Figure 30 depicts the HWL and LWL BIAS and the  $T_{HW}$  and  $T_{LW}$  BIAS of the historical 2001 model with the simultaneously calibrated bottom friction field.

The calibrated 2001 model has a good model performance throughout the estuary. In particular, mean errors on high water levels remain below  $\pm 0.05$  m at all tidal stations, except Wetteren where the model BIAS is approximately +0.10 m. Similarly, low water level BIAS values remain below  $\pm 0.10$  m up until Schoonaarde and increase slightly towards Wetteren and to almost +0.20 m at Melle. Furthermore, the mean phase errors of the high and low waters are all within the simulation's output time step of 10 minutes.

## 6.5 2013 model

Figure 31 depicts the HWL and LWL BIAS and the  $T_{HW}$  and  $T_{LW}$  BIAS of the 2001 model with the simultaneously calibrated bottom friction field.

Based on the BIAS-values of the high and low water levels, the model performance of the 2013 model is good in the Western Scheldt and Lower Sea Scheldt. Mean errors of the high and low water levels are within 0.10 m in this part of the estuary, which is a similar order of accuracy as with the original Scaldis2013 friction field validated by Smolders et al. (2016) (see §5.2). In the Upper Sea Scheldt, the mean errors on high water levels is negligible, but low water levels are underestimated by up to -0.20 m. This underestimation is most probably the result of a high discharge peak, that was present during the simulation period (see Appendix 10.4), and the effect of which is not adequately incorporated in the model's boundary conditions. In particular, the upstream discharge is implemented as a daily average in the 2013 model, implying that the highest discharges are potentially averaged out. The mean phase errors of the high and low waters are all within the output time step of 10 minutes in the newly calibrated 2013 model.

In conclusion, the model performance of the newly calibrated 2013 model regarding tidal propagation along the estuary is considered good. Nevertheless, the performance of the validation run is affected by the presence of a strong discharge peak, the effect of which appears to be underestimated by the model.

Figure 29 – HW BIAS, LW BIAS, THW BIAS and TLW BIAS for the 1980 model with the calibrated friction field from simulation cal25.

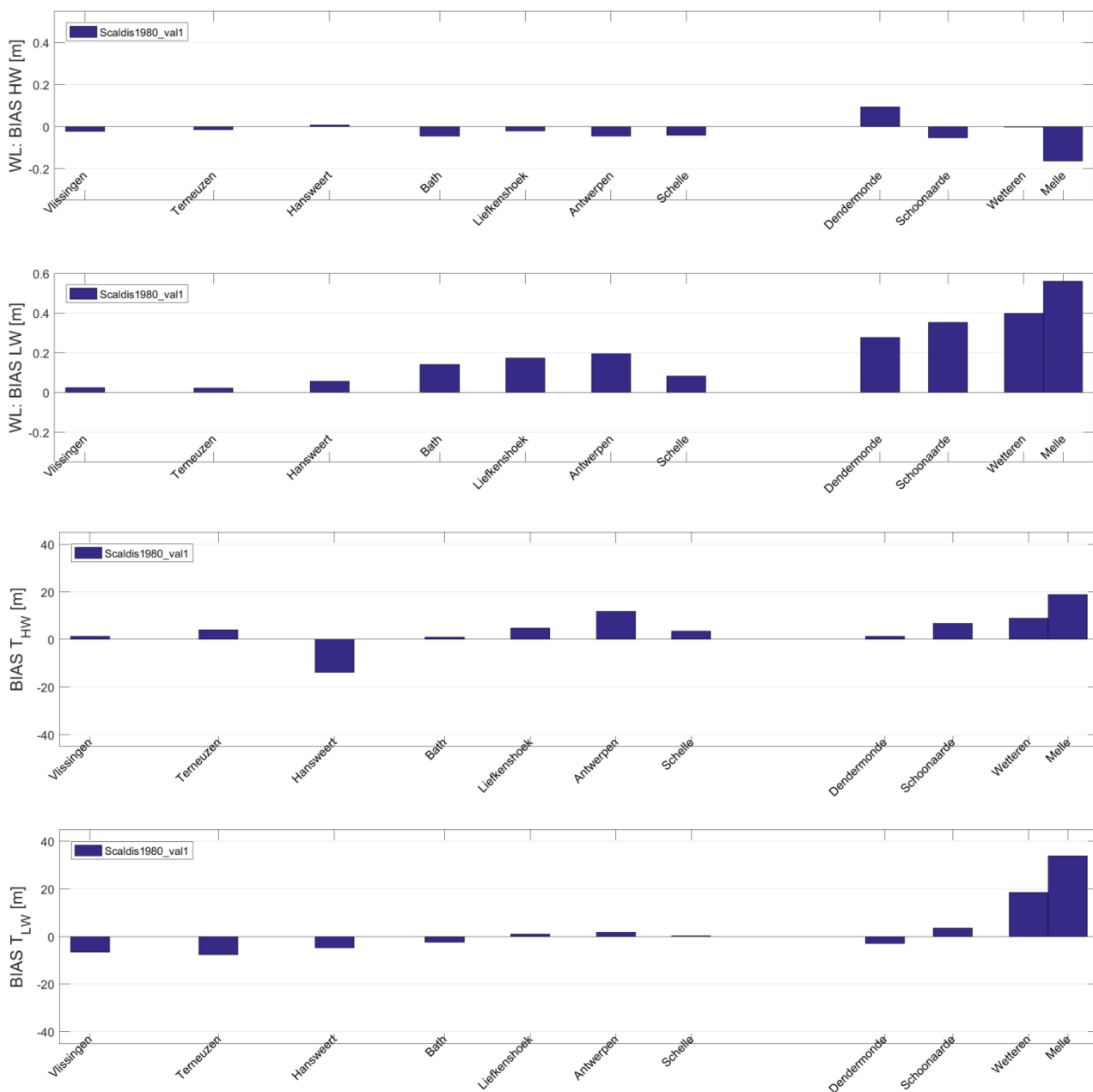


Figure 30 – HW BIAS, LW BIAS, THW BIAS and TLW BIAS for the 2001 model with the calibrated friction field from simulation cal25.

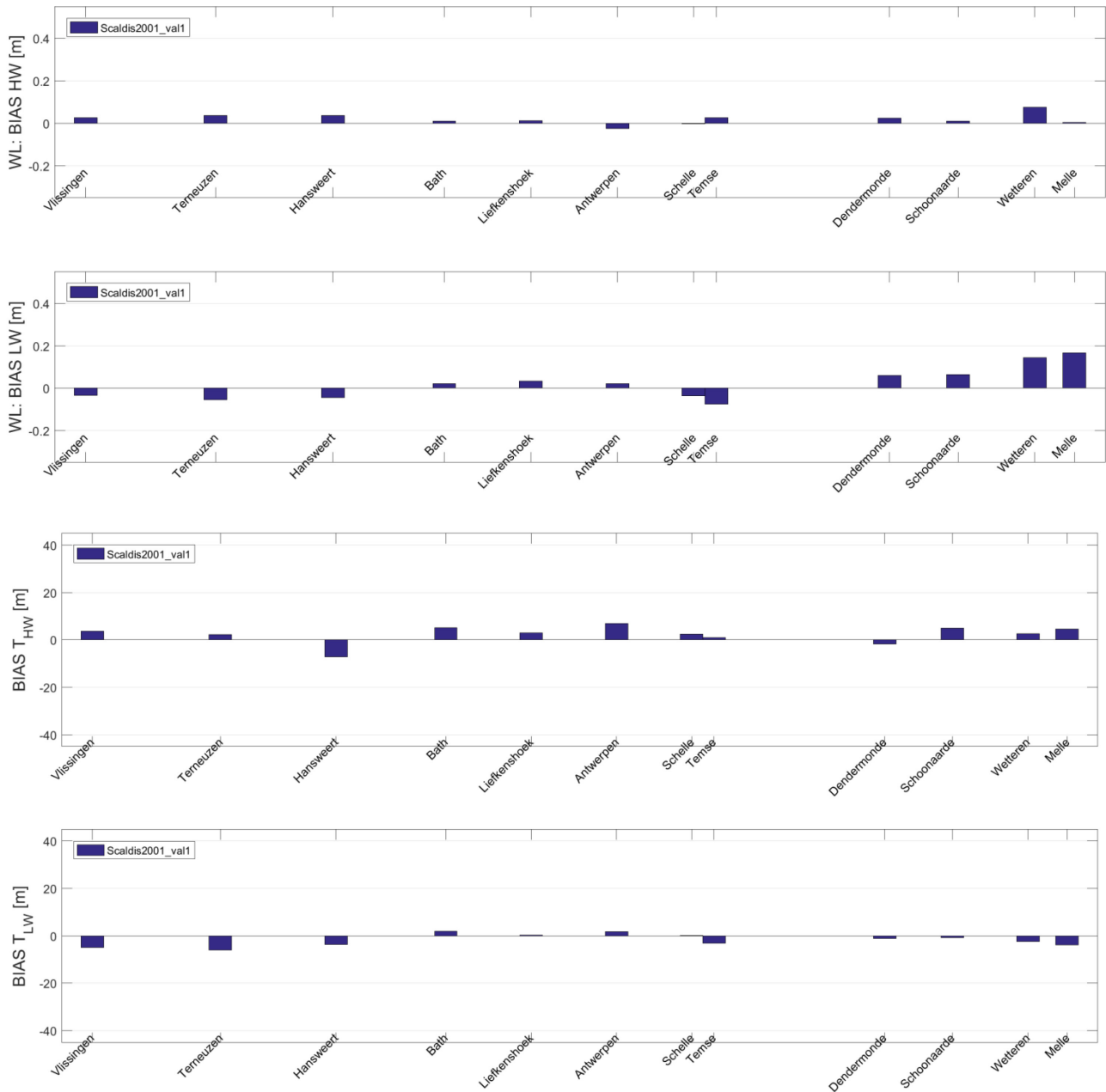
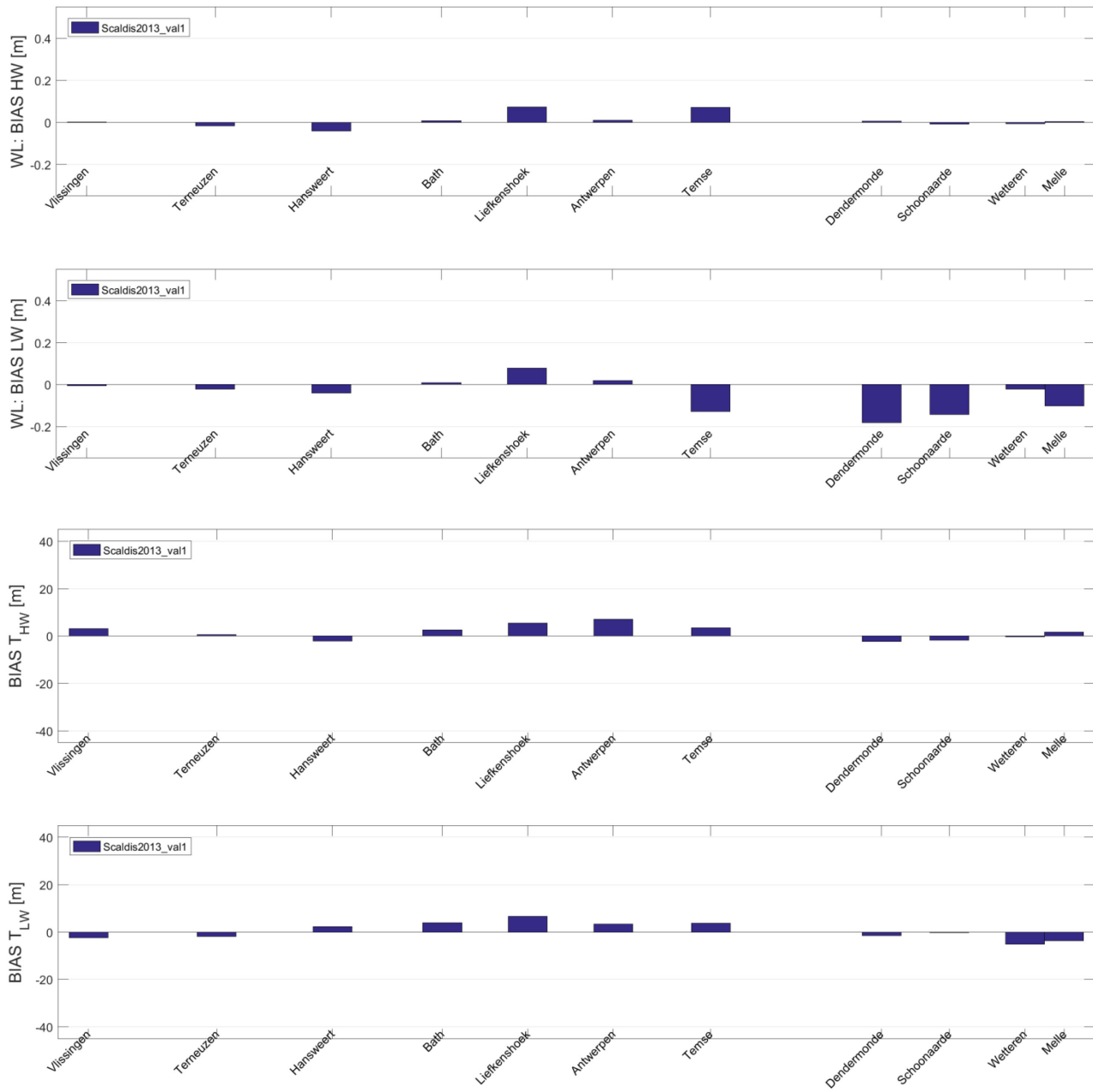


Figure 31 – HW BIAS, LW BIAS, THW BIAS and TLW BIAS for the 2013 model with the calibrated friction field from simulation cal25.



## 6.6 Discussion of the model performance

Although the bottom friction field has been simplified significantly by composing it of three large friction zones, the outcome of the model calibration shows that the model performance averaged over the five historical models improves when using the newly calibrated friction field, compared to the averaged model performance based on the initial Scaldis2013 friction field. Based on the model validation, all models appear to perform well in the Western Scheldt and, except for the 1960 model, also in the Lower sea Scheldt. The model performance of the historical models generally deteriorates in the upstream part of the Upper Sea Scheldt where tidal ranges are mostly underestimated, while the influence of upstream discharge variations on tidal water levels is probably underrepresented.

Overall, the model performance of the 2001 and 2013 models is considered good along the entire Scheldt Estuary transect between Vlissingen and Melle. In particular, mean errors are within  $\pm 0.10$  m and  $\pm 0.15$  m for high- and low water levels respectively and within the output time step of 10 minutes for the high- and low water phase. This implies that the tidal propagation is well-captured along the estuary. However, RMSE values of especially the low water levels appear to increase upstream of Schoonaarde. This might be related to an underestimation of the influence of upstream discharge on the water levels in the most upstream part of the Upper Sea Scheldt. The model performance of the 1930 and 1960 models is considered fairly well along the Western Scheldt and up until around Dendermonde in the Sea Scheldt. Nevertheless, mean errors are up to  $\pm 0.20$  m at some tidal stations and hence are slightly higher than for the 2001 and 2013 models. In particular, the 1960 model generally overestimates both high and low water levels by  $+0.10$  to  $+0.20$  m along a large stretch in the Lower Sea Scheldt from around Bath to Antwerpen. Finally, the model performance of the 1980 model is poor relative to the other models. The 1980 model already underestimates the tidal amplitudes at the estuary mouth (i.e., tidal station of Vlissingen), implying that the representation of the 1980 offshore bathymetry might affect the model results. However, changes in offshore bathymetry are not assessed in this study. As a result, high water levels in the 1980 model are underestimated throughout the estuary and low water levels are underestimated throughout the estuary (i.e., from  $-0.05$  m in the Western Scheldt to  $-0.70$  m in Melle). Nevertheless, the underestimation of the tidal range remains more or less similar along large parts of the estuary up until Schelle, from where the model error increases.

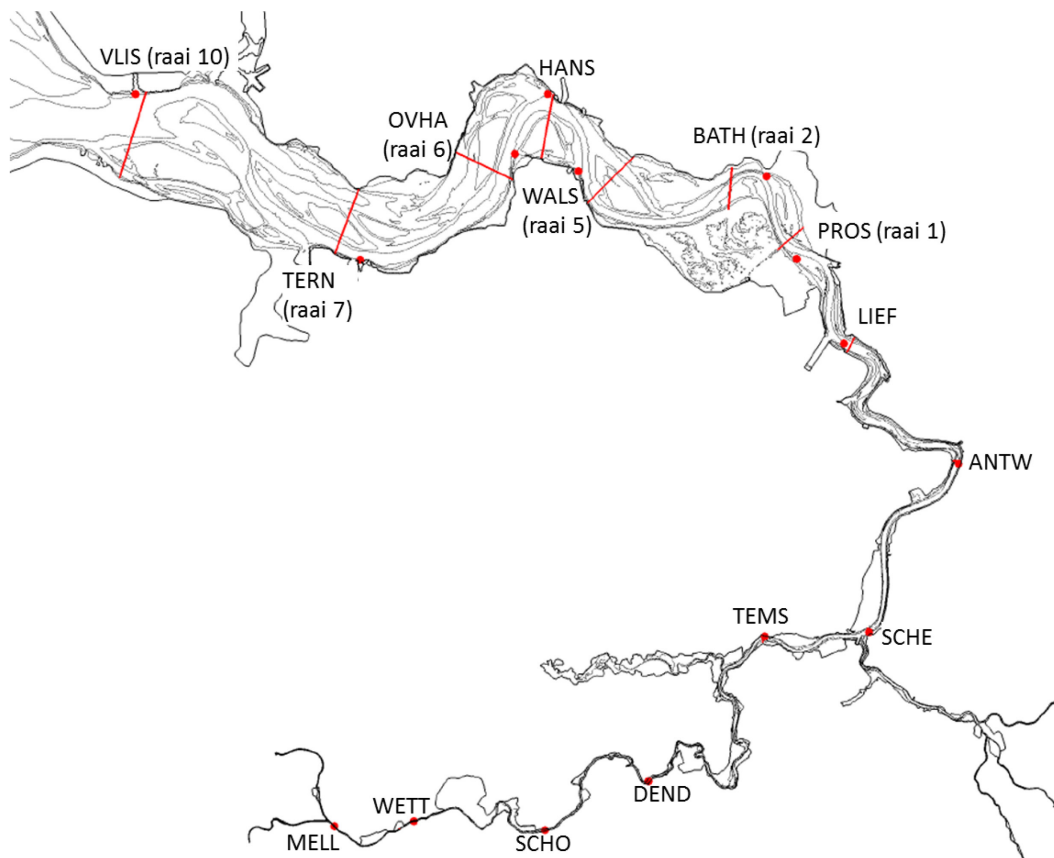
Individual tuning of the bottom friction coefficients in the five historical models or changing other model parameters may further improve the model performance. For example, using even lower friction coefficients in the Upper Sea Scheldt would likely lead to a better representation of the tidal range in this upstream section, but doing so would imply that even more unrealistic friction coefficients would be used. Therefore, such friction coefficients are not tested in the present model calibration. A sensitivity analysis, in which the impact of the artificial viscosity coefficients (i.e., in TELEMAC-3D implemented through the coefficient for horizontal and vertical diffusion of velocities) on the model performance, is assessed is included in Appendix 10.7. However, these sensitivity analyses indicate that altering the user-imposed laminar viscosity by tuning the diffusion coefficients does not improve the model performance in the Upper Sea Scheldt.

## 7 Tidal characteristics

An overview of the computed characteristics of the vertical and horizontal tide for all five historical models is presented in this section.

The locations at which the modelled tidal characteristics are extracted from the model results are shown in Figure 32. They correspond with the locations at which the observed historical tidal characteristics were analyzed (Vandenbruwaene et al., 2019). Some of the cross-sections used for the calculation of characteristics of the horizontal tide (i.e., cross-sectional averaged velocities, discharges, tidal prisms and horizontal asymmetry) correspond to transects at which historical and more recent discharge measurements have been performed in the Western Scheldt (i.e., raai 1 - ... - raai 10) (e.g. De Kramer, 2002).

Figure 32 – Locations and cross-sections at which tidal characteristics are computed



Tidal characteristics of the vertical tide include high water levels, low water levels, tidal range, celerity of the tidal wave and vertical tidal asymmetry. In particular, the vertical tidal asymmetry is defined as the ratio between the duration of the falling tide and the duration of the rising tide ( $T_{fall}/T_{rise}$ ). Besides, the tidal wave celerity is calculated based on the propagation speed of high water levels ( $c_{HW}$ ) and low water levels ( $c_{LW}$ ).

Properties of the horizontal tide include velocities, tidal discharges, the tidal prism as well as tidal asymmetry based on the maximum flood and ebb velocities and based on the normalized third-order velocity moment. cross-sectional averaged velocities are extracted from the model results to analyze the horizontal tidal characteristics. Consequently, the horizontal tidal asymmetry is defined as the ratio

between the peak cross-sectional averaged velocity during flood and the peak cross-sectional averaged velocity during ebb ( $V_{FL-max}/V_{EB-max}$ ).

Finally, the normalized third-order velocity moment ( $\gamma_0$ ) gives an indication of horizontal tidal asymmetry based on the entire velocity time series. This parameter is calculated as the third-order velocity moment, normalized by the second moment to the 1.5<sup>th</sup> power (e.g. Nidzieko and Ralston, 2012; Stark et al., 2017):

$$\gamma_0 = \frac{\mu_3}{(\mu_2)^{1.5}} = \frac{\frac{1}{t} \sum_{j=1}^t V_{cs}(j)^3}{\frac{1}{t} \sum_{j=1}^t (V_{cs}(j)^2)^{1.5}}$$

in which  $\mu_3$  and  $\mu_2$  are the third-order and second-order velocity moments respectively,  $V_{cs}(j)$  [m/s] represents the cross-sectional averaged velocity on time step  $j$  and  $t$  is the total number of time steps. Velocities are considered positive in flood-direction and negative in ebb-direction so that positive values of  $\gamma_0$  denote flood-dominance and negative values of  $\gamma_0$  denote ebb-dominance. While  $V_{FL-max}/V_{EB-max}$  is only based on peak velocities,  $\gamma_0$  considers the entire time series of cross-sectional averaged velocities.

Furthermore, it should be stated that the computed model results in this study should not necessarily correspond with the data analysis presented by Vandenbruwaene et al. (2019) as the model results are only computed over a one month simulation, whereas the observed data are mostly yearly averages. A comparison between the yearly averaged high, low and mean water levels and the high, low and mean water levels during the simulation periods is given in Table 5. The statement also holds for the results in the most upstream part of the Upper Sea Scheldt as tidal characteristics over there are potentially influenced by upstream discharge variations. Moreover, model results in this part of the estuary could be affected by the poor model performance in that part of the estuary as well.

## 7.1 Vertical tide

### High water levels

In accordance with the data analysis by Vandenbruwaene et al. (2019), the model results show that mean high water levels throughout the estuary generally increase over the period of interest (Figure 33). Over the full analyzed period from 1930 until 2013, the strongest mean high water level increase of 0.53 m is modelled at Temse. However, the fastest mean high water level increase of approximately 2.1 cm/yr is modelled at Melle between 1980 and 2001. Exceptions to the continuous high water level increase are the most upstream tidal stations in the Upper Sea Scheldt, where mean high water levels first decrease between 1930 and 1960, after which they increase again. This might be related to the poor model performance of especially the 1960 and 1980 models in this part of the estuary, for which these models strongly overestimate the damping of the tidal wave.

### Low water levels

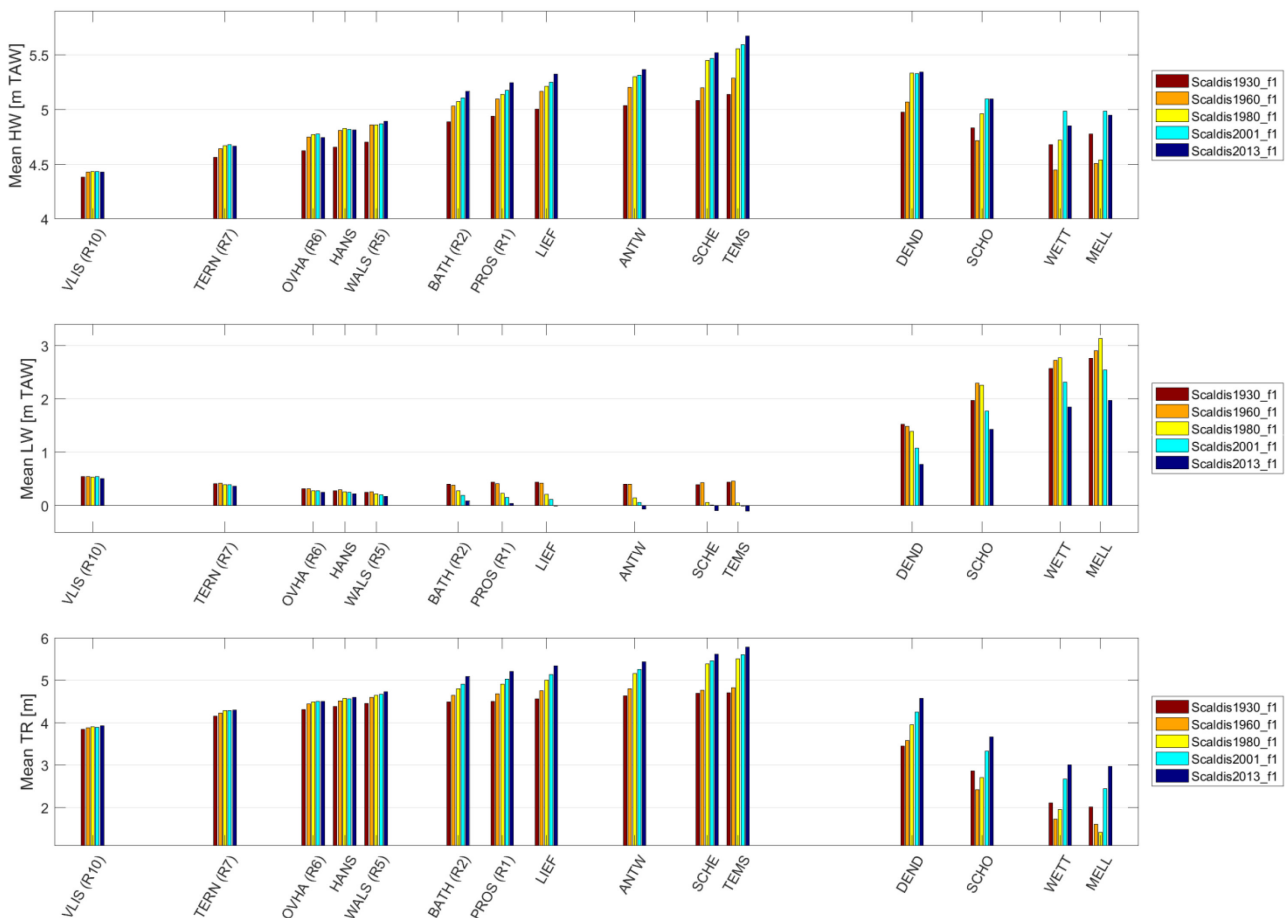
In contrast to the continuous increase of the mean high water levels, the modelled mean low water levels generally decrease over time (Figure 33). In this perspective, it should be stated that the continuous low water decrease in the Western Scheldt does not correspond with the data analyses by Vandenbruwaene et al. (2019) and Kuijper & Lescinski (2012). Moreover, analysis of the imposed boundary conditions shows that the 1930 and 1960 boundary conditions contain relatively high water levels compared to the yearly averages, whereas the 2001 and 2013 boundary conditions are more representative for the full years (Table 5). In particular, they describe a low water level increase of a few centimeters at the tidal stations of Vlissingen, Terneuzen and Hansweert based on high- and low water level observations. An exception is the upstream part of the Upper Sea Scheldt (i.e., Schoonaarde, Wetteren and Melle) where mean low water first increase between 1930 and 1980, after which they decrease towards 2001 and 2013. However, the

representation of low water levels in this section is influenced by the poor model performance of especially the 1960 and 1980 models in this part of the estuary. In particular, these historical models strongly overestimate the damping of the tidal wave in the Upper Sea Scheldt. Besides, the strongest high water level decrease of 3.5 cm/yr on average is modelled between 1980 and 2013 at Melle.

### Tidal range

The modelled development of the mean tidal range over the period of interest (Figure 33) is obtained by superposition of the development of the difference between mean high- and low water levels. This implies that the modelled mean tidal range continuously increases over time at most stations along the estuary, except at Schoonaarde, Wetteren and Melle where the tidal range decreases first between 1930 and 1960 or 1980 and only increases afterwards. In all historical models, the highest tidal range is modelled at Temse. This is also the tidal station where the model results give the strongest increase in tidal range over the entire analyzed period (i.e., 1.08 m or 1.3 cm/yr on average between 1930 and 2013). The fastest tidal range increase is modelled at Melle between 1980 and 2001 (i.e., 4.9 cm/yr). However, the latter value might be affected by the poor model performance at Melle as the tidal range was underestimated throughout the estuary in the 1980 model.

Figure 33 – Modelled historical development in mean high water level (top), mean low water level (mid) and mean tidal range (bottom).



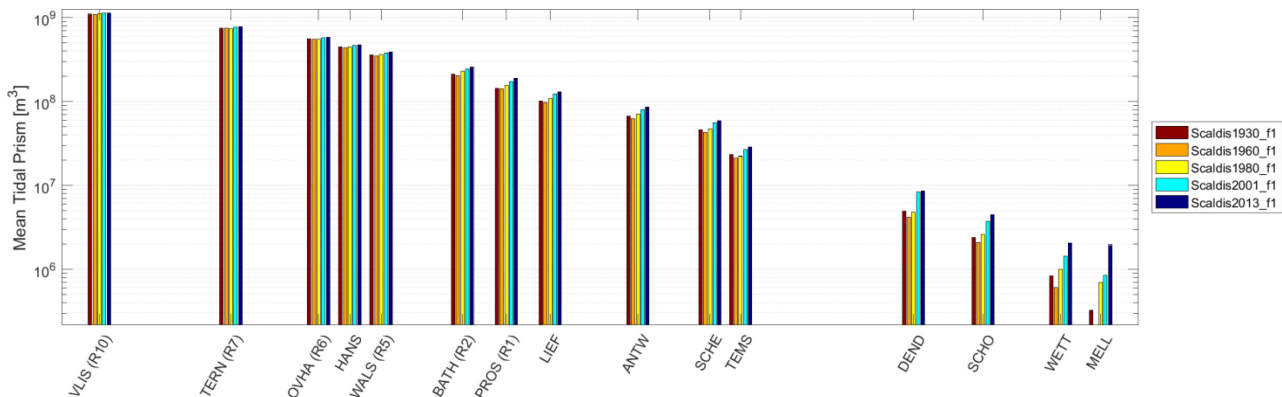
## 7.2 Horizontal tide

### Tidal prism

The modelled development in mean tidal prism  $P$  over the period of interest is shown in Figure 34. The tidal prism is naturally decreasing along the estuary in a landward direction. Model results show that the mean tidal prism decreases first between 1930 and 1960 at all locations, except at Terneuzen. From 1960 onwards, or from 1980 onwards at some locations, the modelled tidal prism increases again. The relative tidal prism decrease between 1930 and 1960 is stronger upstream. Similarly, the tidal prism increase from 1960 onwards is also stronger in the upstream part of the estuary. In particular the tidal prism at Melle decreases from  $0.32 \cdot 10^6 \text{ m}^3$  in 1930 to  $0.22 \cdot 10^6 \text{ m}^3$  in 1960 (i.e., -31% in 30 years) and increases again to  $1.95 \cdot 10^6 \text{ m}^3$  in 2013, implying almost a tenfold increase in 53 years. Over the same period between 1960 and 2013, the relative tidal prism increase downstream in the Western Scheldt was much smaller and varied between +4% in Vlissingen up to +21% in Bath.

The modelled mean tidal prisms of approximately  $1.1 \cdot 10^9 \text{ m}^3$  at Vlissingen (raai 10),  $7.4\text{-}7.8 \cdot 10^8 \text{ m}^3$  at Terneuzen (raai 7) and  $2.0\text{-}2.5 \cdot 10^8 \text{ m}^3$  at Bath (raai 2) are similar to the measured tidal prisms based at discharge transects along the Western Scheldt (i.e., raai 1 - ... - raai 10) presented by e.g. De Kramer (2002), although the measured tidal prisms as presented by De Kramer (2002) were integrated over both flood and ebb and hence are therefore a factor 2 higher. Besides, the modelled mean tidal prisms in this study do also closely match mean tidal prisms for the 1991-2000 period that were calculated by Plancke et al. (2014) based on observed water levels and upstream discharges using the so-called cubature method.

Figure 34 – Modelled historical development in mean tidal prism.



### Velocities

The modelled development of the mean cross-sectional averaged velocities during flood and mean cross-sectional averaged velocities during ebb for mean tide are shown in Figure 35 for all locations along the estuary. Similarly, the modelled development of the peak cross-sectional averaged flood and ebb velocities during mean tide are shown in Figure 36.

The model results indicate an along-estuary variation in the mean cross-sectional averaged velocities. Both flood and ebb velocities are relatively high near the estuary mouth, decrease somewhat towards Bath, increase again along the Lower Sea Scheldt up towards Temse and significantly decrease further upstream in the Upper Sea Scheldt. The latter holds especially for the historical model results and less for the more recent model simulations. In particular, the highest mean flood and mean ebb velocities of almost 0.8 m/s are found for the 1930 model at Schelle, where the tidal range is also highest in all models. On the other

hand, the lowest mean flood and mean ebb velocities are modelled in the Upper Sea Scheldt, where the tidal range strongly decreases.

Besides, the modelled mean flood velocities closely match the modelled mean ebb velocities in the Western Scheldt for all five historical models (i.e., differences between mean flood and mean ebb velocities are all within 0.02 m/s). An exception is discharge raai 5 near Walsoorden where ebb velocities are higher than flood velocities (i.e., up to 0.06 m/s higher for ebb). Remarkably, the modelled mean flood velocities are slightly higher than mean ebb velocities in the Lower Sea Scheldt between Antwerpen and Schelle (i.e., on average 0.03-0.05 m/s higher during flood). Further upstream in the Upper Sea Scheldt, mean ebb velocities are always higher than mean flood velocities. This can of course be related to the larger influence of the upstream discharge on the ebb and flood volumes in this part of the estuary.

When the maximum cross-sectional averaged velocities during flood and ebb are assessed, it follows that peak flood velocities are higher than peak ebb velocities and at almost every location for all five historical models (Figure 36). The only exceptions are the 1930 and 1960 models, in which peak ebb-velocities are higher at Melle. The highest cross-sectional averaged peak velocities of approximately 1.1-1.2 m/s during flood and 0.9-1.0 m/s during ebb are modelled at Terneuzen and Schelle. The lowest cross-sectional averaged peak velocities of 0.2-0.6 m/s are modelled for the most upstream cross-sections at Wetteren and Melle.

Furthermore, the model results suggest that mean and maximum velocities increase over time in the Upper Sea Scheldt where the more recent models clearly give higher maximum velocities during both flood and ebb. Contrastingly, in the Lower Sea Scheldt (i.e., from Bath up until Temse), peak flood velocities are higher for the earlier 1930 or 1960 models. This also holds for the peak ebb velocities and the mean ebb and flood velocities at Schelle. The most downstream cross-sections in the Western Scheldt do not show any clear trends over time.

Figure 35 – Modelled historical development in mean cross-sectional averaged flood velocities (top) and maximum cross-sectional averaged ebb-velocities (bottom) for mean tide.

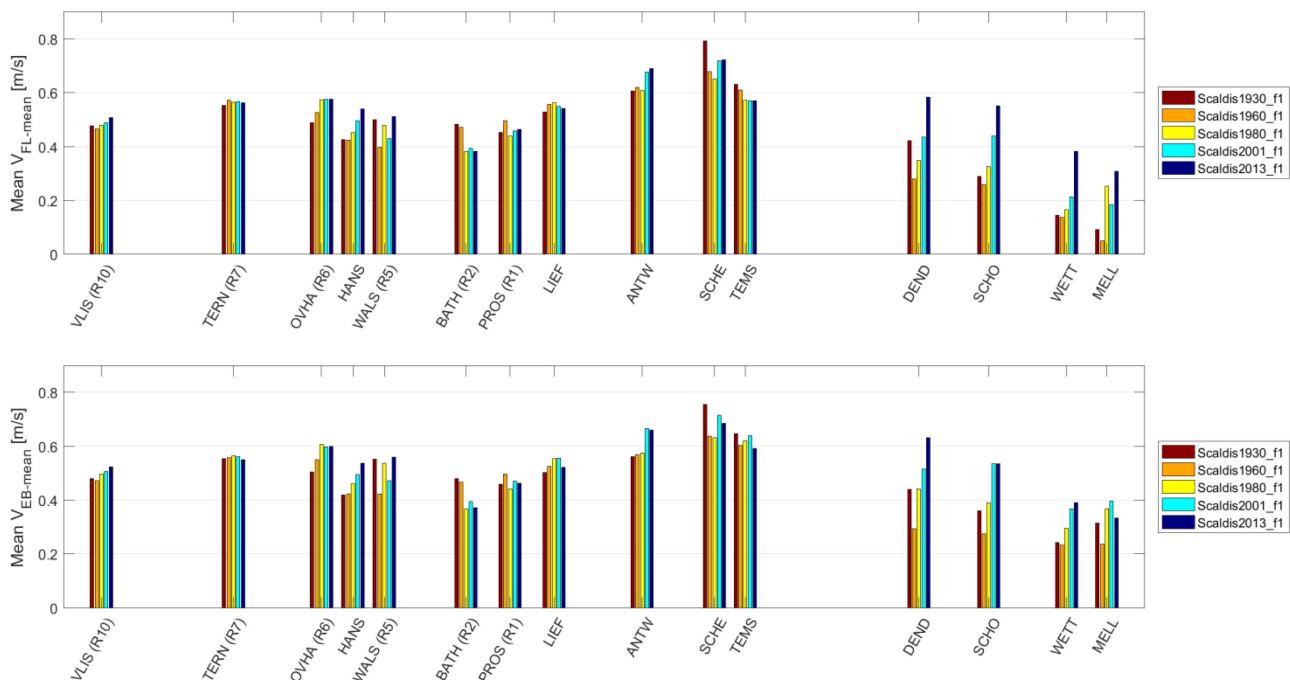
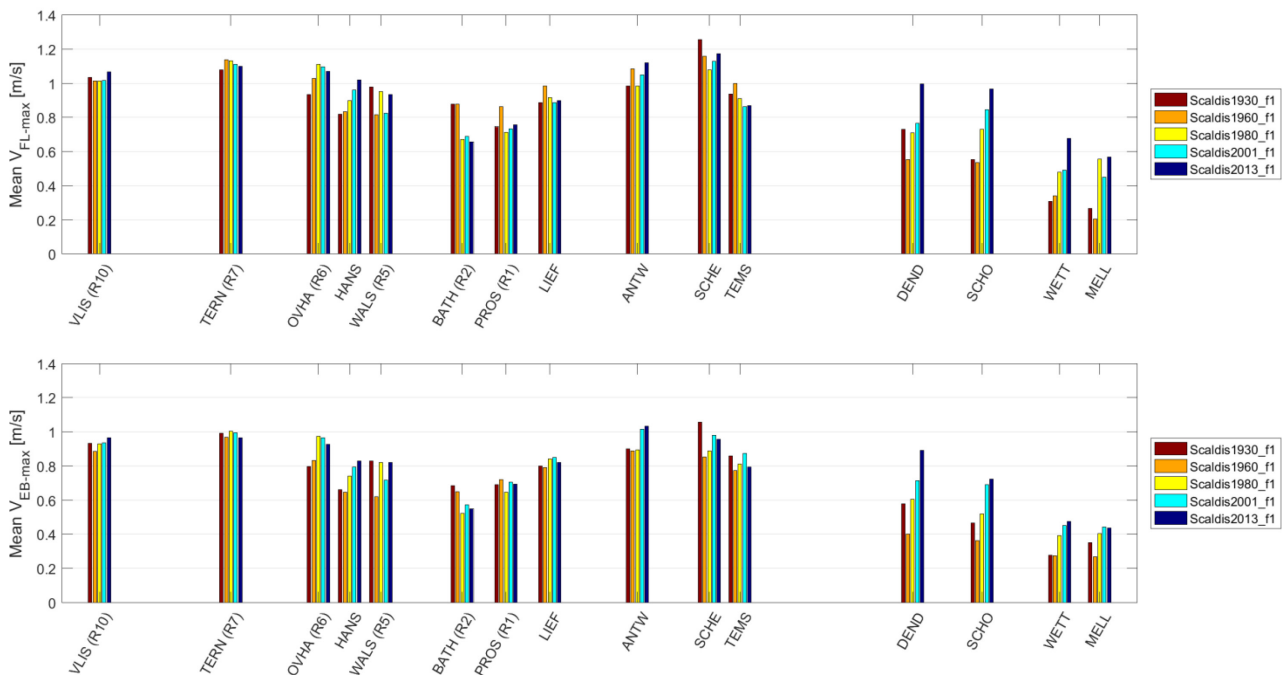


Figure 36 – Modelled historical development in maximum cross-sectional averaged flood velocities (top) and maximum cross-sectional averaged ebb-velocities (bottom) for mean tide.



### 7.3 Tidal wave celerity

#### High tide propagation

The propagation of the high tide is depicted in Figure 37 by means of the mean high water delay  $\Delta T_{HW}$  at each location relative to Vlissingen and in Figure 38 by means of the mean tidal wave celerity  $c_{HW}$  between subsequent locations. The latter is computed by dividing the high water delay between two stations by the along-estuary distance between them. It should be stated that the calculated tidal wave celerity over some of the shorter transects (i.e., nearby subsequent tidal stations) is based on high- or low water phase differences that are of the same order as the output time step of the model (i.e., 10 minutes). This might affect the calculated tidal wave celerity. In addition, Figure 39 shows a comparison between the model results and the historical evolution of the high water celerity and low water celerity based on analyses of historical high and low water measurements by Vandenbruwaene et al. (2019).

Figure 37 clearly shows that the high tide propagation speed increased over time in the upstream part of the estuary, which is in accordance with the findings of Vandenbruwaene et al. (2019). In particular,  $\Delta T_{HW}$  is reduced by over 60 minutes at Melle. The development of  $\Delta T_{HW}$  is slightly different in the Western Scheldt, where the high water delay increases again in the most recent period between 2001 and 2013, implying a development towards a slower tidal propagation in that part of the estuary. In general, the tidal wave celerity varies significantly along the Western Scheldt and Lower Sea Scheldt. The high water celerity is highest between Vlissingen and Terneuzen and between Bath and Liefkenshoek (i.e., 15-22 m/s) and much lower in between Terneuzen and Bath (i.e., about 8-15 m/s). In the 2013 model however, the high water celerity is also high from Walsoorden onwards. The celerity reduces towards the Upper Sea Scheldt where it drops to approximately 5 m/s based on the high water propagation. Based on Figure 39, which shows the calculated tidal wave celerity based on observed high- and low waters, the model captures the observed historical development of the high water celerity fairly well between Liefkenshoek and Melle. However, the high water celerity is generally overestimated between Vlissingen and Hansweert and underestimated towards Liefkenshoek. In accordance with findings of Vandenbruwaene et al. (2019) based

on data analysis, the high water celerity generally increases over time at most locations. Nevertheless, the high water celerity peaks in 2001 between Vlissingen and Overloop van Hansweert and in 1960 between Overloop van Hansweert and Walsoorden. The strongest increase in high water celerity is modelled Walsoorden-Bath section (i.e., 7.2 m/s in 1930 to 16.9 m/s in 2013). This increase occurred almost entirely during the most recent interval between 2001 and 2013, indicating a very strong impact on the tidal wave celerity in this section over just a few years.

### Low tide propagation

As for the high tide propagation, the propagation of the low tide is depicted in Figure 37 by means of the low water delay  $\Delta T_{LW}$  at each location relative to Vlissingen and in Figure 38 by means of the tidal wave celerity  $c_{LW}$  between subsequent locations. The latter is again computed by dividing the low water delay between two stations by the along-estuary distance between them. The low tide propagation is slower than the high tide propagation in all historical models, which corresponds to the findings in the data analysis by Vandenbruwaene et al. (2019). Similar to that analysis, the tidal wave celerity based on the low waters also increases over time. In particular, at the most upstream tidal station of Melle, the low water delay relative to Vlissingen decreases by over 120 minutes between 1960 and 2013. The observed historical development of the low water celerity is quite well captured by the model results (Figure 39). The strongest increase in low water wave celerity is modelled at the Bath-Prosperpolder section, where the low water celerity increased from 8.3 m/s in 1930 to 16.4 m/s in 2013. The latter is also the highest modelled tidal wave celerity based on low water propagation in the estuary. The slowest low water wave celerity of 3-6 m/s depending on the section and historical model is modelled in the Upper Sea Scheldt, where the water depth is also lower.

Figure 37 – Modelled historical development in mean tidal propagation for high tide (top) and low tide (bottom), expressed as the phase difference at each location with Vlissingen.

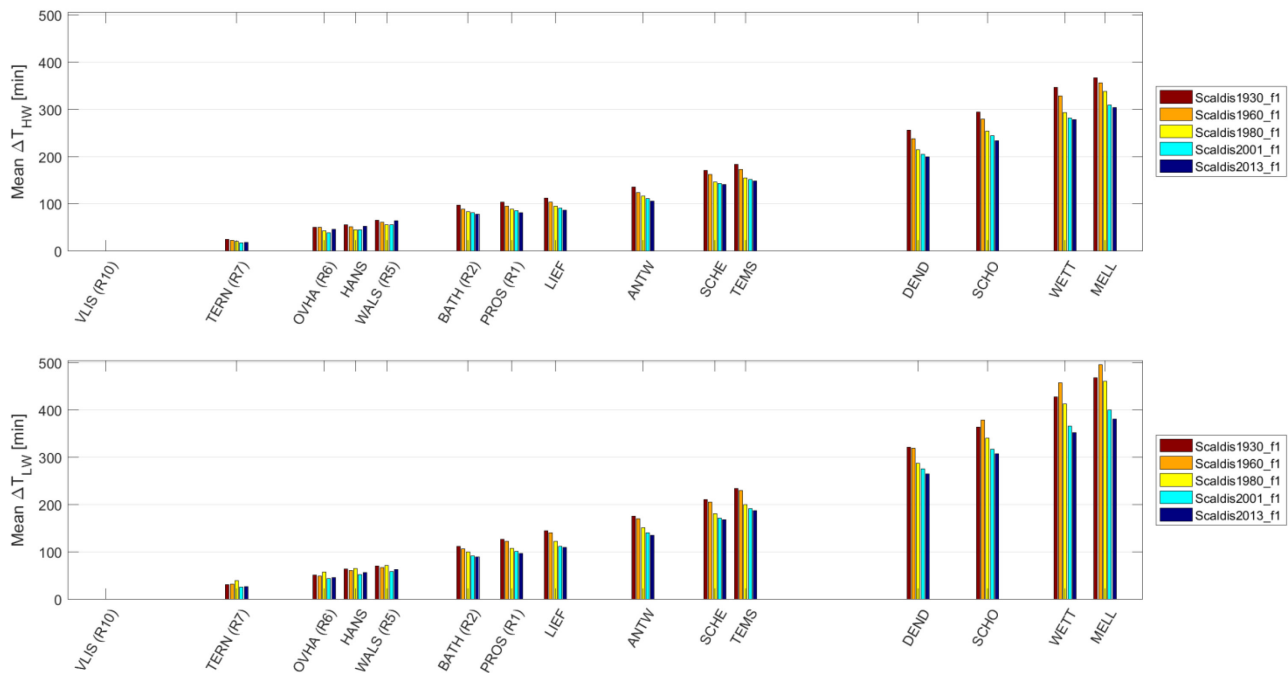


Figure 38 – Modelled historical development in mean tidal wave celerity for high tide (top) and low tide (bottom), based on the high- and low water time-differences between downstream and upstream neighboring stations.

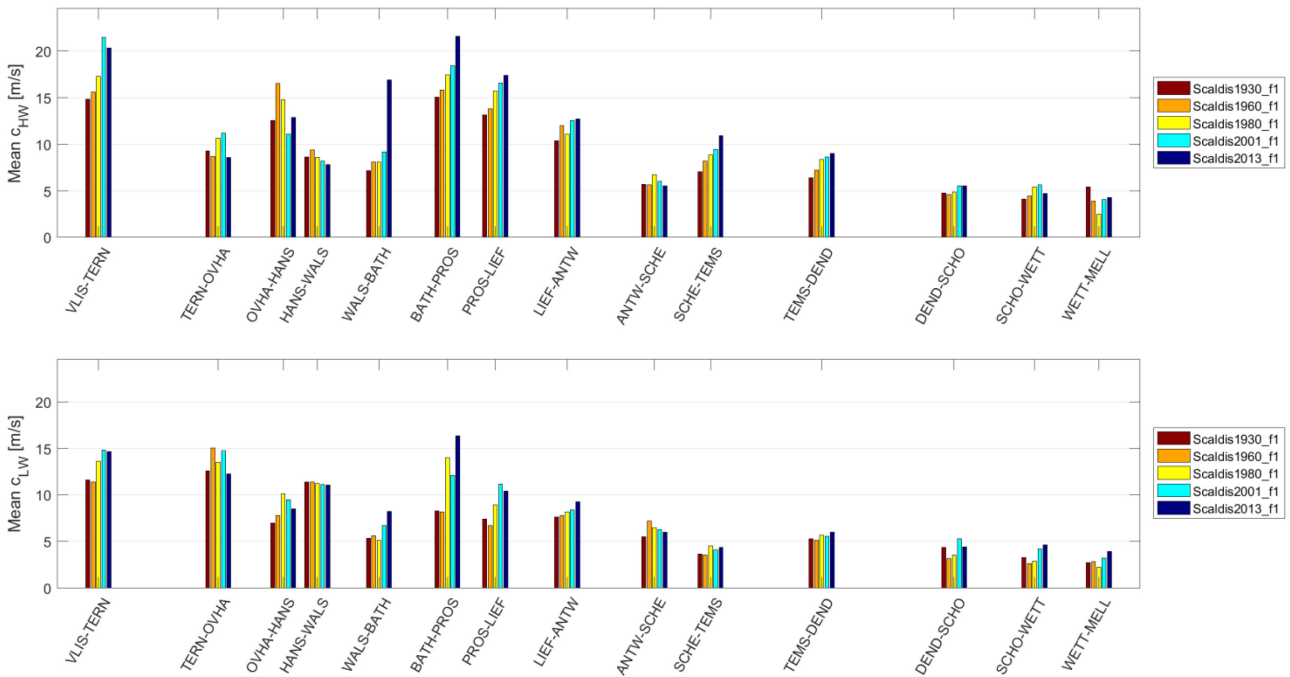
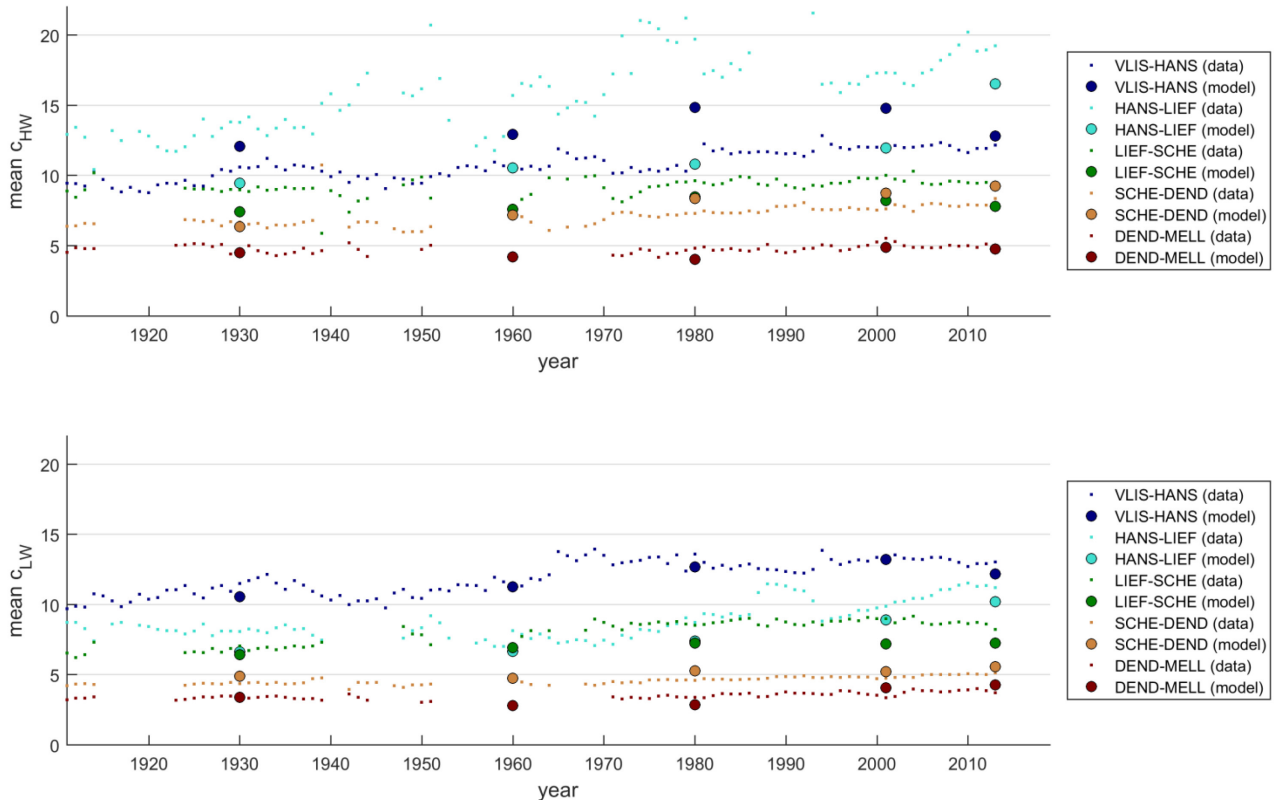


Figure 39 – Evolution of the observed historical development of the tidal wave celerity of high tide (top) and low tide (bottom) with the model results plotted along with them.



## 7.4 Tidal asymmetry

### Vertical tidal asymmetry

The modelled vertical tidal asymmetry at several locations along the estuary is depicted in Figure 40 by means of the ratio between the mean duration of the falling tide  $T_{fall}$  and the mean duration of the rising tide  $T_{rise}$ . Tidal asymmetry is flood-dominant if  $T_{fall}/T_{rise} > 1$  and ebb-dominant if  $T_{fall}/T_{rise} < 1$ . Furthermore, Figure 41 and Figure 42 give a comparison between the modelled and the observed vertical tidal asymmetry (i.e., based on historical high and low tide observations presented by Vandebrouwaene et al., 2019). The modelled mean vertical tidal asymmetry fits the observed values fairly well at most locations, although the modelled values tend to be slightly lower or less flood-dominant at Vlissingen. The same holds for the asymmetry at Antwerpen in 1960. Furthermore, tidal asymmetry is also underestimated for the 1930 model at Dendermonde, Schoonaarde and Wetteren in the Upper Sea Scheldt. At Schoonaarde, the underestimation of the flood-dominant asymmetry persists for all historical models.

In general, the mean vertical tidal asymmetry changes gradually from slightly flood-dominant in the Western Scheldt (i.e.,  $T_{fall}/T_{rise} = 1.05-1.12$ ) to a more distinct flood-dominant asymmetry in the Upper Sea Scheldt (i.e.,  $T_{fall}/T_{rise} = 1.50-2.30$ ). In accordance with observations, the modelled vertical tidal asymmetry in the Sea Scheldt becomes more flood-dominant between 1930 and 1960, along with a decrease in intertidal storage in the estuary. There is no clear development in vertical tidal asymmetry in the Western Scheldt between 1930 and 1960. From 1960 onwards, the flood-dominance in the entire estuary slowly decreases again to values that are lower than they initially were in 1930. Those trends are most pronounced upstream in the Upper Sea Scheldt. Remarkably, the development of the vertical tidal asymmetry in the Western Scheldt and Lower Sea Scheldt shifts again towards a slight increase in flood-dominance between 2001 and 2013.

### Horizontal tidal asymmetry

The modelled horizontal tidal asymmetry is depicted in Figure 40 as the ratio between the maximum cross-sectional averaged velocities during flood and ebb  $V_{FL-max}/V_{EB-max}$  averaged over two spring-neap cycles and by means of the normalized third order velocity moment  $\gamma_0 = \mu_3/\mu_2^{1.5}$ . The indicators for horizontal tidal asymmetry depict flood-dominance if  $V_{FL-max}/V_{EB-max} > 1$  or  $\gamma_0 > 0$ . Similarly, they indicate ebb-dominance if  $V_{FL-max}/V_{EB-max} < 1$  and  $\gamma_0 < 0$ .

While the mean vertical tidal asymmetry is without exception flood-dominant along the estuary, the mean horizontal tidal asymmetry shows more variation depending on the indicator used. Based on  $V_{FL-max}/V_{EB-max}$ , the horizontal tidal asymmetry is mainly flood-dominant throughout the estuary, although the horizontal asymmetry does not increase towards the upstream part of the estuary as the vertical tidal asymmetry does. However, the horizontal asymmetry based on the third-order velocity moment is mostly ebb-dominant (i.e.,  $\gamma_0 < 0$ ). The horizontal tidal asymmetry tends to be most flood-dominant (or least ebb-dominant) at Bath (i.e.,  $V_{FL-max}/V_{EB-max} = 1.19-1.35$ ;  $\gamma_0$  of -0.03 up to 0.06) and less flood-dominant (or more ebb-dominant) between Vlissingen and Terneuzen (i.e.,  $V_{FL-max}/V_{EB-max} = 1.08-1.16$ ;  $\gamma_0$  between -0.12 and -0.05) and in the Lower Sea Scheldt up until Antwerpen (i.e.,  $V_{FL-max}/V_{EB-max} = 1.03-1.21$ ;  $\gamma_0$  between -0.15 and -0.05 at Antwerpen). The spatial and temporal variation in horizontal asymmetry in the Upper Sea Scheldt are more variable. Nevertheless, the ebb-dominance of the third-order velocity moment is strongest at the most upstream locations in the Upper Sea Scheldt. This contradicts with the stronger flood-dominance of the vertical tidal asymmetry in the most upstream part of the estuary. Hence, different parameters for tidal asymmetry do not always indicate the same type or strength of tidal asymmetry.

Finally, the modelled development over time of the horizontal tidal asymmetry is similar to the modelled development of the vertical tidal asymmetry. In particular, horizontal tidal asymmetry generally becomes more flood-dominant (or less ebb-dominant) between 1930 and 1960. Later on, flood-dominance decreases again or ebb-dominance increases again up until 2001. Ultimately, this trend reverses again

between 2001 and 2013 as  $V_{FL-max}/V_{EB-max}$  becomes more flood-dominant and  $\gamma_0$  becomes less ebb-dominant. These historical developments in horizontal tidal asymmetry are most pronounced in the Sea Scheldt. Exceptions are the most upstream locations at Melle and Wetteren where the development in horizontal tidal asymmetry is more variable over time, possibly due to differences in upstream discharge between model simulations.

Figure 40 – Modelled historical development in mean tidal asymmetry based on the ratio between the duration of the falling and rising tide (top), based on the ratio between peak cross-sectional averaged flood and ebb velocities (mid) and based on the third-order velocity moment  $\gamma_0$  (bottom).

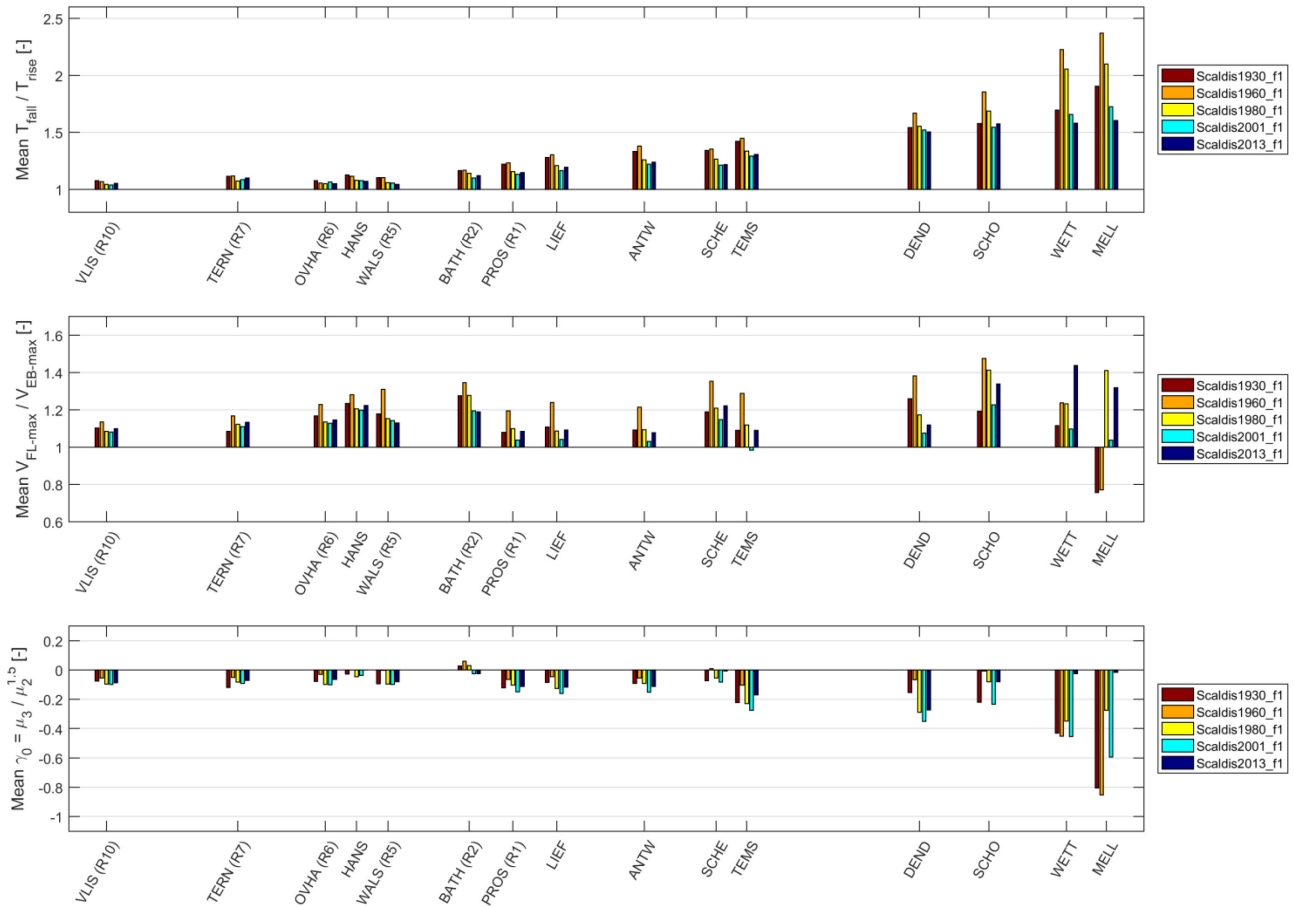


Figure 41 – Evolution of the observed historical development of the vertical tidal asymmetry based on the duration of the falling and rising tide in the Western Scheldt and Lower Sea Scheldt, with the model results plotted along with them.

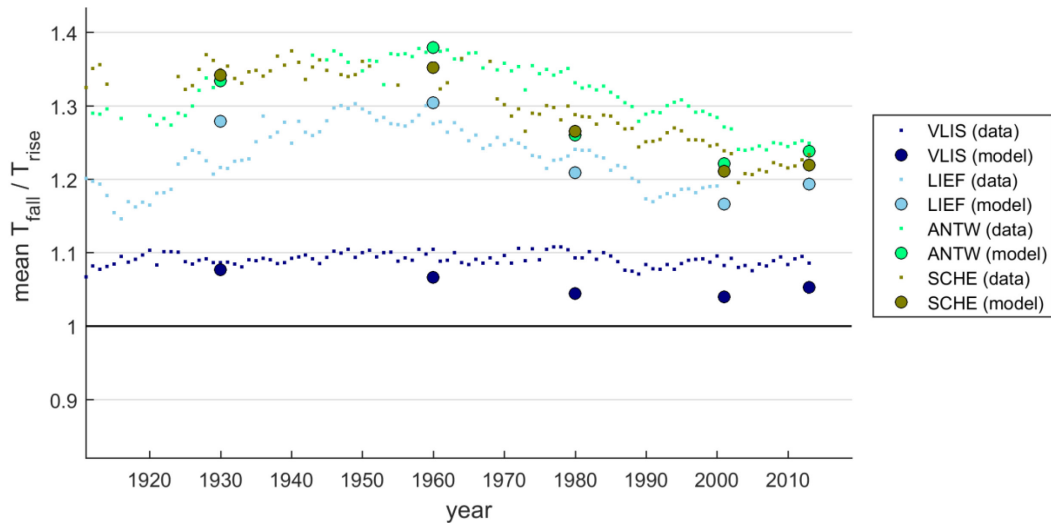
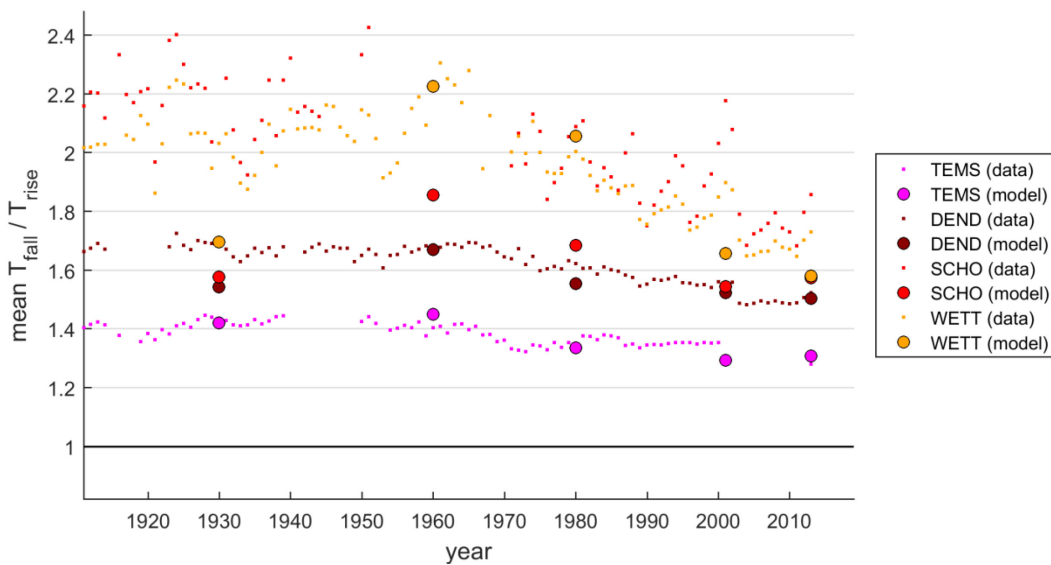


Figure 42 – Evolution of the observed historical development of the vertical tidal asymmetry based on the duration of the falling and rising tide in the Upper Sea Scheldt, with the model results plotted along with them.



## 8 Discussion and conclusions

### 8.1 Model performance

The simultaneous calibration of five historical models of the Scheldt Estuary (i.e., the 1930, 1960, 1980, 2001 and 2013 models) was presented in this report.

The model grid of the three-dimensional Scaldis 2013 model, developed in a previous study by Smolders et al. (2016), was adapted to implement historical tidal branches and intertidal areas. Offshore boundary conditions were generated by nesting the Scaldis model grid into the CSM- and ZUNO-models of the entire North Sea. Model calibration further consisted of the stepwise adjustment of bottom friction coefficients in three large friction zones (i.e., Western Scheldt, Lower Sea Scheldt and Upper Sea Scheldt). This was done simultaneously for the five historical models in order to obtain a friction field that gives the best overall model performance (i.e., averaged over the five historical models). Best overall results are obtained with a Manning friction coefficient of  $0.021 \text{ s}\cdot\text{m}^{-1/3}$  in the Western Scheldt (i.e., between Cadzand and Bath),  $0.017 \text{ s}\cdot\text{m}^{-1/3}$  in the Lower Sea Scheldt (i.e., between Bath and the Scheldt-Rupel confluence) and  $0.012 \text{ s}\cdot\text{m}^{-1/3}$  in the Upper Sea Scheldt (i.e., upstream of Temse).

Overall, the model validation shows that the five historical models perform well in the Western Scheldt and, except for the 1960 model, also in the Lower sea Scheldt. The accuracy of the historical models generally decreases in the upstream part of the Upper Sea Scheldt where tidal ranges are mostly underestimated. In particular, the most recent 2001 and 2013 models reproduce high- and low water levels with a mean error of  $\leq 0.15 \text{ m}$ , while high- and low water phases are represented with mean errors of less than 10 minutes (i.e. smaller than the model output time step) throughout the estuary. The historical 1930 model has a similar accuracy along the Western Scheldt and Lower Sea Scheldt, but its performance is less good in the most upstream part Upper Sea Scheldt where low water errors increase up to  $+0.35 \text{ m}$ . The 1960 model produces a large-scale overestimation of high-, low- and mean water levels in the Lower Sea Scheldt, while it also underestimates the tidal range by up to  $0.50 \text{ m}$  in the upstream part of the Upper Sea Scheldt. Finally, the 1980 model underestimates the tidal range throughout the estuary, indicating that its poor model performance possibly results from a bad representation of the offshore and mouth area or from the boundary conditions itself. Nevertheless, the underestimation of the tidal range remains more or less similar along large parts of the estuary up until Schelle, from where the model error increases.

#### Possibilities for model improvement

Sensitivity analyses indicated that tuning of the user-defined turbulent viscosity (i.e., implemented as velocity diffusivity coefficient) does not lead to further improvement of the model results in the Scaldis model. Other potential possibilities for improvement of the model performance in the Upper Sea Scheldt include but are not limited to: refining the bathymetrical representation of the shallow and intertidal zones (i.e., the representation of the river banks and edge between the subtidal and intertidal areas in the upstream part of the estuary appears to be quite rough in the older 1960 and 1930 bathymetries); improving the representation of the upstream discharge (i.e., using daily or even hourly averages); or using different numerical parameters, numerical schemes or solvers within the Telemac-3D modeling system. However, these adaptations are not tested in this report as the main goal of the developed historical models is to represent estuary scale changes in tidal hydrodynamics as a result of human-induced geometric and morphological changes, rather than focusing specifically on the most upstream stretches of the Upper Sea Scheldt.

## 8.2 Historical development of tidal characteristics

Five historical models were used to compute historical tidal characteristics along the estuary with a special focus on characteristics that could not be derived from the available high- and low water observations presented in Subreport 1 (Vandenbruwaene et al., 2019).

The historical development of the vertical tidal characteristics in the Scheldt Estuary was already assessed based on historical water level observations in Subreport 1 and Subreport 2 of this study (i.e., Vandenbruwaene et al., 2019; 2020) as well as in earlier studies (e.g. De Kramer, 2002; Kuijper, 2013; Vandenbruwaene, 2016). The present modelling study confirms previous conclusions on a continuous increase in tidal range over the analyzed period of over 80 years. The largest tidal range increase of 1.08 m or 1.3 cm/yr on average is modelled at Temse. In accordance with the observations, most of the modelled tidal range increase occurred between 1960 and 1980 along with the first enlargement of the navigation channels in the 1970s.

In addition, the model results indicate a continuous increase in tidal prism throughout the estuary together with the tidal range increase between 1960 and 2016. In contrast, the modelled tidal prism decreased between 1930 and 1960, which can be explained by the loss of intertidal storage areas and historical tidal branches that occurred during this period (e.g. Vandenbruwaene et al., 2020). Later on, channel enlargements are considered to have enhanced the propagation of the tidal wave, leading to an increase in tidal prism and tidal range throughout the estuary. The modelled tidal prisms in the Western Scheldt are of the same order as the tidal prisms that were calculated based on discharge measurements (see: De Kramer, 2002), although these observed tidal prisms were cumulated over both flood and ebb implying that the presented values are a factor 2 higher. Besides, the modelled tidal prisms correspond quantitatively well with tidal prisms that were calculated from water level and discharge measurements by Plancke et al. (2012) using the cubature method.

The modelled tidal velocities, assessed as mean and maximum cross-sectional averaged velocities during flood and ebb, have a similar along-estuary variation in all historical models. In the Western Scheldt, they increase from the estuary mouth towards Hansweert, while velocities are clearly lower between Walsoorden and Prosperpolder where the adjacent intertidal storage volume is largest. Further upstream, velocities increase again towards Schelle where the highest tidal velocities are generally found. Finally, the lowest tidal velocities are modelled in the Upper Sea Scheldt for all historical models. This along-estuary pattern corresponds fairly well with the findings of Vandenbruwaene et al. (2013), whom used the cubature method to compute cross-sectional averaged velocities during flood and ebb for the 1960 and 2001 situation. The development over time of the tidal velocities along the estuary is more variable, except for the Upper Sea Scheldt where the highest velocities are clearly found in the more recent models. However, in contrast to findings of Vandenbruwaene et al. (2013) that velocities in the Upper Sea Scheldt were higher in 1960 than in 2001, the present model results indicate a continuous increase in cross-sectional averaged velocities from 1960 onwards. In this context, it should be mentioned that the model performance of especially the 1960 model is quite poor in the Upper Sea Scheldt (i.e., significant underestimation of the tidal range).

### Celerity

The celerity of the tidal wave (based on high and low water propagation) was assessed on a more detailed spatial scale in this model analysis than in the data analyses by Vandenbruwaene et al. (2019). The low water celerity is generally well-represented by the different models. Nevertheless, the models tend to overestimate the high water celerity between Vlissingen and Hansweert and underestimate the high water celerity between Hansweert and Liefkenshoek. Both the present model results and the data analysis by Vandenbruwaene et al. (2019) indicate that the high water celerity increased more over time than the low water celerity. Historical embankments are a probable cause for an increase in high water celerity, while historical channel enlargements probably induced the increase in low water celerity. In this context,

Friedrichs & Madsen (1992) showed analytically that when tidal variations in channel depth dominate tidal variations in channel width (i.e., relatively shallow channels and little intertidal storage), high water celerity is faster than low water celerity and the tide tends to be shorter-rising. Similarly, when tidal variations in channel width dominate tidal variations in channel depth (i.e., ample intertidal storage and relatively deep channels), low water celerity tends to be faster high water celerity causing a shorter-falling tide. Similar conclusions were also drawn by Fortunato & Oliveira (2005), who assessed high- and low water celerity in the presence of tidal flats with different elevations and concluded that tidal flats reduce high water celerity the most if they are situated at or slightly above mean water level. Their findings were confirmed numerically with a TELEMAC-2D model by Stark et al. (2017). Regarding the historical developments in tidal wave celerity that were observed and modelled in this study, it can be concluded that when the high water celerity increased more than the low water celerity, the loss in intertidal storage was more important than channel deepening. Similarly, during periods in which the low water celerity increased more than the high water celerity, the increase in channel depth was more important than the loss in intertidal storage volume. Besides, a remarkable increase in high water celerity is modelled for the estuary section between Walsoorden and Bath between 2001 and 2013, potentially induced by a local loss of intertidal storage volume in this section (i.e., large parts of the Platen van Valkenisse and Plaat van Walsoorden experienced an elevation increase during this period). However, the present results underestimate the high water celerity between Hansweert and Liefkenshoek for the 1930-2001 models, while the calculated tidal wave celerity over such a short transect may well be affected by the output time step of the model which is of the same order as the high- or low water phase differences between some of the subsequent tidal stations.

### Asymmetry

The ratio between the duration of the falling and rising tide, the ratio between maximum flood and ebb velocities and the normalized third order velocity moment were extracted from the model results as indicators for tidal asymmetry. All three indicators for tidal asymmetry show similar historical trends. In particular, tidal asymmetry became more flood-dominant between 1930 and 1960. In accordance with analytical results of e.g. Friedrichs & Madsen (1992), Friedrichs & Aubrey (1994) or Fortunato & Oliveira (2005), who showed that the presence of tidal flats enhances ebb-dominance, this increase in flood-dominance between 1930 and 1960 can be attributed to the loss in intertidal storage areas. Between 1960 and 2001, when the human-induced morphological impacts mainly consisted of stepwise channel enlargement and other sand mining or dredging activities, the observed and modelled tidal asymmetry became less flood-dominant (or more ebb-dominant) again. Following the above-mentioned analytical studies on tidal propagation through estuaries and channels (i.e., Friedrichs & Madsen, 1992; Friedrichs & Aubrey, 1994), channel deepening enhances the low water propagation more than the high water propagation, which reduces the flood-dominance. Most recently, between 2001 and 2013, model results show that the temporal development in tidal asymmetry shifted back to an increase in flood dominance (or decrease in ebb-dominance). A similar trend is present in the data analysis in Subreport 1 (Vandenbruwaene et al., 2019), in which the asymmetry slightly drops in 2001 and slowly increases from 2001 onwards. It should be stated this apparent increase in flood-dominance is rather small and is only based on one decade of observations, implying that the potential influence of the 18.6-year nodal cycle of the tide cannot be neglected on this timescale.

While the indicators for tidal asymmetry generally result in similar trends over time, they do differ quantitatively. Vertical tidal asymmetry based on the duration of the falling and rising tide, as well as horizontal tidal asymmetry based on the peak flood and ebb velocities, both indicate a flood-dominant asymmetry throughout the estuary for all simulations, whereas the normalized third-order velocity moment indicates an ebb-dominant asymmetry at most parts of the estuary. The latter corresponds with model results of Stark et al. (2017), who used the same indicators to assess the effect of intertidal area changes on tidal hydrodynamics in the Scheldt Estuary with a TELEMAC-2D model. The fact that different characterizations of horizontal tidal asymmetry result in opposite types of asymmetry could imply opposite residual transport directions for different sediment types (e.g. cohesive vs. non-cohesive transport). In

particular, the residual load of sediments of which the transport is mostly influenced by peak velocities would be in flood-direction, whereas residual transport that is influenced by lower velocities as well could be in ebb-direction, based on the present model results. However, numerical modeling of historical (cohesive or non-cohesive) sediment transport goes beyond the scope of this study.

### 8.3 Outlook

Ultimately, it is intended that the historical models are used to assess the hydrodynamic impact of specific large-scale morphological changes in the estuary. Therefore, scenario analyses can be performed to assess the effect of individual or combined effects of embankments, de-embankments, channel enlargements or other morphological changes resulting from anthropogenic impacts. For example, historical bathymetries can be combined to isolate the effects of morphological changes in the estuarine channels (i.e., channel deepening) or in the intertidal areas (i.e., storage area loss and marsh elevation increase). Additionally, model scenarios could be performed in which the historical models are run for varying boundary conditions to study whether the obtained developments in tidal characteristics result from changes in morphology or if long-term variations in hydraulic boundary conditions (e.g., sea level rise) also play a role.

The results of a model scenario analysis are presented in Subreport 4 of this study (Stark et al., 2020).

Besides, the present model results could potentially be used in harmonic component analyses to assess the relative contribution of tidal constituents along the estuary, which provides for additional indicators for the strength and type of tidal asymmetry (e.g. Wang et al., 1999, 2002).

Another opportunity is using the historical models that were developed for this study to simulate (cohesive and/or non-cohesive) sediment transport or morphological developments. By doing so, the historical development of sediment transport patterns in the estuary could be assessed or the impact of future impacts to the morphology and geometry of the estuary on sediment transport patterns can be investigated.

## 9 References

**Claessens, J.; Belmans, H.** (1984). Overzicht van de tijwaarnemingen in het Zeescheldebekken gedurende het decennium 1971-1980. *Tijds. Openb. Werken Belg. = Ann. Trav. Publics Belg.* 1984(3): [1-96].

**Codde, R.; De Keyser, L.N.** (1963). Overzicht van de tijwaarnemingen in het Zeescheldebekken gedurende het tijdperk 1951-1960. *Tijds. Openb. Werken Belg. = Ann. Trav. Publics Belg.* 116(4): [1-68].

**Coen, L.; Peeters, P.; Mostaert, F.,** 2008. Inventarisatie en historische analyse Zeeschelde habitats: Effect antropogene ingrepen en natuurlijke evoluties op de getij-indringing in de Zeeschelde - Ondersteunende numerieke 1D-modellering. WL Rapporten, 713\_21 Waterbouwkundig Laboratorium: Antwerpen, België.

**Cox, T.; Maris, T.; De Vleeschauwer, P.; De Mulder, T.; Soetaert, K.; Meire, P.** (2006). Flood control areas as an opportunity to restore estuarine habitat. *Ecol. Eng.* 28, 55-63. doi:10.1016/j.ecoleng.2006.04.001.

**De Kramer, J.** (2002). Waterbeweging in de Westerschelde: een literatuurstudie. ICG-rapport: 02/6. ISBN 90-77079-08-4.

**Dujardin, A.; Meire, D.; Chu, K.; Vanlede, J.; Plancke, Y.; Mostaert, F.** (2017). Slibbalans Zeeschelde: sub report 8 – Hydrodynamic model 1954. Versie 4.0. FHR reports, 00\_029\_8. Flanders Hydraulics Research: Antwerp . XI, 73 + 86 p. appendices pp.

**EDF-R&D,** (2013). 3D hydrodynamics TELEMAC-3D software. Release 6.2. Operating Manual

**Fortunato, A.B.; Oliveira, A.** (2005). Influence of intertidal flats on tidal asymmetry. *J. Coast. Res.* 21, 1062e1067. doi:10.2112/03-0089.1.

**Friedrichs, C.T.; Aubrey, D.G.** (1994). Tidal propagation in strongly convergent channels. *J. Geophys. Res.* 99, 3321-3336. doi:10.1029/93JC03219.

**Friedrichs, C.T.; Madsen, O.S.** (1992). Nonlinear diffusion of the tidal signal in frictionally dominated embayments. *J. Geophys. Res.* 97, 5637-5650. doi:10.1029/92JC00354.

**Hervouet, J.-M.** (2007). Hydrodynamics of Free Surface Flows: Modelling with the finite element method. doi:10.1002/9780470319628

**Jeuken, C.; Wang, Z.B.; van der Kaaij, T.; Van Helvert, M.; Van Ormondt, M.; Bruinsma, R.; Tanczos, I.** (2004). Morfologische ontwikkelingen in het Schelde estuarium bij voortzetting van het huidige beleid en effecten van een verdere verdieping van de vaargeul en uitpoldering langs de Westerschelde. Deelovereenkomst 2 en 3. Morfologie. Arcadis/Technum/WL | Delft Hydraulics: Delft. 228 pp.

**Jeuken, C.J.L.; Hordijk, D.; Ides, S.; Kuijper, C.; Peeters, P.; de Sonnevile, B.; Vanlede, J.** (2007). Koploperproject LTV-O&M - Thema Veiligheid: deelproject 1. Inventarisatie historische ontwikkeling van de hoogwaterstanden in het Schelde-estuarium. Delft Hydraulics/Waterbouwkundig Laboratorium: Delft. 92 pp.

**Kuijper, K.** (2013). Aanvullend onderzoek historische ontwikkeling getij in het Scheldeestuarium. Data-analyse en toepassingen analytisch model. IMDC NV/Deltares/Svasek Hydraulics/ARCADIS Nederland: Antwerpen. 109 pp.

**Kuijper, K.; Lescinski, J.** (2012). LTV O&M thema Veiligheid - Sub project 1: data analyses and hypotheses Western Scheldt. Deltares: [s.l.]. 126 + bijlagen pp.

**Leyssen, G.; Vanlede, J.; Decrop, B; Van Holland, G; Mostaert, F.** (2012). Modellentrein CSM-ZUNO. Deelrapport 2: Validatie. WL Rapporten, 753\_12. Waterbouwkundig Laboratorium & IMDC: Antwerpen, België.

- Maris, T.; Cox, T.; Temmerman, S.; De Vleeschouwer, P.; Van Damme, S.; De Mulder, T.; Van Den Bergh, E.; Meire, P.** (2007). Tuning the tide: creating ecological conditions for tidal marsh development in a flood control area. *Hydrobiologia* 588, 31-43. doi:10.1007/s10750-007-0650-5.
- Maximova, T.; Ides, S.; Vanlede, J.; De Mulder, T.; Mostaert, F.** (2009). Verbetering 2D randvoorwaarden model. Deelrapport 3: Kalibratie bovenlopen. WL Rapporten, 753\_09. Flanders Hydraulics Research: Antwerp, Belgium.
- Maximova, T.; Ides, S.; Plancke, Y.; De Mulder, T.; Mostaert, F.** (2010.) Vervolgstudie inventarisatie en historische analyse van slikken en schorren langs de Zeeschelde - Scenario analyse 2D model. WL Rapporten, 713\_21. Waterbouwkundig Laboratorium: Antwerpen.
- Maximova, T.; Vanlede, J.; Verwaest, T.; Mostaert, F.** (2016). Vervolgonderzoek bevaarbaarheid Bovenzeeschelde: Subreport 4 – Modelling Train CSM – ZUNO: validation 2013. Version 3.0. WL Rapporten, 13\_131. Flanders Hydraulics Research: Antwerp, Belgium.
- Nidzieko, N.J.; Ralston, D.K.**, (2012). Tidal asymmetry and velocity skew over tidal flats and shallow channels within a macrotidal river delta. *J. Geophys. Res. Ocean.* 117, 1e17. doi:10.1029/2011JC007384.
- Plancke, Y.; Schramkowski, G.; Verwaest, T.; Mostaert, F.** (2014). Kubatuuurberekening voor het Scheldeestuarium: Karakteristieke getijden uit het decennium 1991 - 2000 en topo-bathymetrische gegevens uit 2001. Versie 3.0. WL Rapporten, 00\_157. Waterbouwkundig Laboratorium : Antwerpen, België.
- Smolders, S.; Maximova, T.; Vanlede, J.; Plancke, Y.; Verwaest, T.; Mostaert, F.** (2016). Integraal Plan Bovenzeeschelde: Subreport 1 – SCALDIS: a 3D Hydrodynamic Model for the Scheldt Estuary. Version 5.0. WL Rapporten, 13\_131. Flanders Hydraulics Research: Antwerp, Belgium.
- Stark, J.; Smolders, S.; Meire, P.; Temmerman, S.** (2017). Impact of intertidal area characteristics on estuarine tidal hydrodynamics: A modelling study for the Scheldt Estuary. *Estuarine, Coastal and Shelf Science*, 198PA: 138-155. doi:10.1016/j.ecss.2017.09.004
- Stark, J.; Vandenbruwaene, W.; Mostaert, F.** (2020). Agenda for the Future – Historical evolution of tides and morphology in the Scheldt Estuary: Sub report 4 – Hydrodynamic modelling of morphological scenarios. Version 1.0. FHR Reports, 14\_147\_4. Flanders Hydraulics Research: Antwerp.
- Taverniers, E.; Mostaert, F.** (2009). Overzicht van de tijwaarnemingen in het Zeescheldebekken gedurende het decennium 1991-2000: T.O. tijwaarnemingen Zeescheldebekken 1991-2000. Versie 2.0, heruitg. papieren versie. WL Rapporten, 833\_01. Waterbouwkundig Laboratorium: Antwerpen. I, 170 pp.
- Van Braeckel, A.; Coen, L.; Peeters, P.; Plancke, Y.; Mikkelsen, J.; Van den Bergh, E.** (2012). Historische evolutie van Zeescheldehabitats. Kwantitatieve en kwalitatieve analyse van invloedsfactoren. Rapporten van het Instituut voor Natuur- en Bosonderzoek 2012 (59). Instituut voor Natuur- en Bosonderzoek, Brussel i.s.m. het Waterbouwkundig Laboratorium, Antwerpen.
- Vandenbruwaene, W.; Plancke, Y.; Verwaest, T.; Mostaert, F.** (2013). The long-term hydrogeomorphological evolution of the Schelde estuary: A comparison between 1951-1960 and 2000-2010. Version 2\_0. WL Rapporten, 00\_158. Flanders Hydraulics Research: Antwerp, Belgium.
- Vandenbruwaene, W.; Meire, D.; Vanlede, J.; Plancke, Y.; Vanlierde, E.; Verwaest, T.; Mostaert, F.** (2016). Integraal Plan Boven-Zeeschelde: Deelrapport 2 – Getijrapport Boven-Zeeschelde, Rupel en Durme. Versie 6.0.
- Vandenbruwaene, W.; Pauwaert, Z.; Meire, D.; Plancke, Y.; Deschamps, M.; Mostaert, F.** (2019). Agenda voor de Toekomst – Historische evolutie getij en morfologie Schelde estuarium : Evolutie van het getij over de periode 1888-2013. Versie 5.0. WL Rapporten, 14\_147. Waterbouwkundig Laboratorium: Antwerpen, België.

**Vandenbruwaene, W.; Beullens, J.; Meire, D.; Plancke, Y.; Mostaert, F.** (2020). Agenda voor de Toekomst – Historische evolutie getij en morfologie Schelde estuarium: Analyse morfologie en getij – data analyse. Versie 2.4. WL Rapporten, 14\_147. Waterbouwkundig Laboratorium: Antwerpen, België. WL Rapporten, 13\_131. Waterbouwkundig Laboratorium: Antwerpen, België.

**Vanlinderde, E.; Michielsen, S.; Vereycken, K.; Hertoghs, R.; Meire, D.; Deschamps, M.; Verwaest, T.; Mostaert, F.** (2016). Tienjarig overzicht van de tijwaarnemingen in het Zeescheldebekken: decennium 2001-2010. Versie 5.0. WL Rapporten, 12\_071. Waterbouwkundig Laboratorium: Antwerpen. XIV, 212 pp.

**Vekemans, R.** (1946). Tienjarig overzicht 1931-1940 der tijwaarnemingen in het Zeescheldebekken. Tijds. Openb. Werken Belg. = Ann. Trav. Publics Belg. augustus: [1-62] + 12 plates.

**Wang, Z. B.; Jeuken, C.; De Vriend, H. J.** (1999). Tidal asymmetry and residual sediment transport in estuaries: a literature study and application to the Western Scheldt. Z2749. WL | Delft Hydraulics: Delft, Nederland.

**Wang, Z.B.; Jeuken, C.; Gerritsen, H.; De Vriend, H.J.; Kornman, B.A.** (2002). Morphology and asymmetry of the vertical tide in the Westerschelde estuary. Cont. Shelf Res. 22, 2599-2609. doi:10.1016/S0278-4343(02)00134-6.



## 10 Appendices

### Overview of Appendices:

- Appendix 10.1 Grid Adaptation
- Appendix 10.2 Sensitivity analysis: grid adaptation
- Appendix 10.3 Sensitivity analysis: effect of discharge at Bath
- Appendix 10.4 Initial model performance with the Scaldis2013 bottom friction field
- Appendix 10.5 Evaluation of peak discharges in simulation period
- Appendix 10.6 Results of calibration runs: RMSE of HW, LW,  $T_{HW}$  and  $T_{LW}$
- Appendix 10.7 Sensitivity analysis: viscosity coefficient

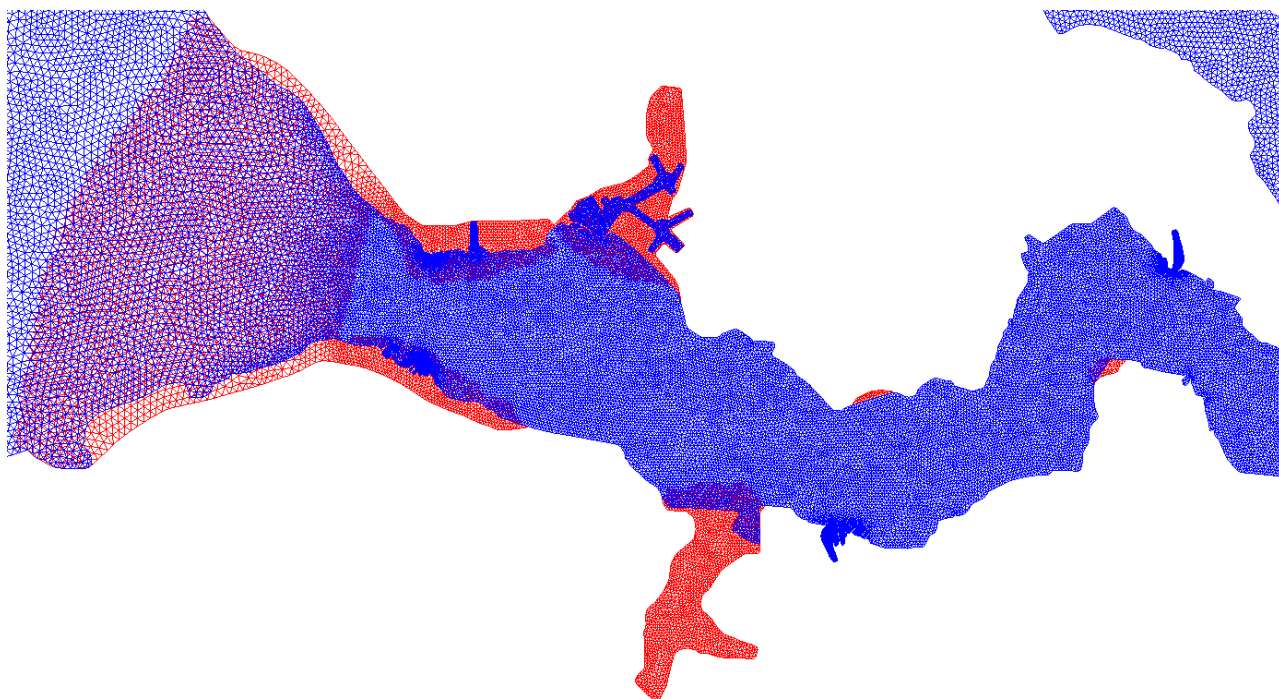
## 10.1 Grid adaptation

A comparison of the original Scaldis and adapted grid is presented in Figure 43 to Figure 46. Figure 47 and Figure 50 show examples of the grid adaptation in the areas where the model bathymetry from different years is very different. The grid in these locations was extended and refined based on bathymetric samples (Figure 48, Figure 49, Figure 51 and Figure 52).

---

Figure 43 – Model grid for the downstream part of the Western Scheldt (blue: original Scaldis model; red: adapted grid)

---



---

Figure 44 – Model grid for the upstream part of the Western Scheldt and Lower Sea Scheldt (blue: original Scaldis model; red: adapted grid)

---

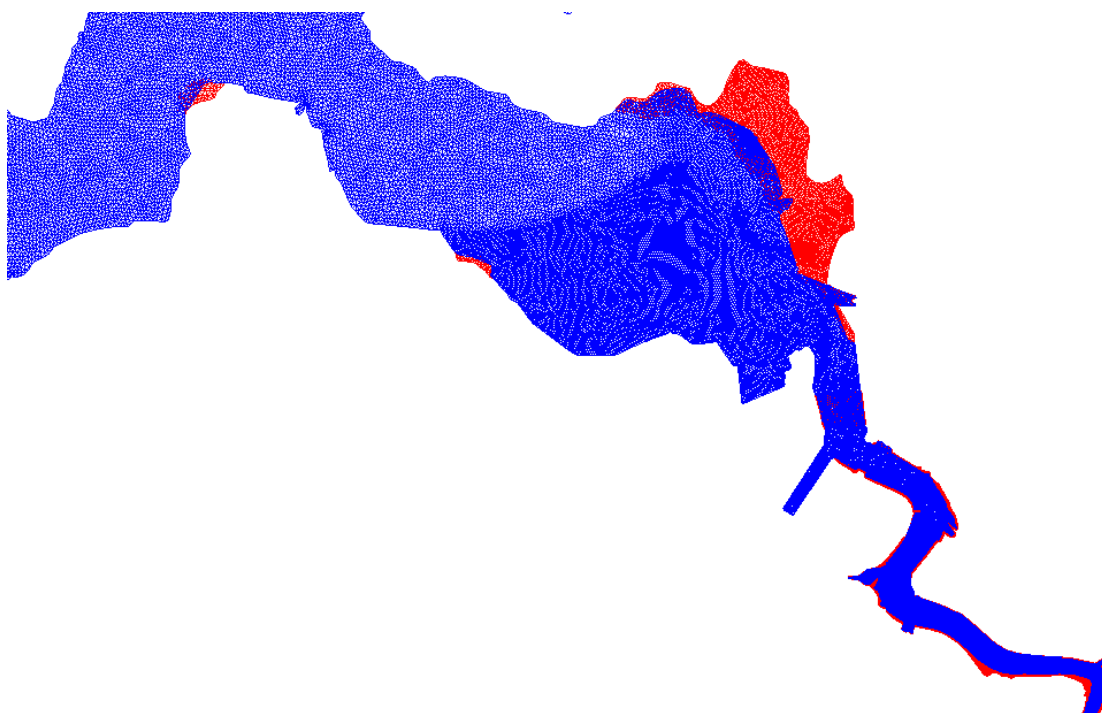


Figure 45 – Model grid for the Sea Scheldt, Durme and Rupel (blue: original Scaldis model; red: adapted grid)

---

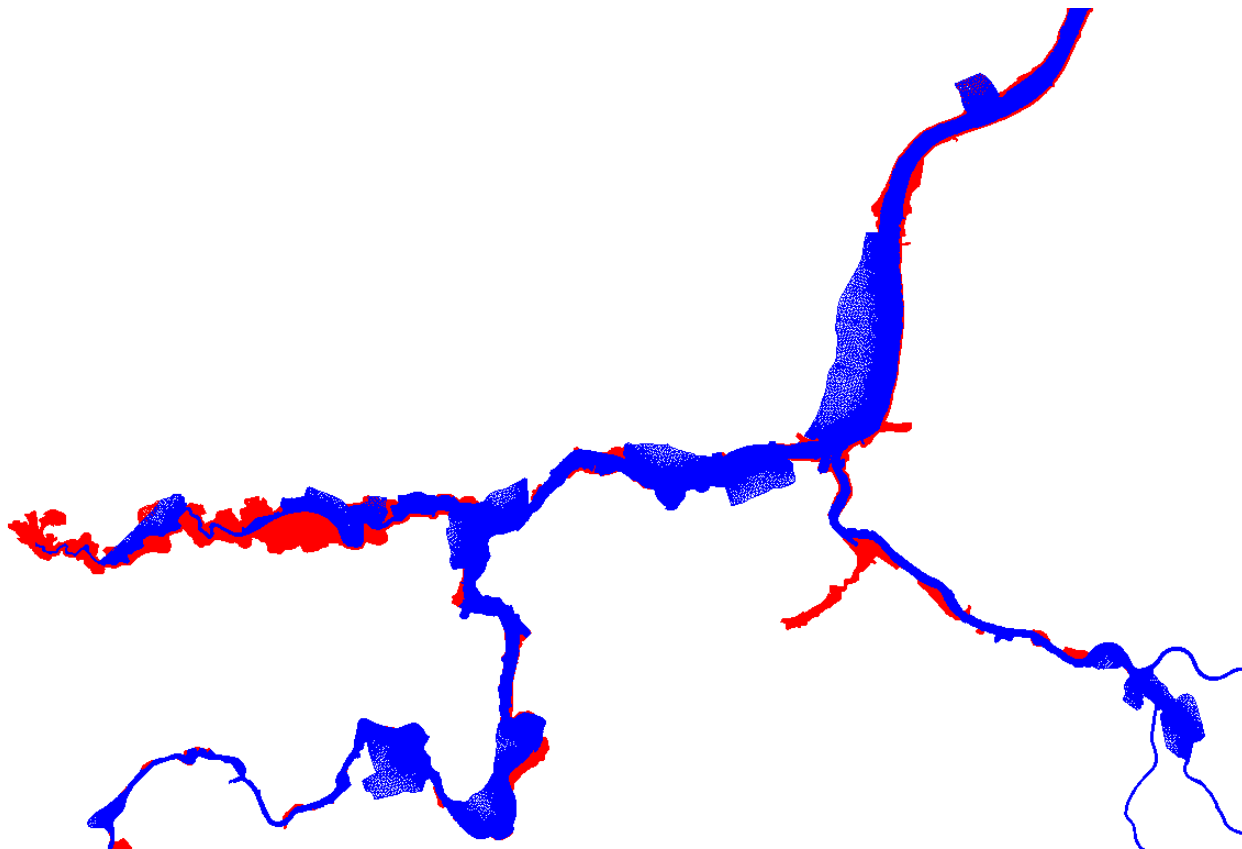


Figure 46 – Model grid for the Upper Sea Scheldt (blue: original Scaldis model; red: adapted grid)

---

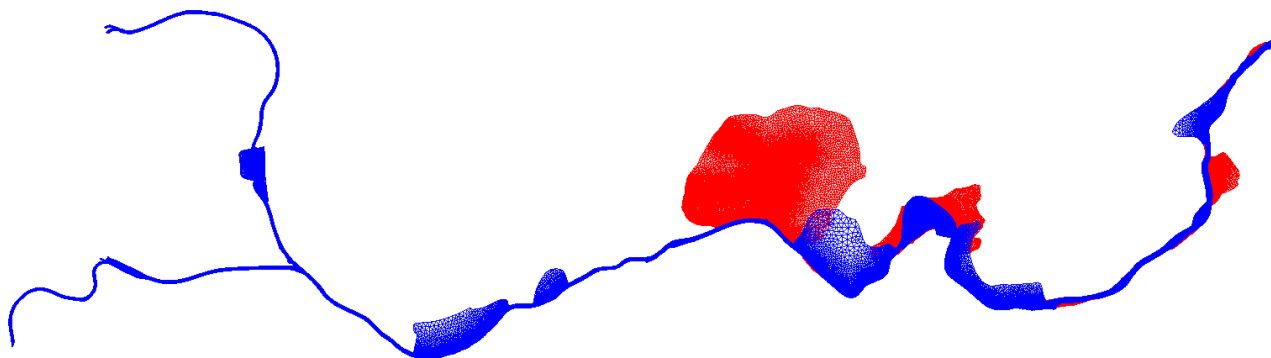


Figure 47 – Model grid for the Durme (blue: original Scaldis model; red: adapted grid)

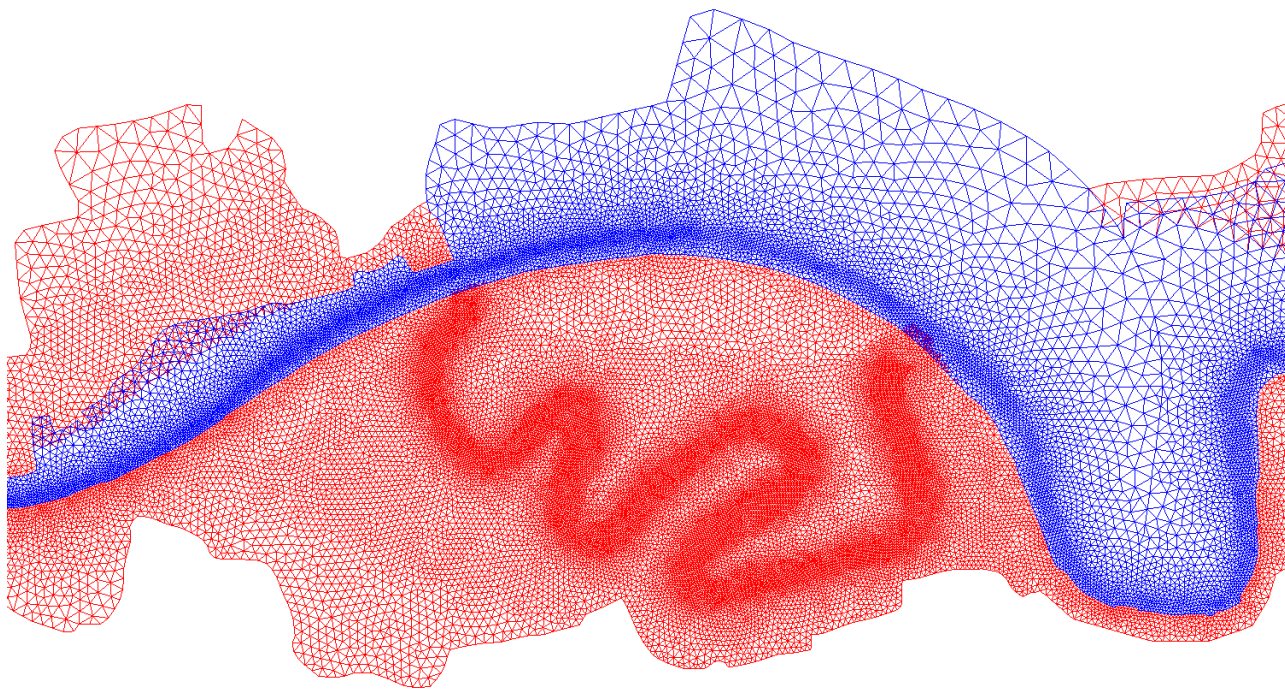


Figure 48 – Bathymetry of the Durme in 1930



Figure 49 – Bathymetry of the Durme in 1960

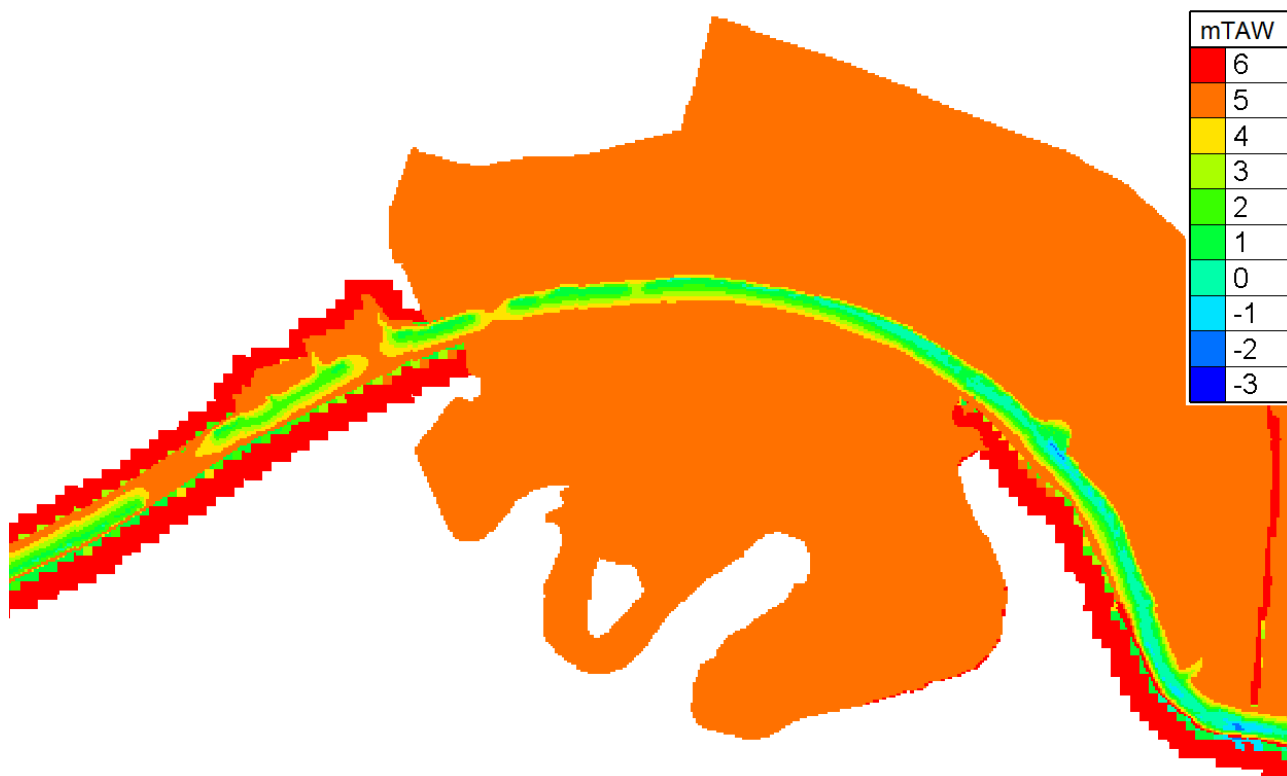


Figure 50 – Model grid for the Rupel (upstream Wintam) (blue: original Scaldis model; red: adapted grid)

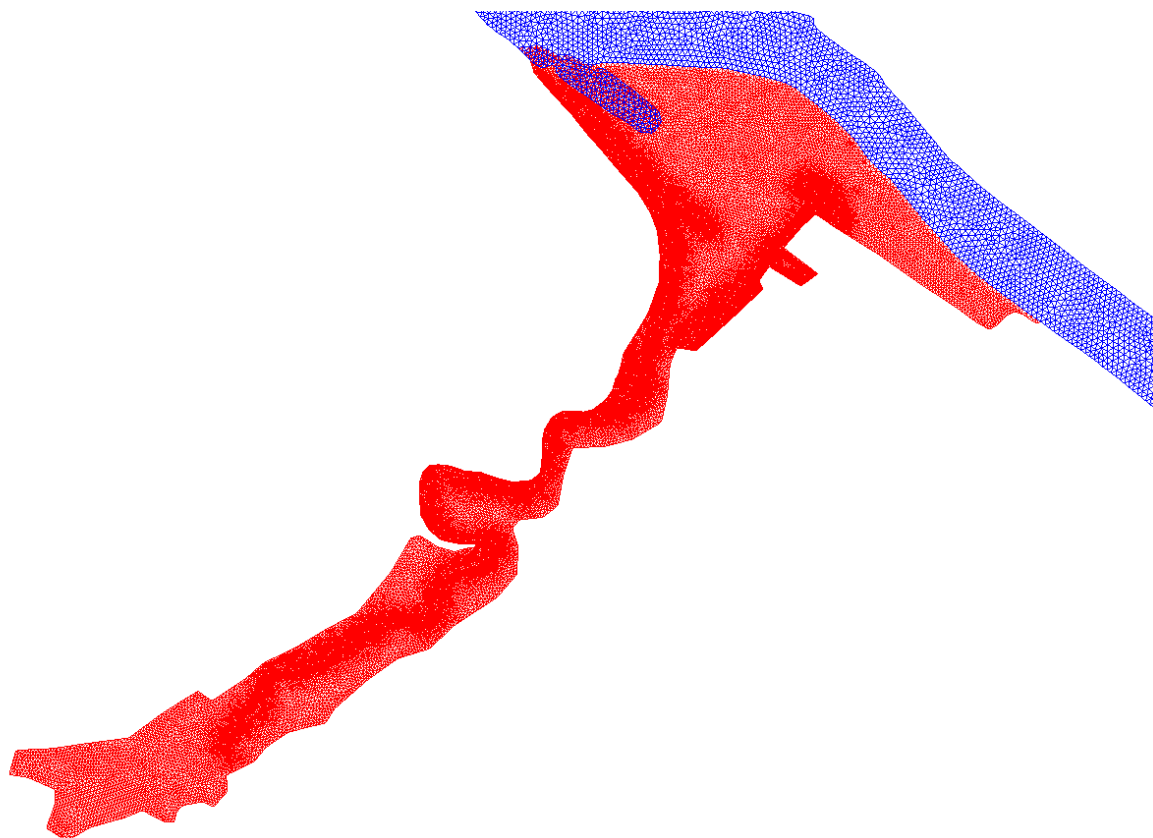


Figure 51 – Bathymetry of the Rupel upstream Wintam in 1930

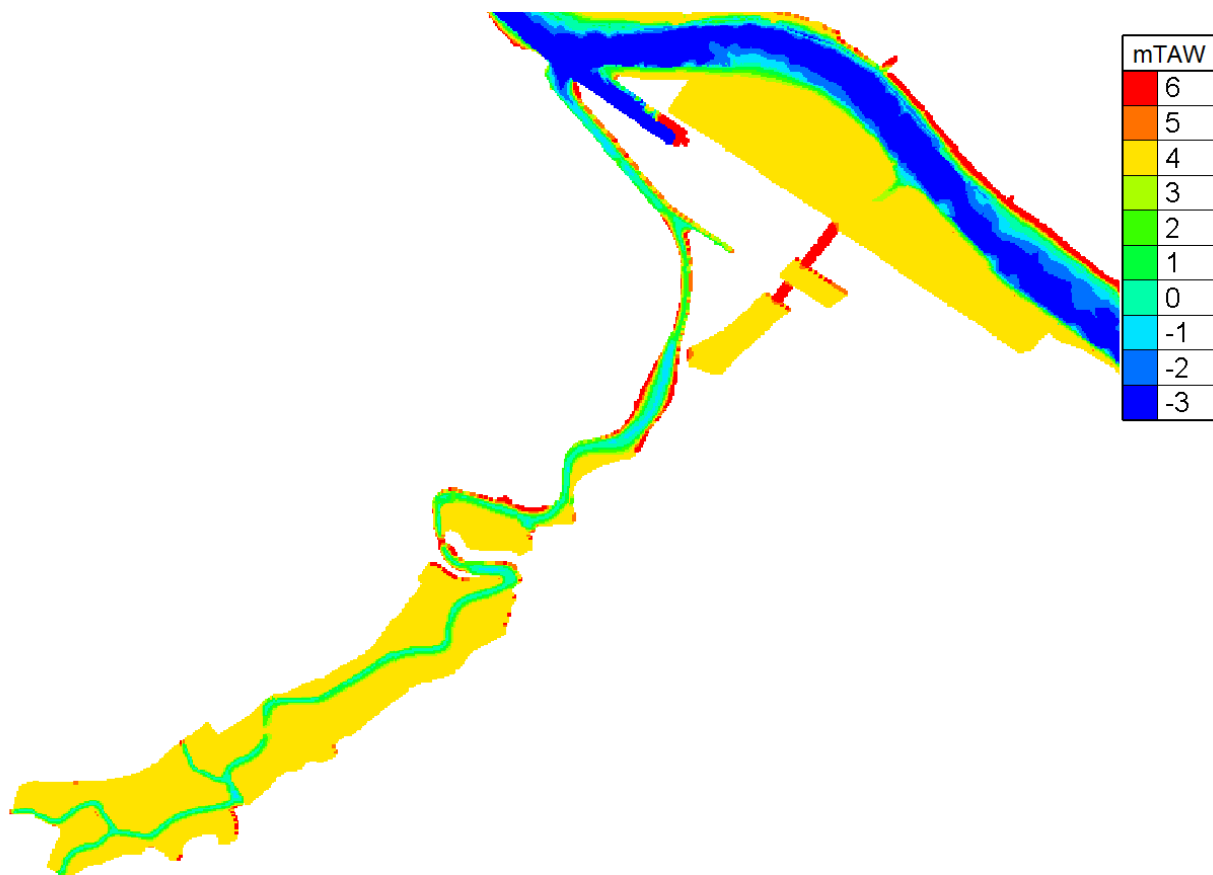
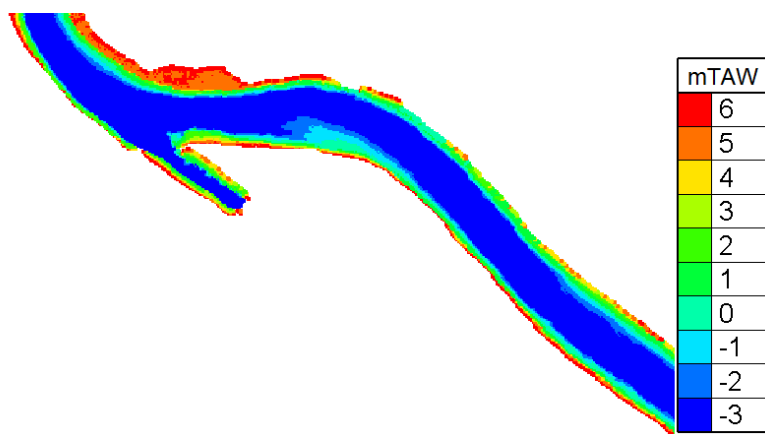


Figure 52 – Bathymetry of the Rupel upstream Wintam in 2001



## 10.2 Sensitivity Analysis: grid adaptation

A comparison between a model simulation with the original Scaldis2013 grid (r2d\_v20\_2013 in figures) and the adapted grid for this project (newgrid in figures) is presented below. The parameter settings, roughness field and topo-bathymetric input data are identical for both simulations. In particular, all parameter settings are obtained from the calibrated Scaldis 2013 model. Figure 53 – Figure 55 depict the impact of altering the mesh on the full water level time series along the estuary, high water levels along the estuary and low water levels along the estuary and offshore along the Belgian coast. The comparison shows that using the adapted model grid induces water level variations between -0.01 m and +0.01 m at tidal stations along the estuary. Figure 53 depicts that water levels are generally increased in the Lower Sea Scheldt (i.e., between Liefkenshoek and Temse), while water levels decrease in the proximity of the estuary mouth (i.e., at Cadzand and Westkapelle). The effect on high water levels and low water levels specifically is slightly stronger. If the adapted grid is used, high water levels increase by up to 0.005 m along the Western Scheldt and the downstream part of the Sea Scheldt (i.e., between Vlissingen and Kallo), while high water levels are decreased by 0.02 m further upstream. Besides, high water levels decrease by 0.015 m near the estuary mouth (i.e., at Cadzand and Westkapelle) if the adapted grid is used. The effect on low water levels along the estuary is more or less opposite of the effect on high water levels. In particular, low water levels at Westkapelle increase on average by almost 0.025 m if the adapted grid is used. In the Western Scheldt and downstream part of the Sea Scheldt, low water levels are decreased by up to 0.005 m, upstream of which low water levels are increased by up to 0.025 m if the adapted grid is used. The effects of the grid adaptations on both high water levels and low water levels in the coastal zone is limited.

In conclusion, the impact of the grid adaptation on the model performance is small as average water level differences are all within one or two centimeters. The newly adapted grid can thus be considered equally good as the previously calibrated and validated Scaldis2013 model by Smolders et al. (2016).

Figure 53 – Average water level difference along the estuary between a model simulation with the newly adapted grid (newgrid) and the original grid (r2d\_v20\_2013).

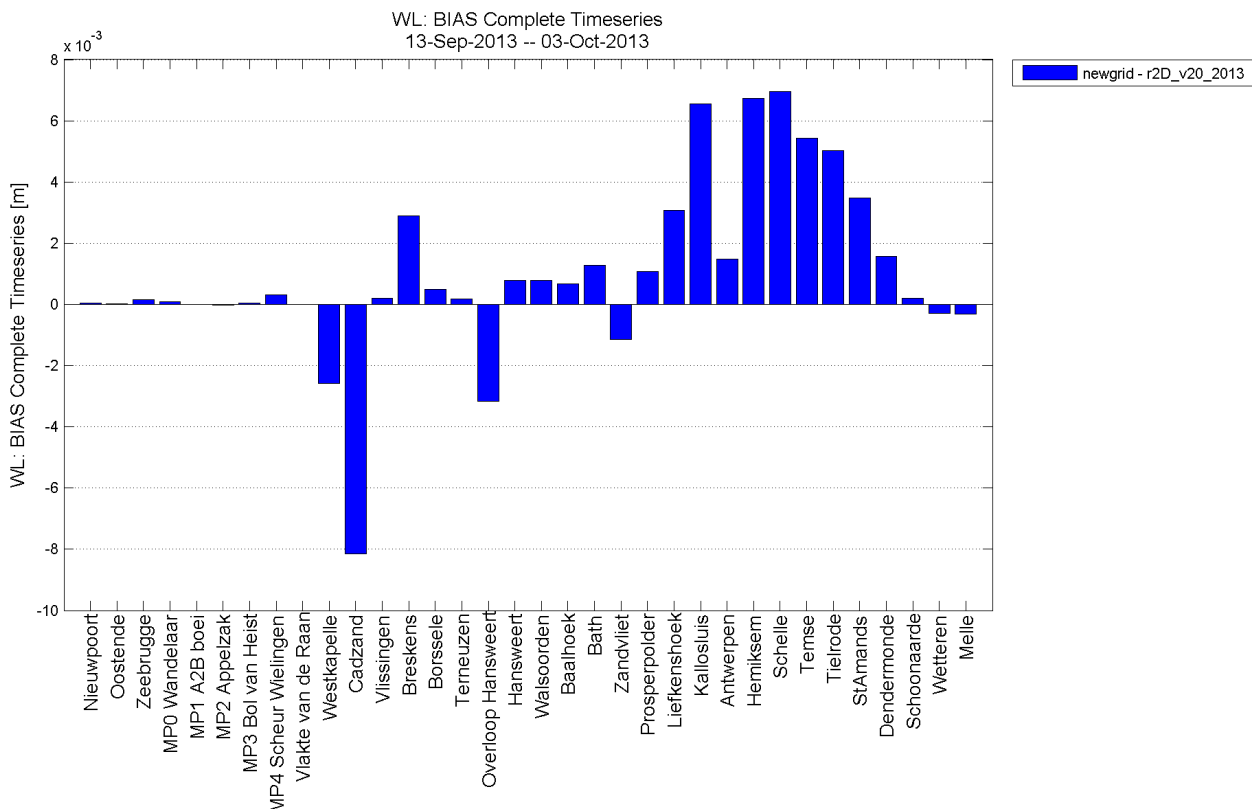


Figure 54 – Average high water level difference along the estuary between a model simulation with the newly adapted grid (newgrid) and the original grid (r2d\_v20\_2013).

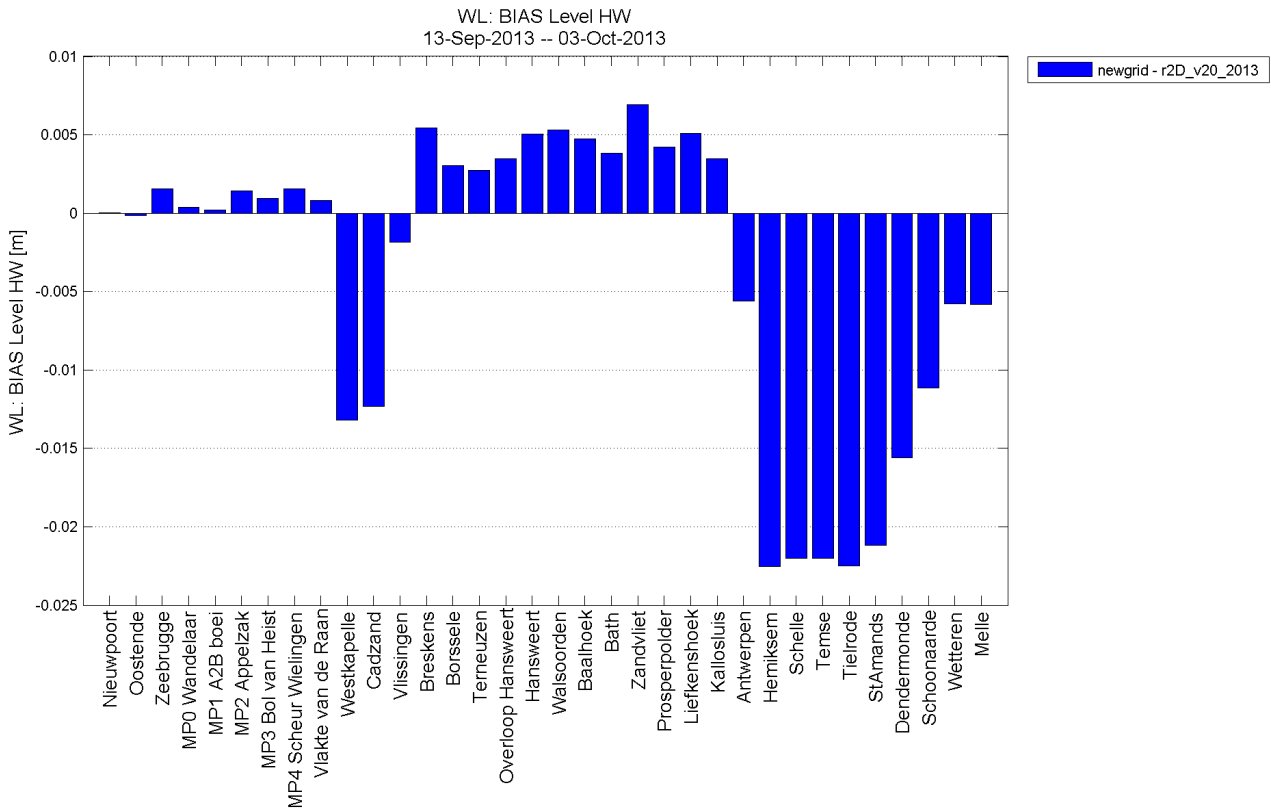
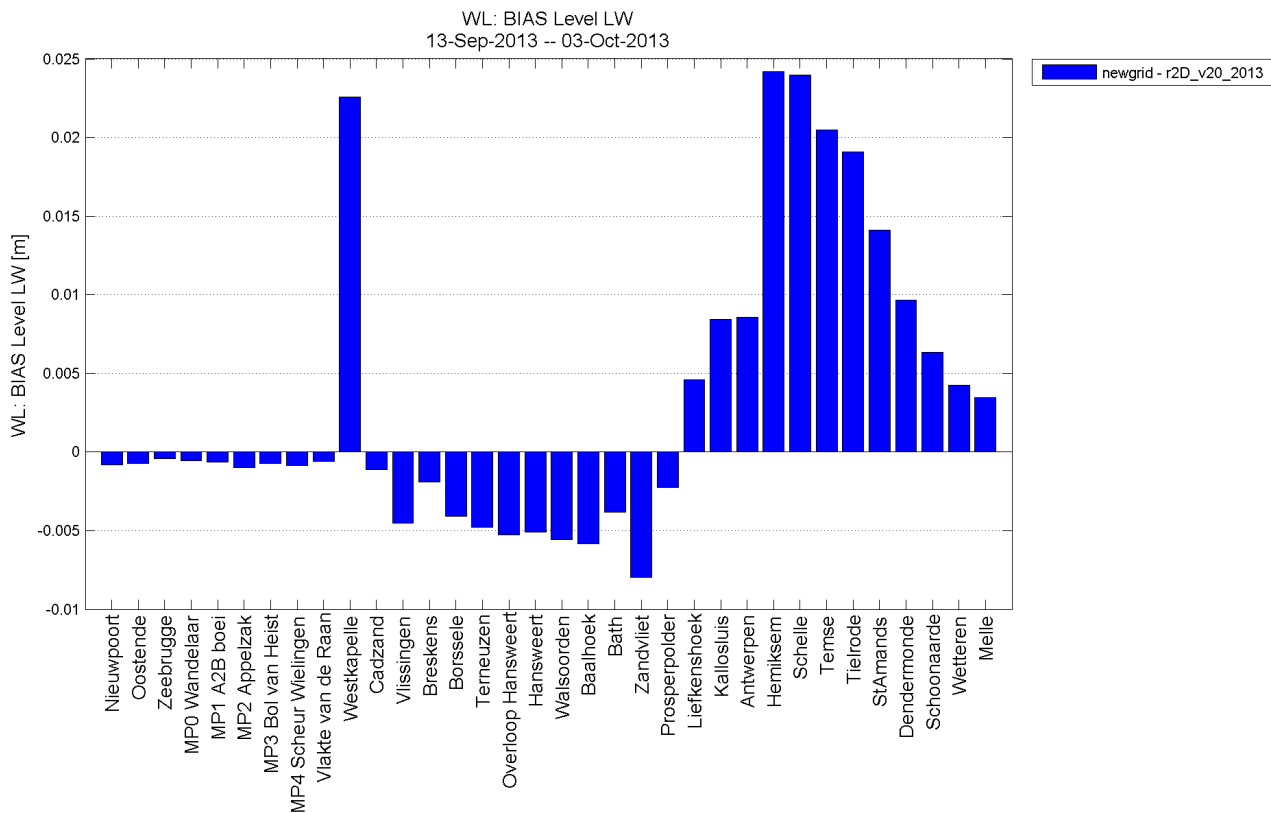


Figure 55 – Average low water level difference along the estuary between a model simulation with the newly adapted grid (newgrid) and the original grid (r2d\_v20\_2013).



### 10.3 Sensitivity Analysis: effect of discharge at Bath

The effect of omitting the discharge at Spuikanaal Bath (near the Bath tidal station in Figure 1) is briefly assessed by comparing model results of a simulation with the Scaldis 2013 model (with the new model grid) in which this discharge is included (2013\_V7P2r0) and a simulation in which the discharge at Bath is not included (noBath).

Figure 56 – Figure 58 depict the effect of omitting this discharge boundary on the full water level time series along the estuary, high water levels along the estuary and low water levels along the estuary and offshore along the Belgian coast. Based on these figures, the impact of the discharge at Bath (Spuikanaal) on water levels along the estuary is less than 0.001 m and hence negligible.

Figure 56 – Average effect of omitting the discharge at Bath on water level time series along the estuary.

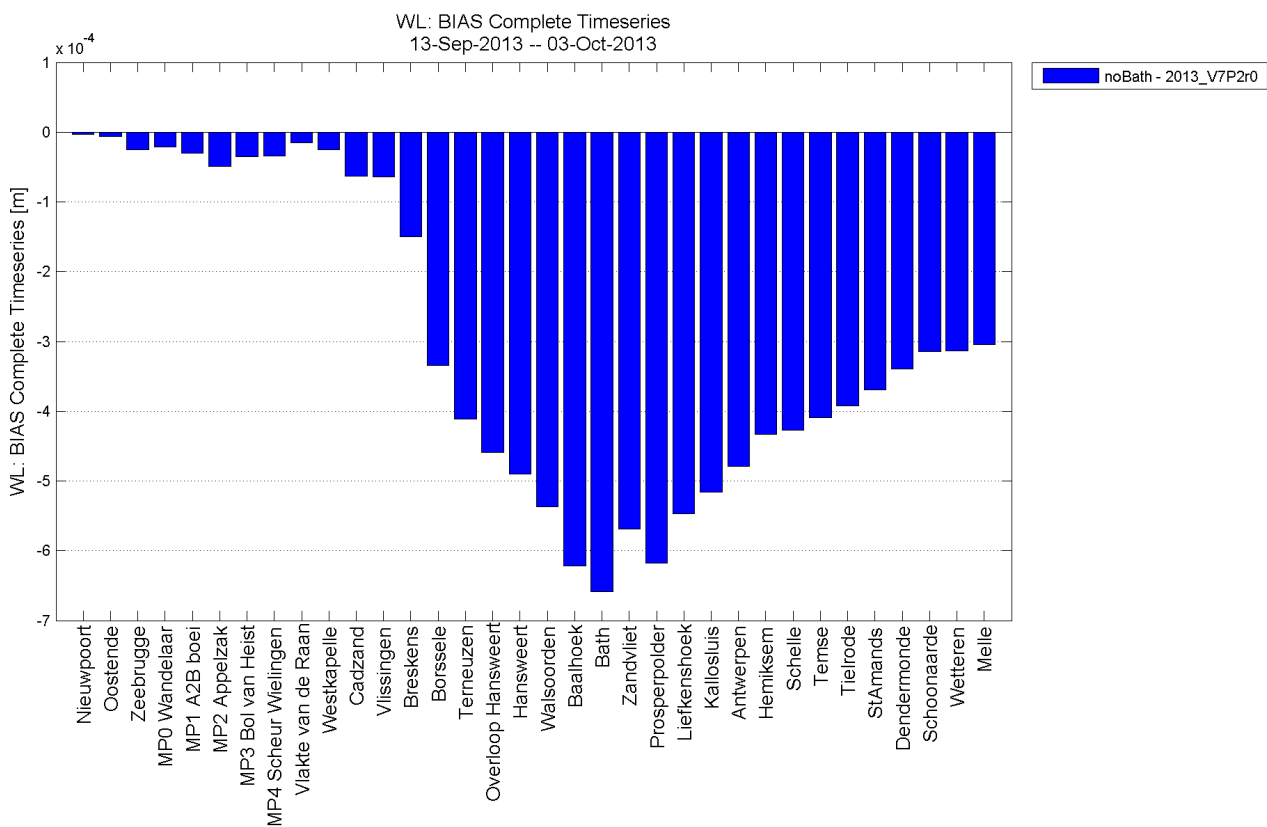


Figure 57 – Average effect of omitting the discharge at Bath on water level time series along the estuary.

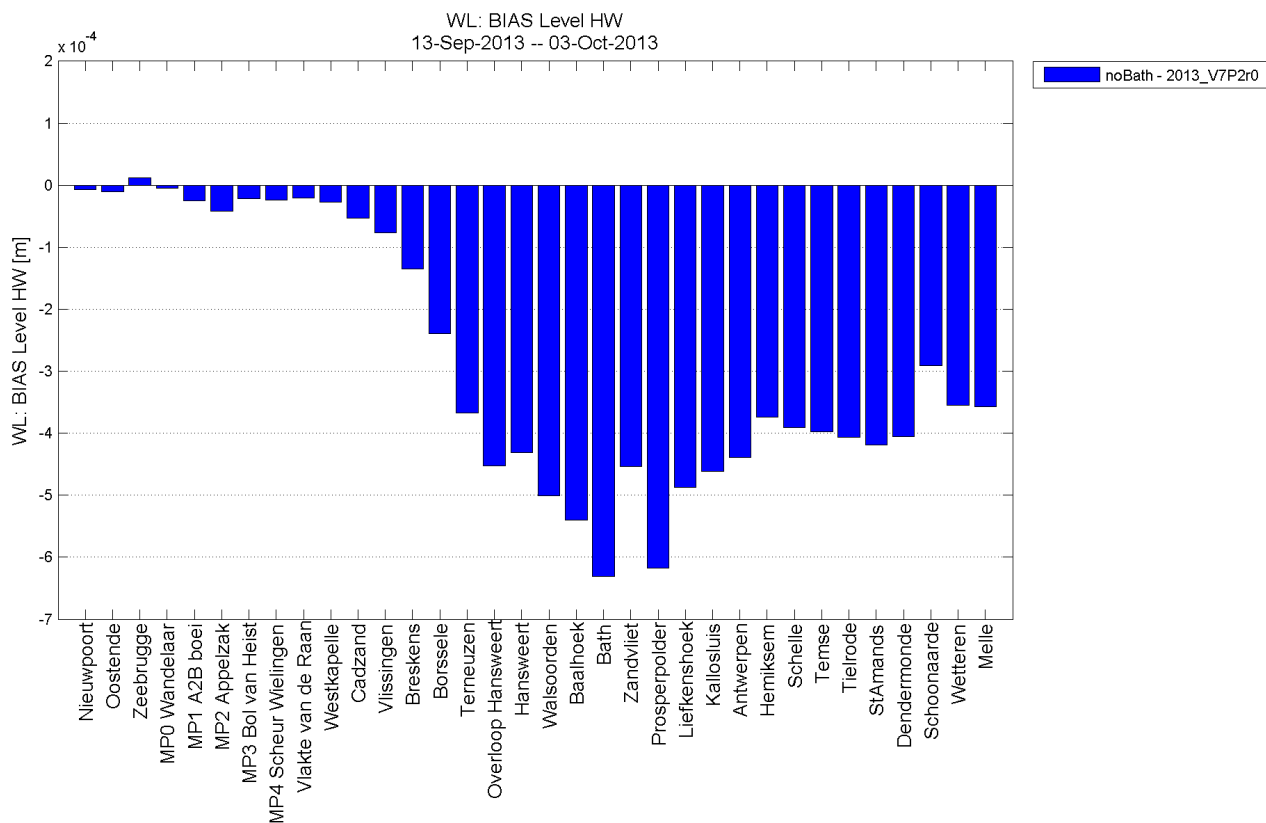
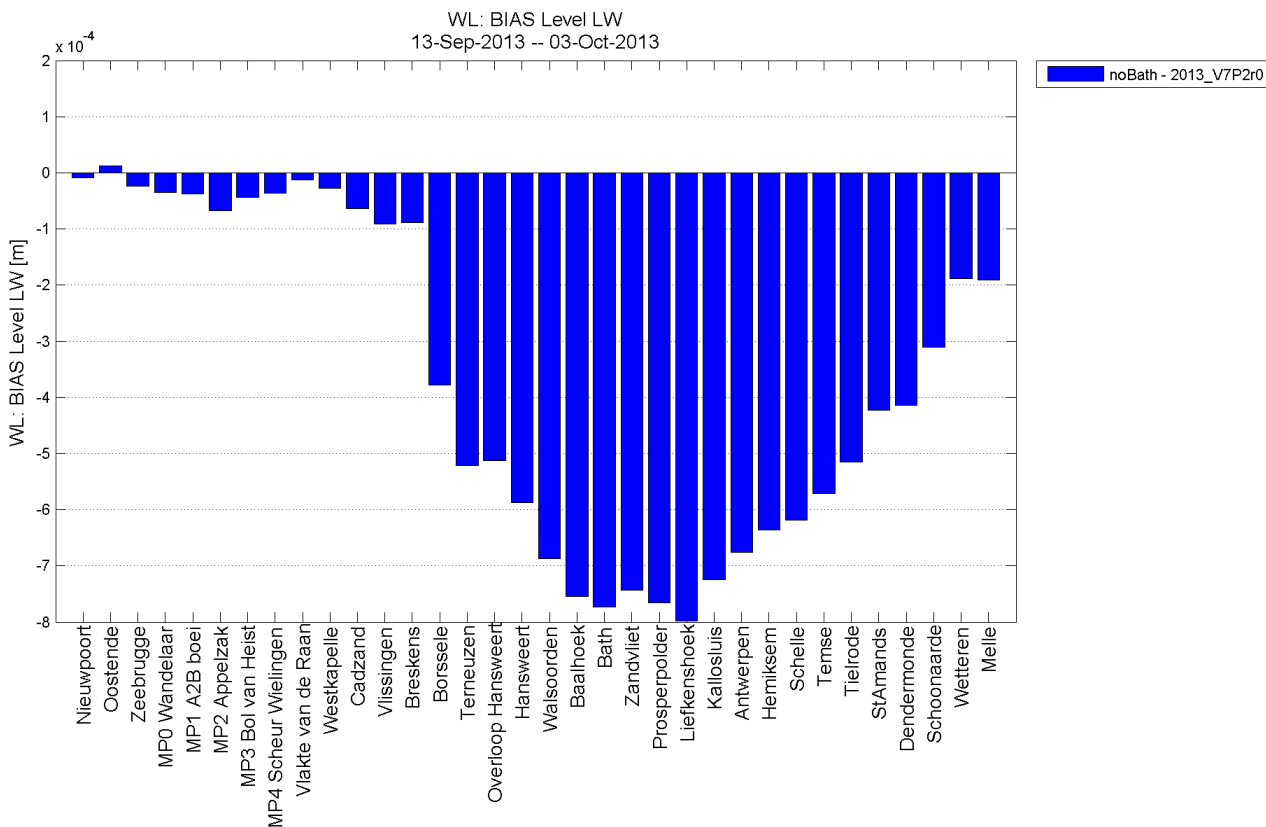


Figure 58 – Average effect of omitting the discharge at Bath on water level time series along the estuary.



## 10.4 Initial model performance with the Scaldis2013 bottom friction field

Figure 59 until Figure 63 depict the mean errors (BIAS) of each historical model for high and low water levels. Similarly, Figure 64 until Figure 68 depict the mean errors (BIAS) of each historical model for the timing of the high and low waters. The BIAS-values are calculated over a period of two weeks.

Figure 59 – HWL BIAS (top) and LWL BIAS (bottom) for the 1930 model with the Scaldis2013 friction field.

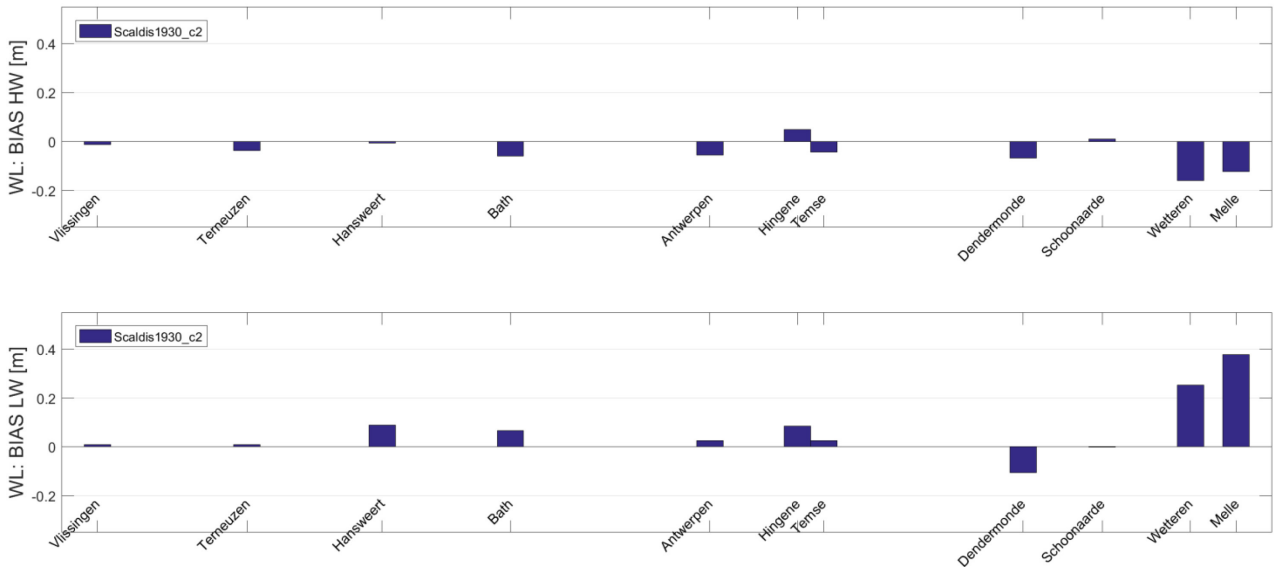


Figure 60 – HWL BIAS (top) and LWL BIAS (bottom) for the 1960 model with the Scaldis2013 friction field.

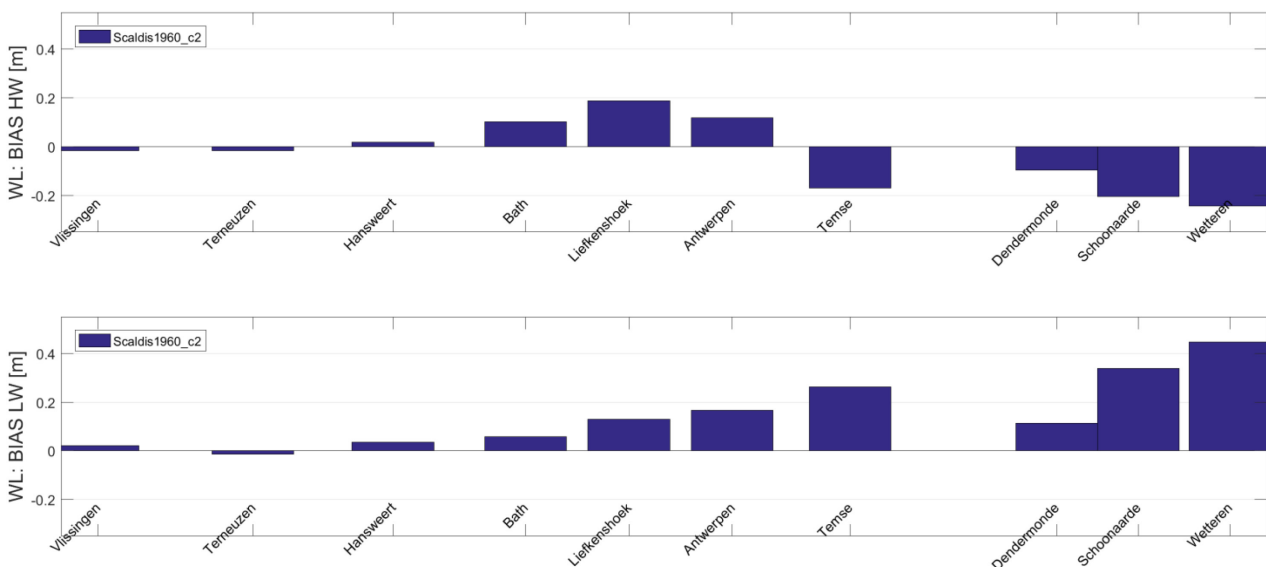


Figure 61 – HWL BIAS (top) and LWL BIAS (bottom) for the 1980 model with the Scaldis2013 friction field.

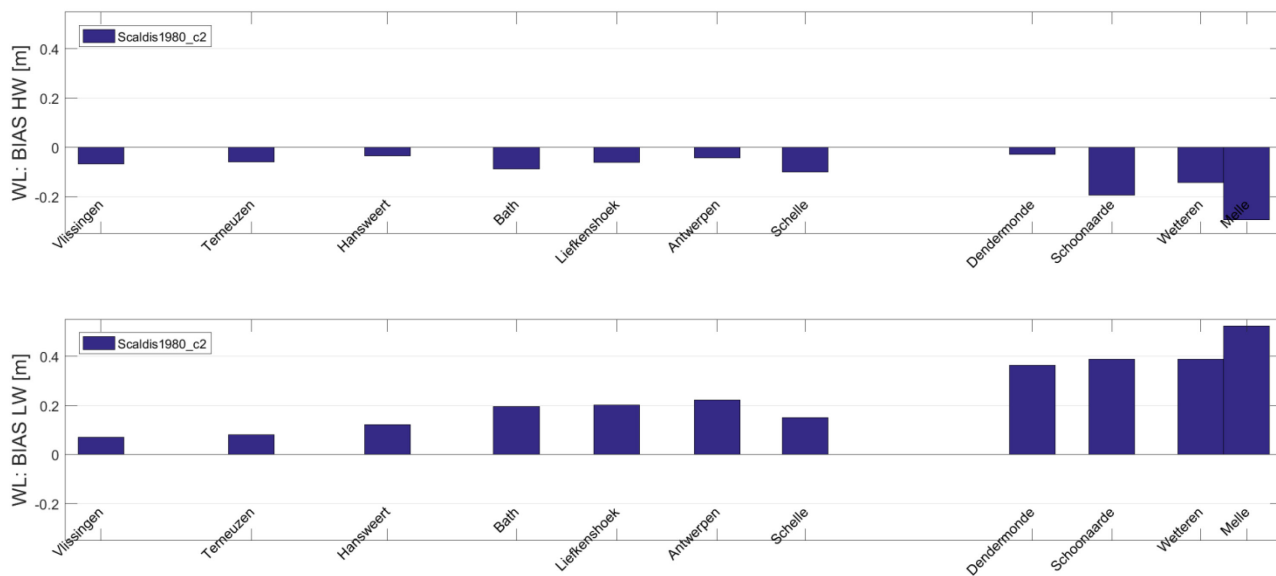


Figure 62 – HWL BIAS (top) and LWL BIAS (bottom) for the 2001 model with the Scaldis2013 friction field.

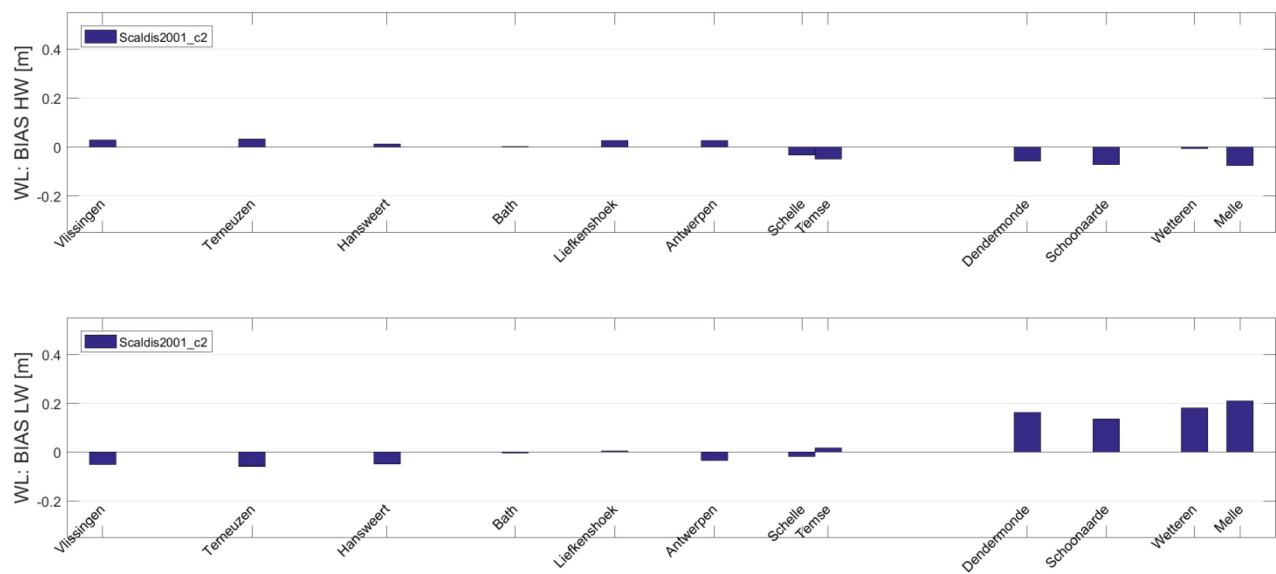


Figure 63 – HWL BIAS (top) and LWL BIAS (bottom) for the 2013 model with the Scaldis2013 friction field.

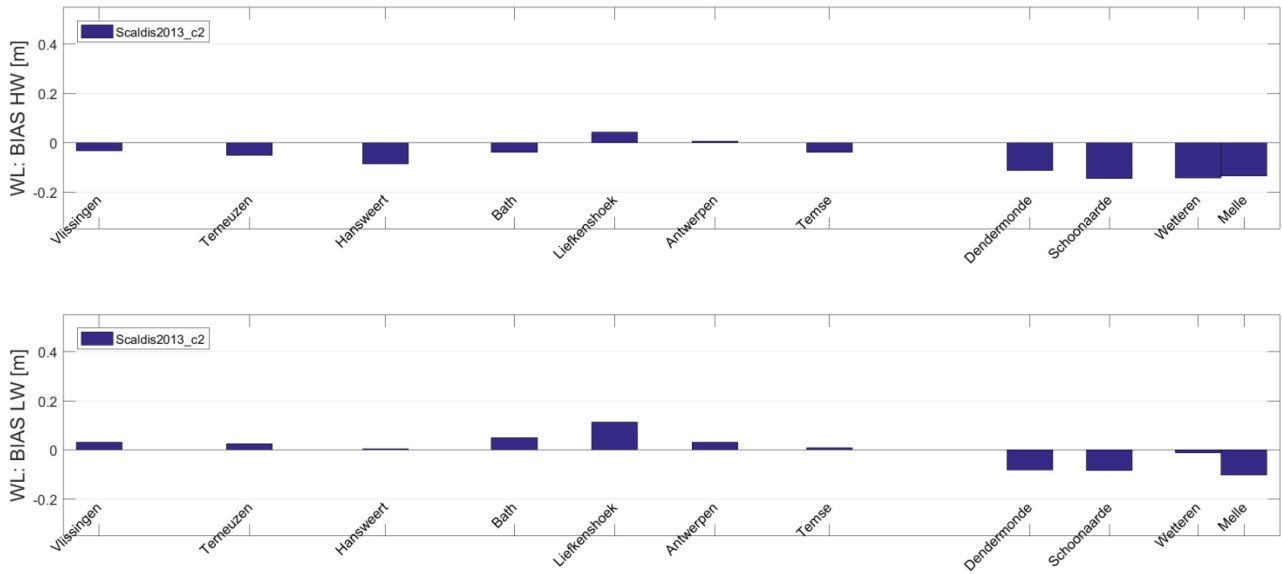


Figure 64 – THW BIAS (top) and TLW BIAS (bottom) for the 1930 model with the Scaldis2013 friction field.

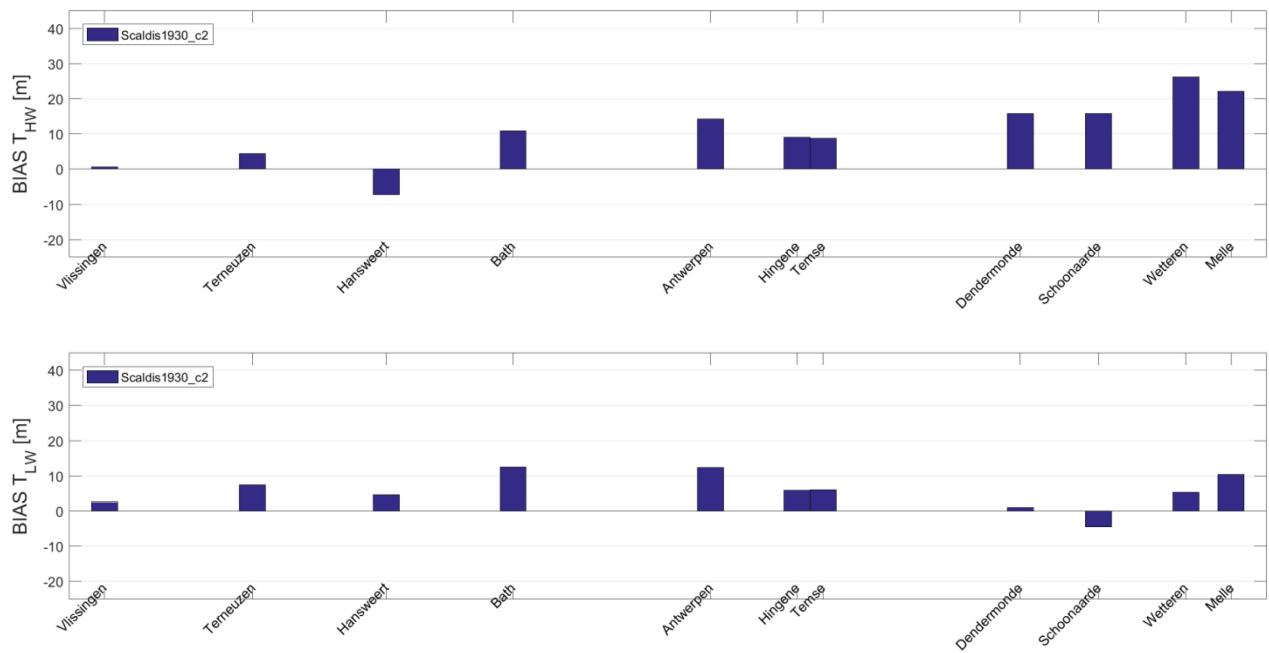


Figure 65 – THW BIAS (top) and TLW BIAS (bottom) for the 1960 model with the Scaldis2013 friction field.

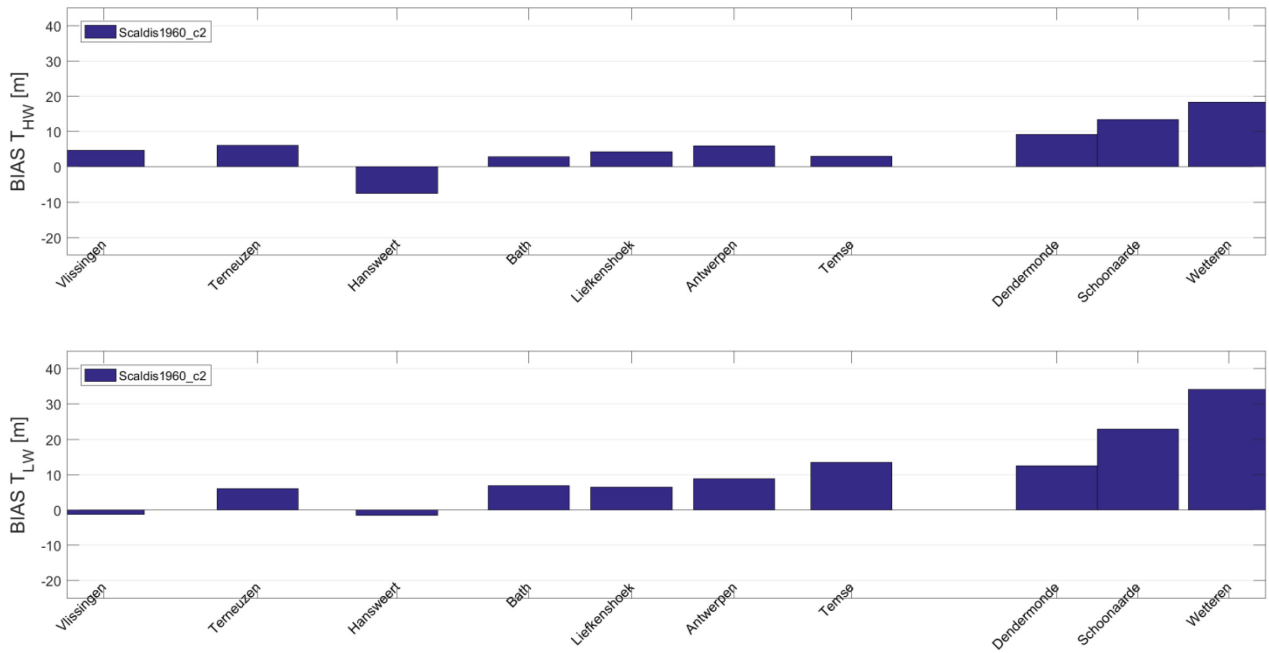


Figure 66 – THW BIAS (top) and TLW BIAS (bottom) for the 1980 model with the Scaldis2013 friction field.

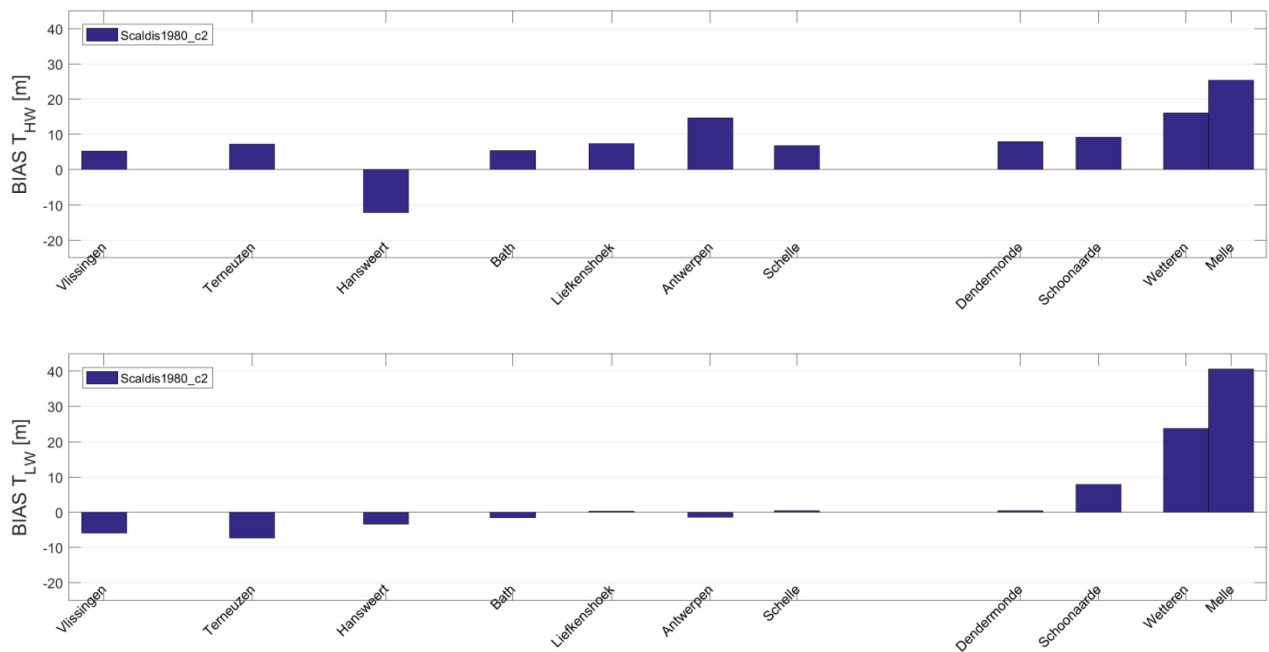


Figure 67 – THW BIAS (top) and TLW BIAS (bottom) for the 2001 model with the Scaldis2013 friction field.

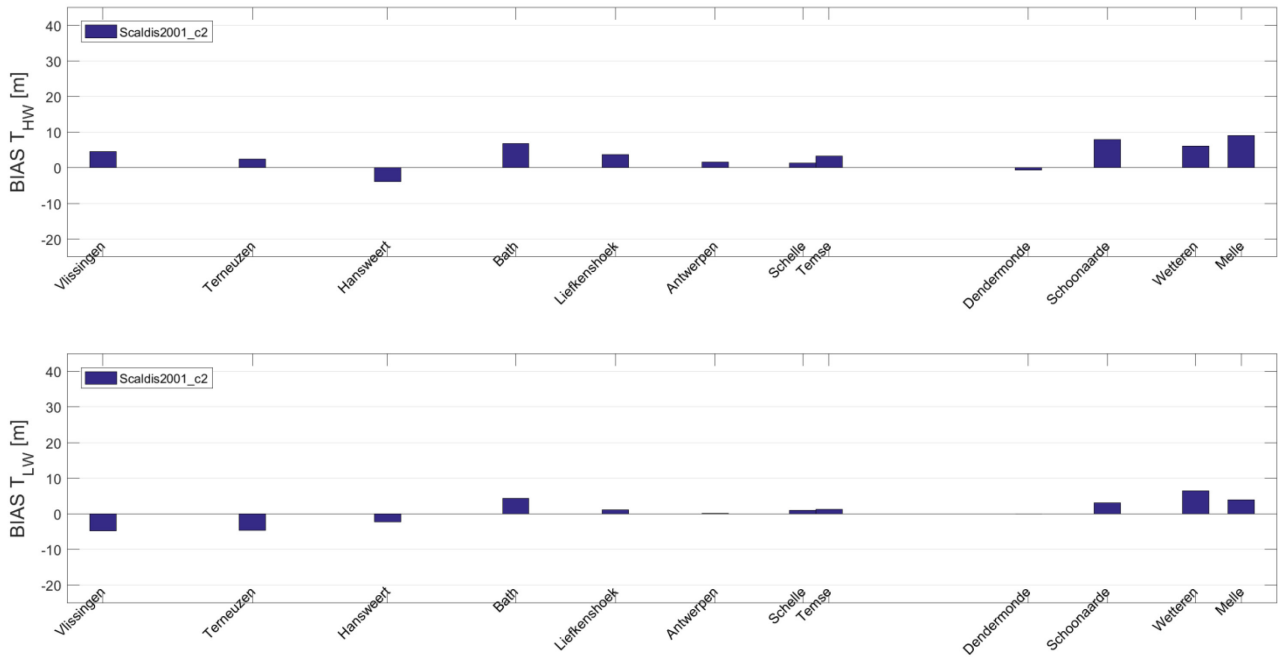
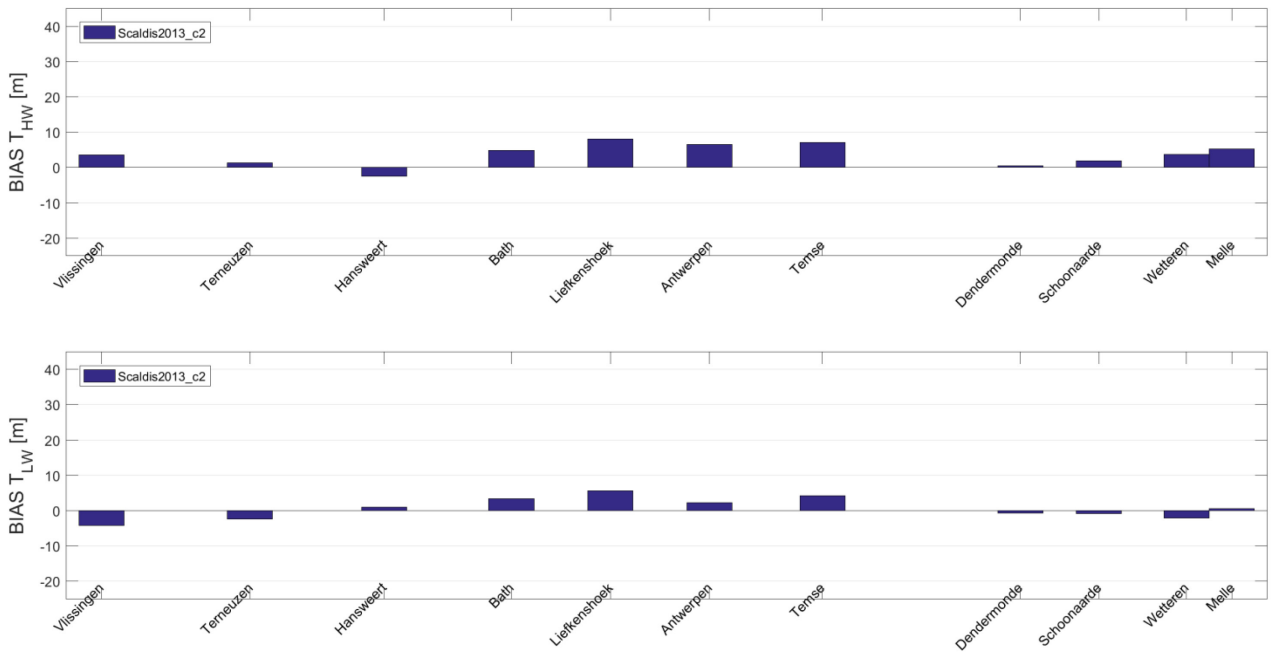


Figure 68 – THW BIAS (top) and TLW BIAS (bottom) for the 2013 model with the Scaldis2013 friction field.



## 10.5 Evaluation of peak discharges in simulation period

The simulation period is chosen based on minimal surge at the offshore or downstream boundary. Moreover, surge effects have been implemented into the downstream boundary conditions by evaluating the difference signal between modelled and measured water levels at Vlissingen and adding a centered moving average to the boundary condition time series (§4.6.4). However, peak discharges at the upstream boundaries may still be present in the simulation periods. Such events may influence high and low water levels in the upstream part of the estuary (i.e., upstream of Dendermonde).

The presence of peak discharge in the simulation periods may, depending on the timing of the discharge peak relative to the high- and low water levels, influence the model performance during the calibration process, as the upstream discharges are only implemented as daily averages. This may filter out peaks and hence their effects on water levels in the upstream part of the estuary. Moreover, the 1930 and 1960 models are forced by constant discharges, implying that possible peak discharges are not included at all. More specifically, high discharges lead to high water levels and hence higher high- and low water levels. If these peak discharges are not (adequately) represented by the upstream boundary conditions, the model is likely to underestimate high and low water levels in the upstream part of the estuary.

The effect of peak discharges in the simulation period is assessed with the surge signals at two stations along the estuary: Antwerpen in the Lower sea Scheldt and Wetteren. At Antwerpen, the surge signal is almost entirely the result of the offshore boundary conditions and wind setup along the estuary, while the surge signal at Wetteren is also largely influenced by upstream discharges from Merelbeke or Gentbrugge (see Figure 1 for locations of these tidal stations). Evaluation of the difference between the surge signal in Wetteren and the surge signal in Antwerpen then gives an indication of the part of the surge caused by peak discharges in the upstream part of the estuary.

The surge signal is calculated for each simulation period by subtracting a mean water level from the moving average of two high water levels and two low water levels (i.e., filtering out the semi-diurnal signal) at each tidal station. The mean water level is on its turn defined as the mean of all high water levels and low water levels in a simulated year. The difference signal between the surge signal at Wetteren and Antwerpen is simply computed by subtraction of the two surge signals.

Figure 69 – Figure 73 show the discharge-induced surge signals at Wetteren during the simulation periods of the historical models, obtained by the above-described method. Positive values for the discharge-induced surge signal suggest a higher than average upstream discharge, whereas negative values for the discharge-induced surge signal suggest a lower than average discharge. A distinct discharge-induced surge peak of almost one meter is present in the 2013 simulation period (Figure 73). This surge peak increases the individual high- and low water levels in Wetteren by up to +1.5 m, in Dendermonde by up to +0.5 m and is not distinguishable anymore in tidal stations further downstream. For the model calibration, an underestimation of both high- and low water levels may thus be expected in the 2013 model as the peak discharge is only implemented as a daily averaged value, possibly leading to an underestimation of the discharge peak. Furthermore, the 1930, 1960, 1980 and 2001 simulation periods contain discharge-induced water level variations between -0.4 m and +0.4 m. A somewhat stronger discharge-induced surge peak is present during the first days of the 1980 simulation period, but this surge peak is outside the part of the simulation that is assessed during the model calibration (i.e., the period is within the hydrodynamic spin-up time of the model).

Besides, a comparison of the surge signal in Wetteren with the surge signal in Vlissingen instead of the surge signal in Antwerpen gives similar results. This comparison is however not presented in this report.

Figure 69 – Discharge induced surge signal at Wetteren for the 1930 simulation period, calculated as the difference between the surge signal at Wetteren and the surge signal at the more downstream located tidal station of Antwerpen.

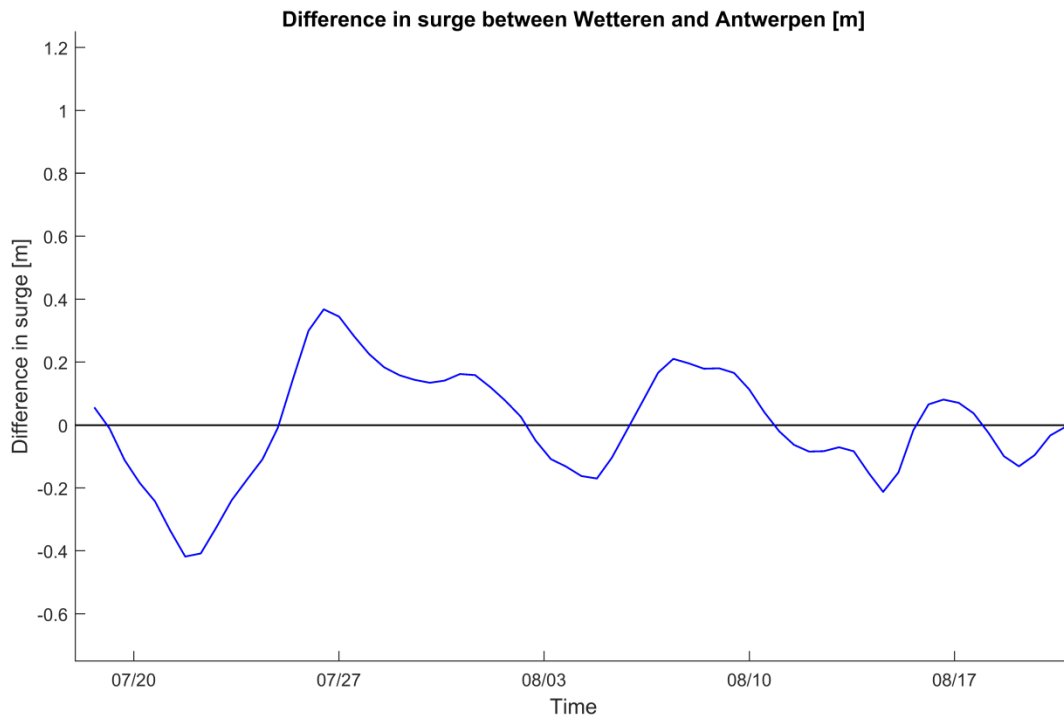


Figure 70 – Discharge induced surge signal at Wetteren for the 1960 simulation period, calculated as the difference between the surge signal at Wetteren and the surge signal at the more downstream located tidal station of Antwerpen.

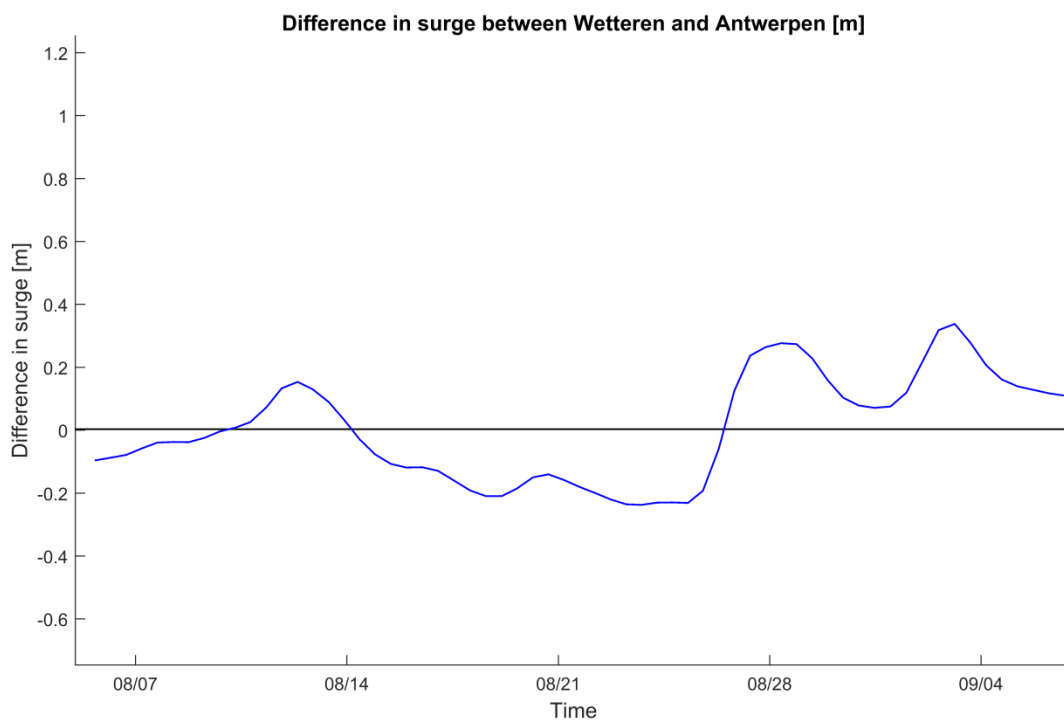


Figure 71 – Discharge induced surge signal at Wetteren for the 1980 simulation period, calculated as the difference between the surge signal at Wetteren and the surge signal at the more downstream located tidal station of Antwerpen.

---

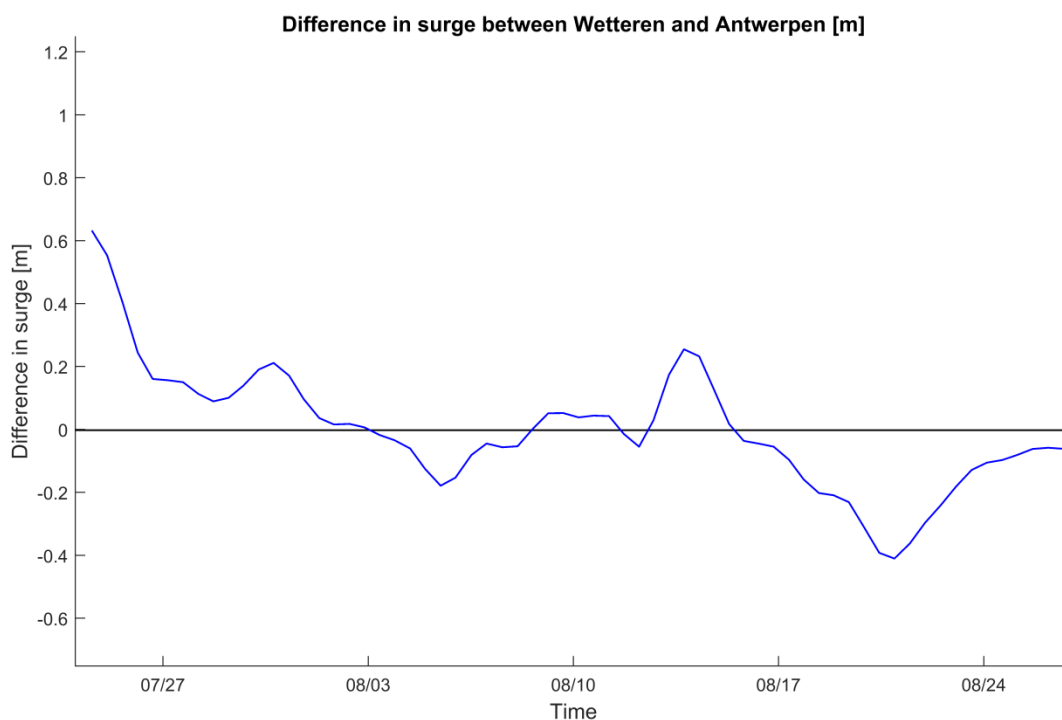


Figure 72 – Discharge induced surge signal at Wetteren for the 2001 simulation period, calculated as the difference between the surge signal at Wetteren and the surge signal at the more downstream located tidal station of Antwerpen.

---

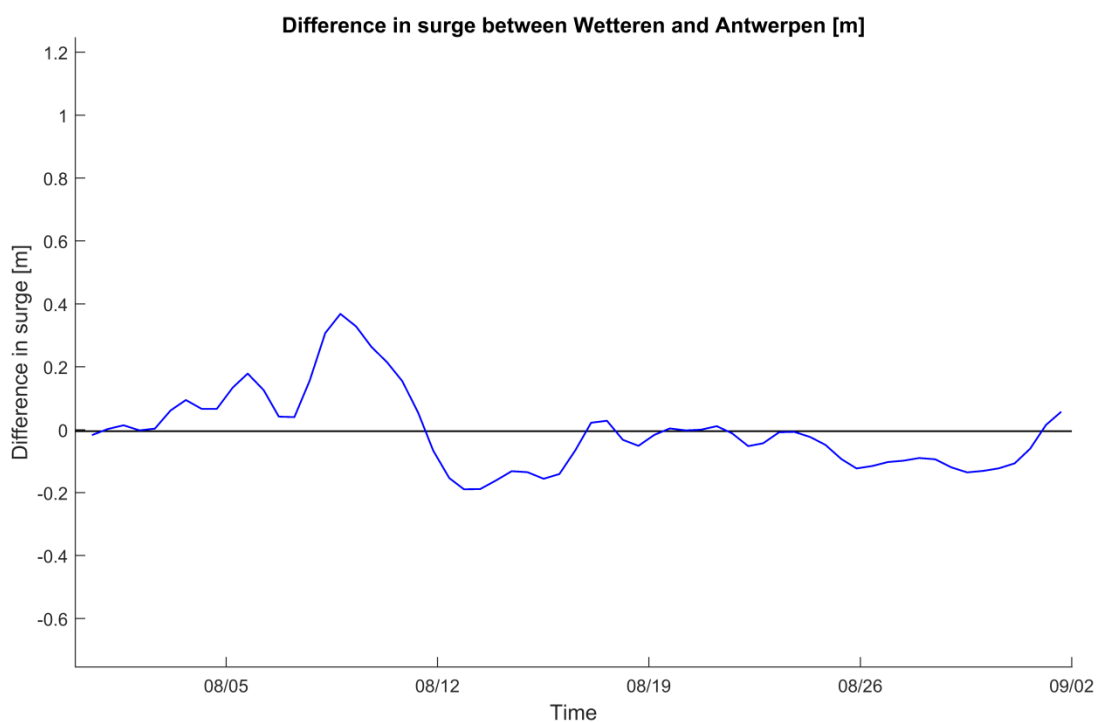
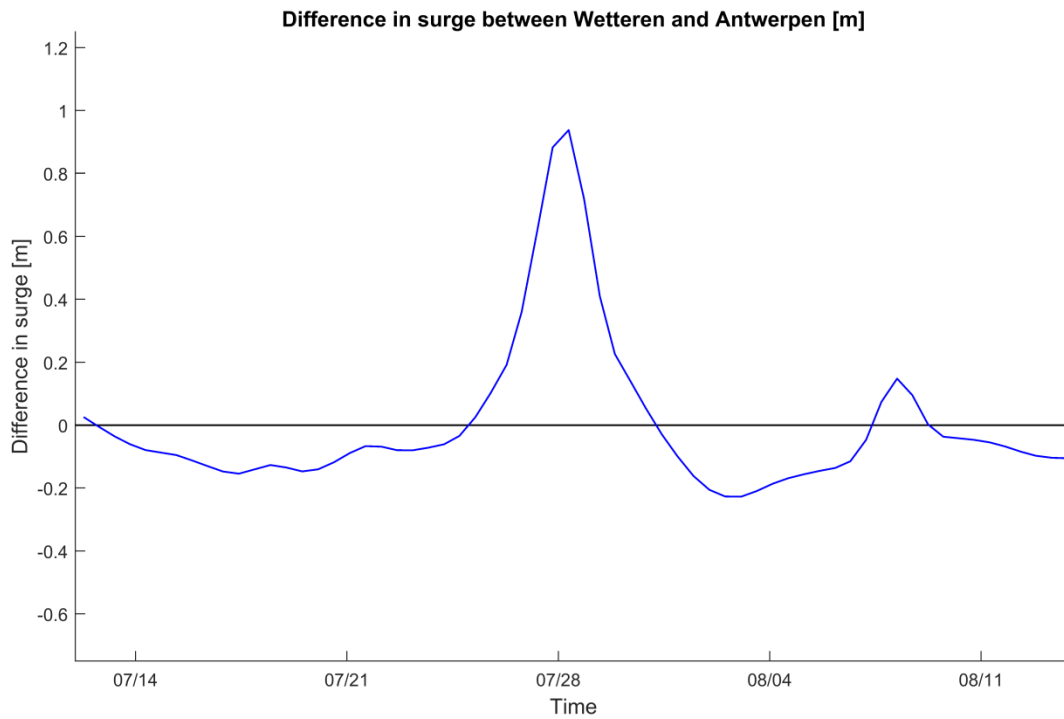


Figure 73 – Discharge induced surge signal at Wetteren for the 2013 simulation period, calculated as the difference between the surge signal at Wetteren and the surge signal at the more downstream located tidal station of Antwerpen.



## 10.6 Results of calibration runs: RMSE of HW, LW, $T_{HW}$ and $T_{LW}$

### Calibration runs for Western Scheldt section (cal01, cal02 and cal03)

See Table 9 for an overview of the friction coefficients per estuarine section in each calibration run.

Figure 74 – HWL RMSE (top) and LWL RMSE (bottom) for calibration runs cal01-cal03 with the 1930 model.

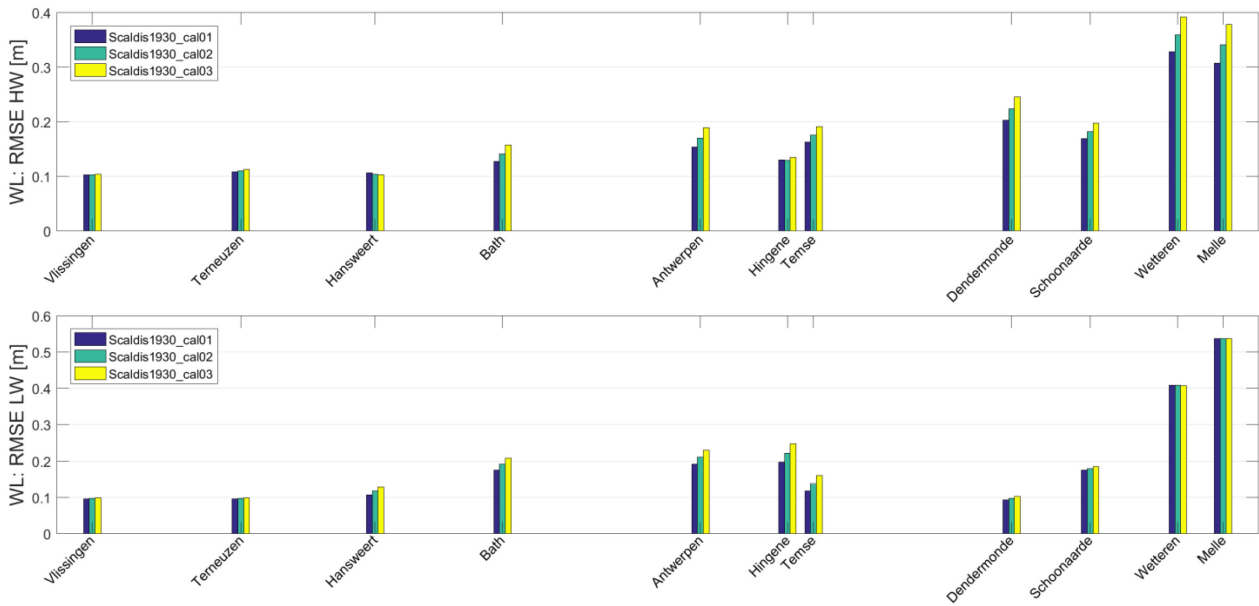


Figure 75 –  $T_{HW}$  RMSE (top) and  $T_{LW}$  RMSE (bottom) for calibration runs cal01-cal03 with the 1930 model.

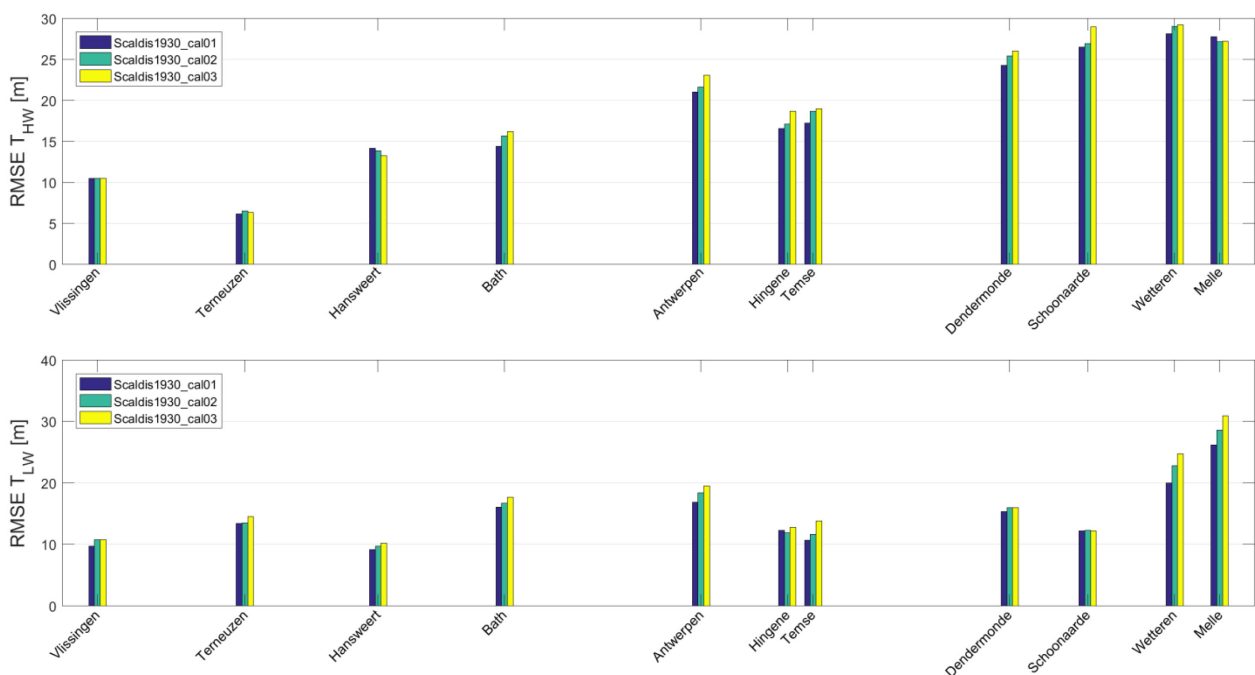


Figure 76 – HWL RMSE (top) and LWL RMSE (bottom) for calibration runs cal01-cal03 with the 1960 model.

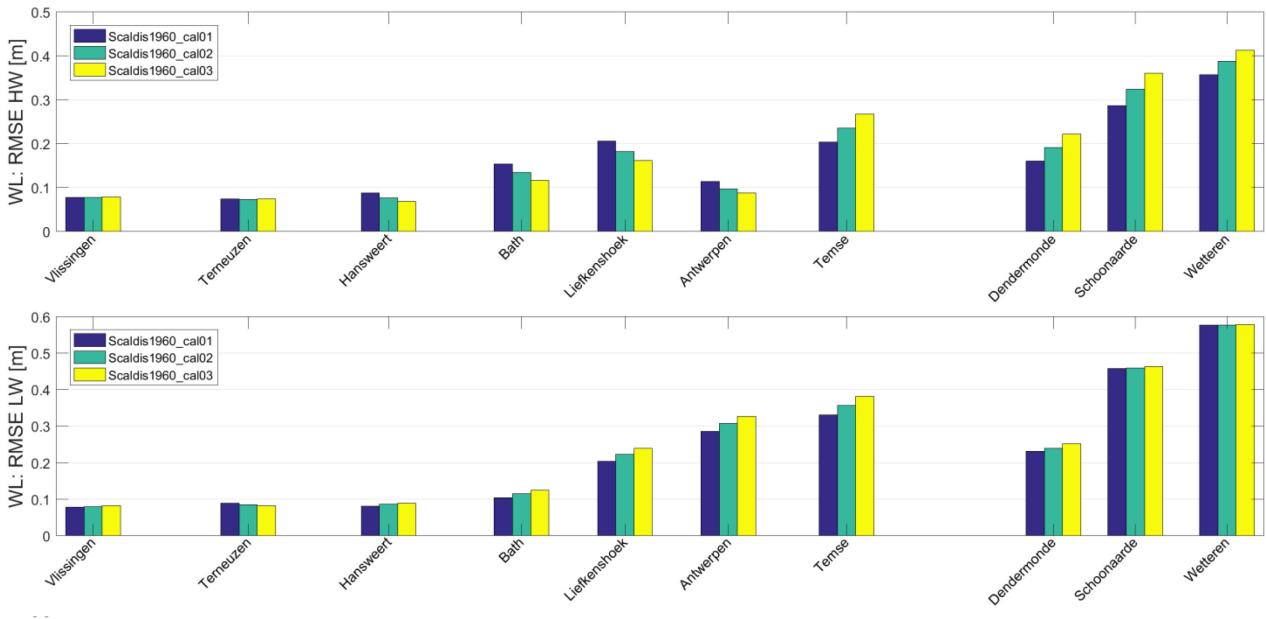


Figure 77 – THW RMSE (top) and TLW RMSE (bottom) for calibration runs cal01-cal03 with the 1960 model.

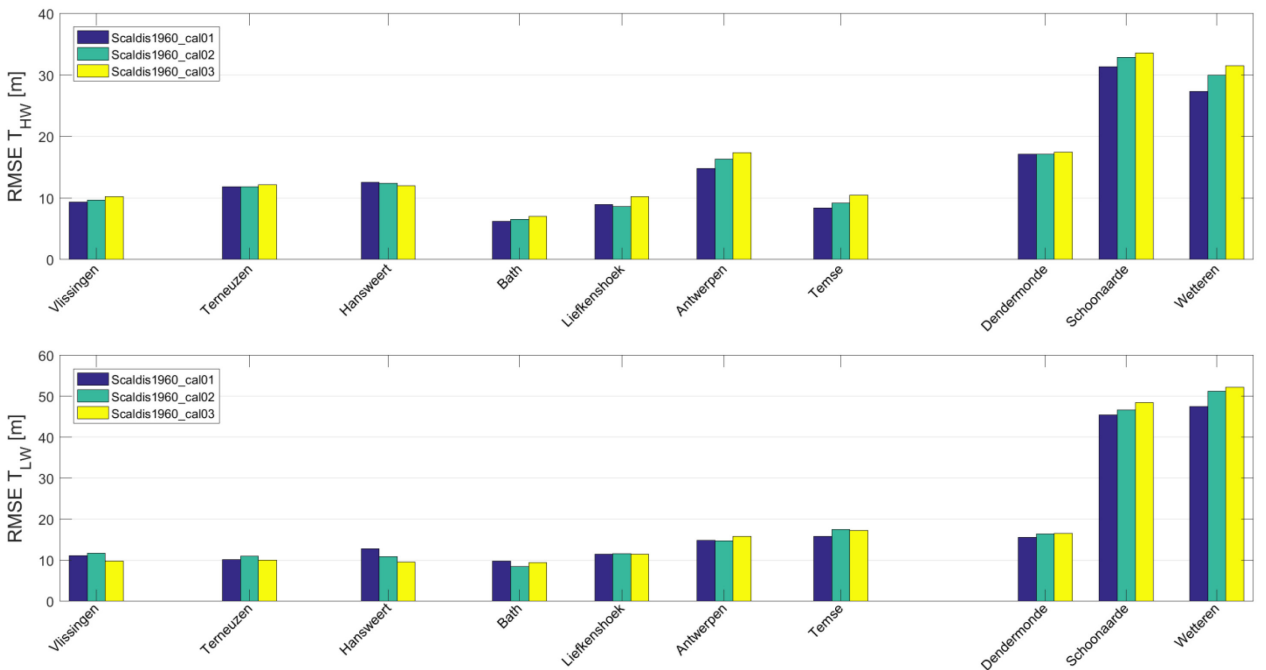


Figure 78 – HWL RMSE (top) and LWL RMSE (bottom) for calibration runs cal01-cal03 with the 1980 model

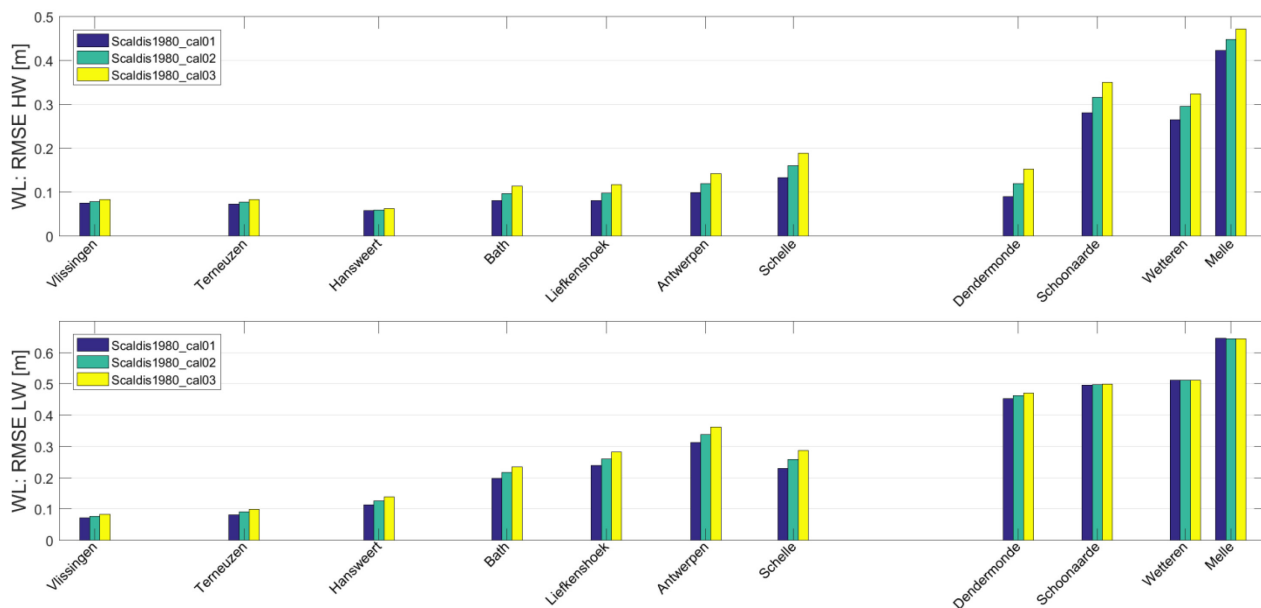


Figure 79 – THW RMSE (top) and TLW RMSE (bottom) for calibration runs cal01-cal03 with the 1980 model.

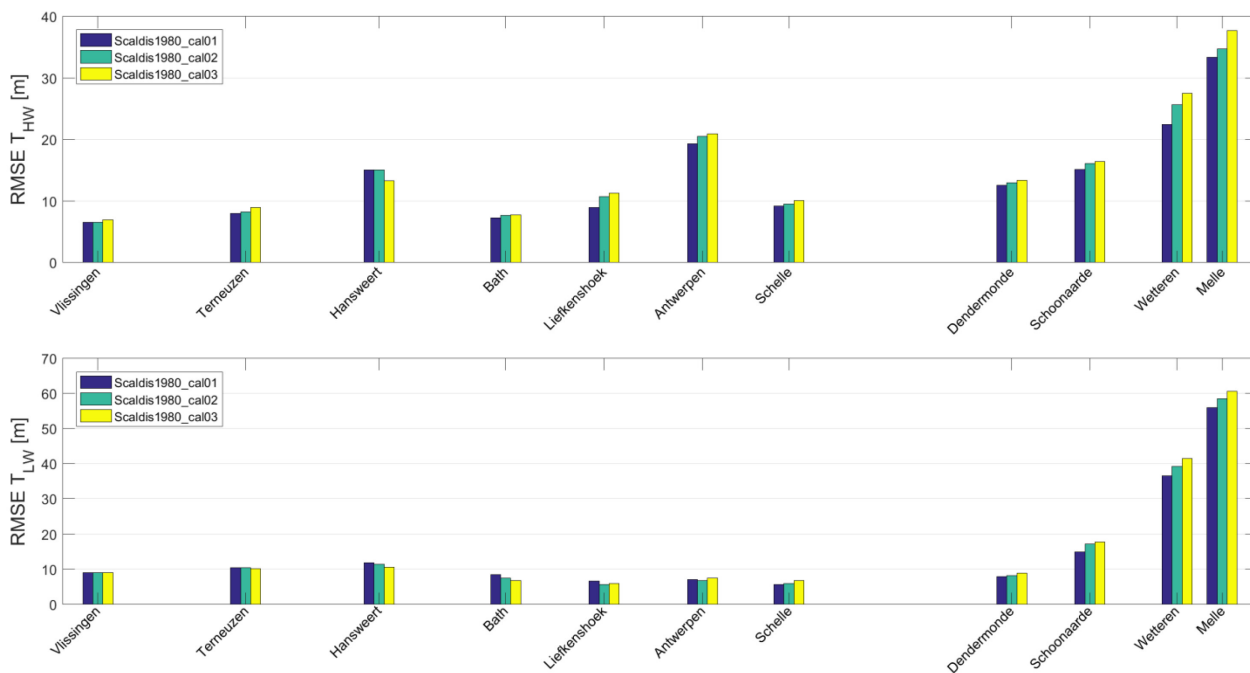


Figure 80 – HWL RMSE (top) and LWL RMSE (bottom) for calibration runs cal01-cal03 with the 2001 model.

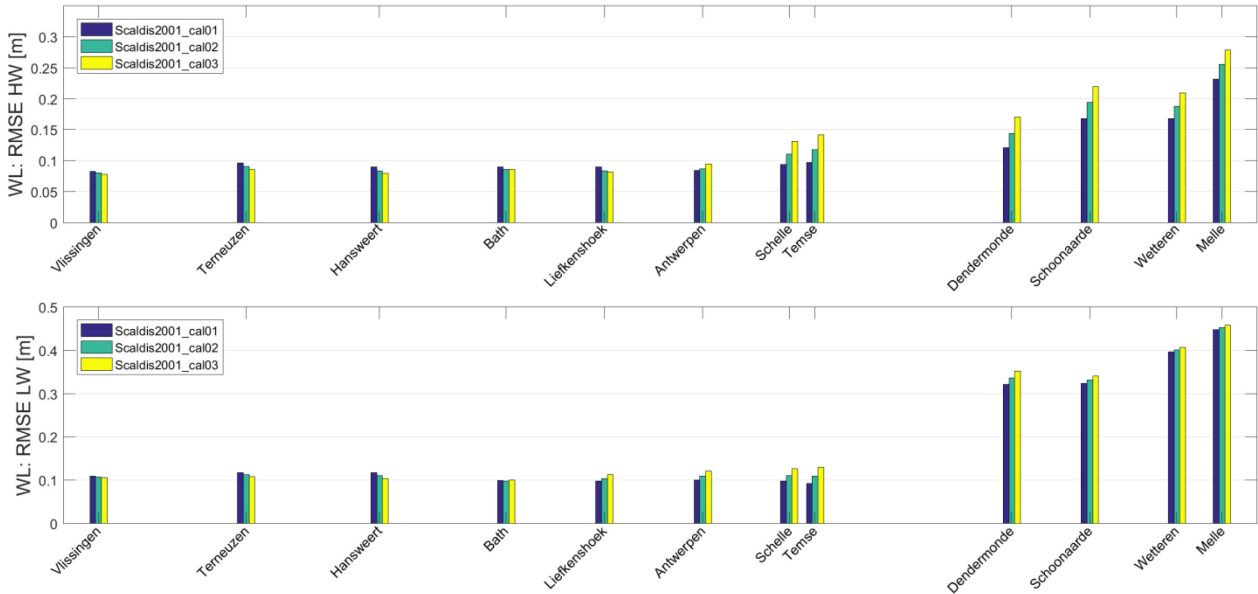


Figure 81 – THW RMSE (top) and TLW RMSE (bottom) for calibration runs cal01-cal03 with the 2001 model.

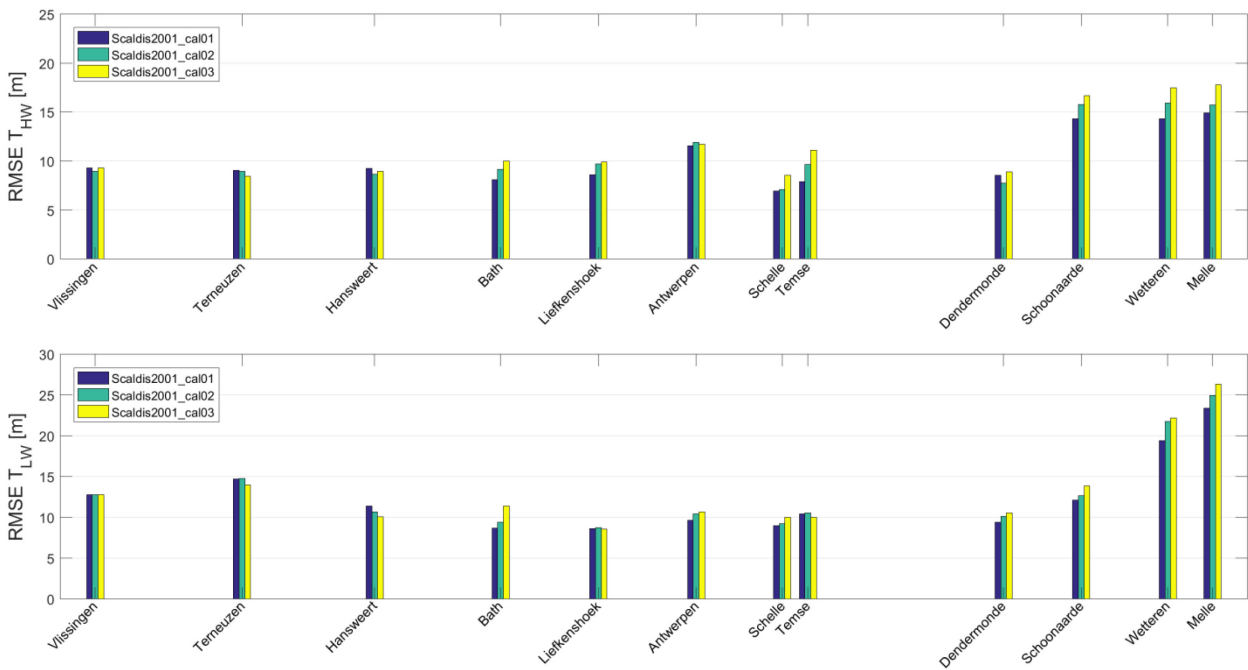


Figure 82 – HWL RMSE (top) and LWL RMSE (bottom) for calibration runs cal01-cal03 with the 2013 model.

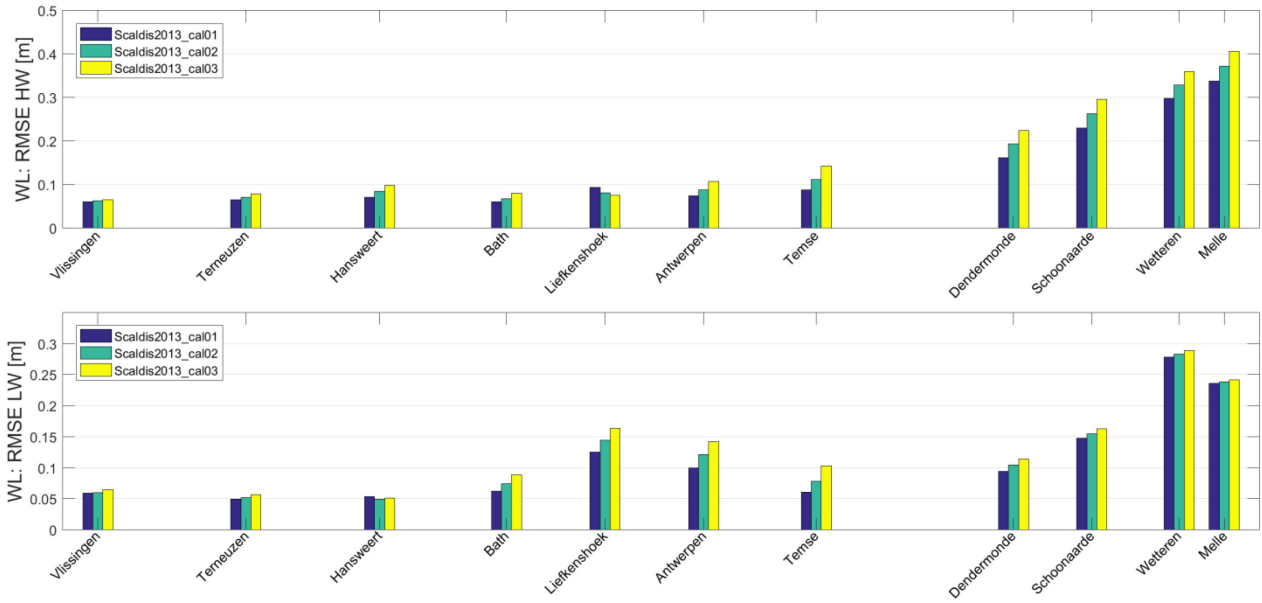
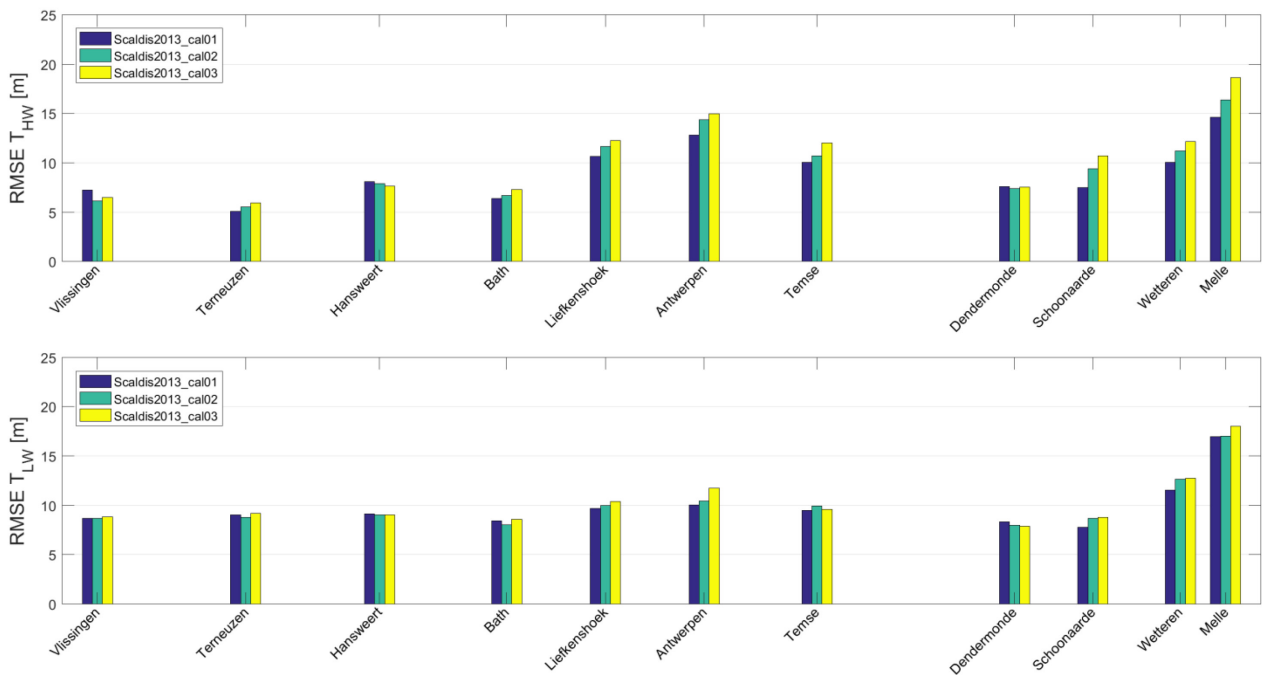


Figure 83 – THW RMSE (top) and TLW RMSE (bottom) for calibration runs cal01-cal03 with the 2013 model.



**Calibration runs for Lower Sea Scheldt section (cal11, cal12, cal13, cal14, cal15 and cal16)**

See Table 9 for an overview of the friction coefficients per estuarine section in each calibration run.

Figure 84 – HWL RMSE (top) and LWL RMSE (bottom) for calibration runs cal01 and cal11-cal16 with the 1930 model.

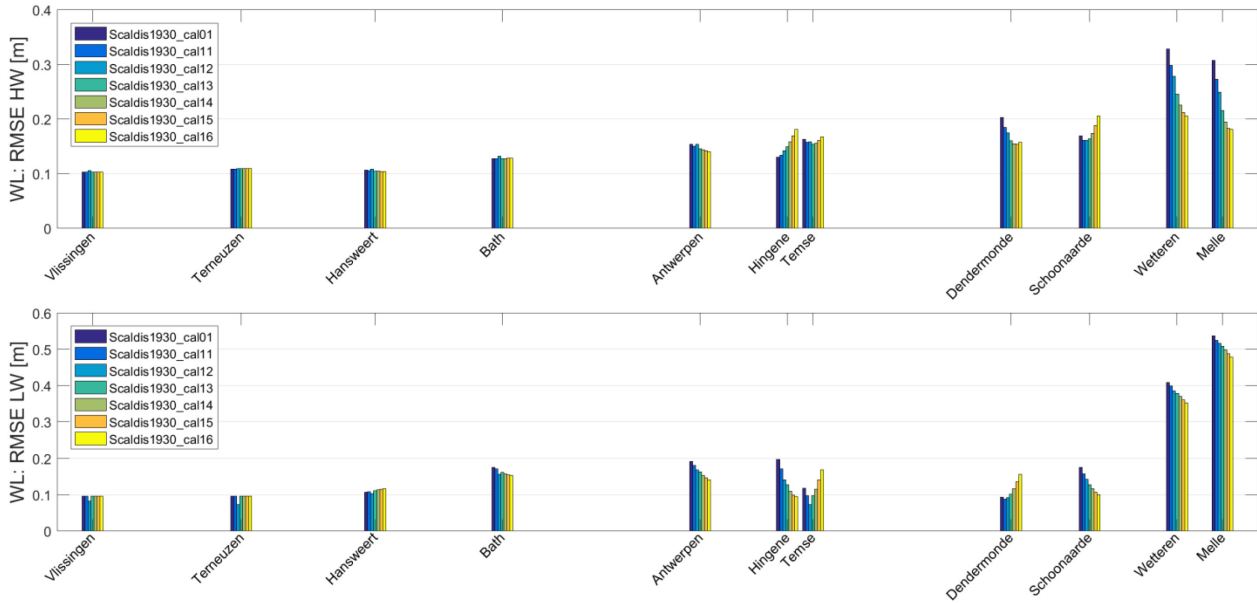


Figure 85 – THW RMSE (top) and TLW RMSE (bottom) for calibration runs cal01 and cal11-cal16 with the 1930 model.

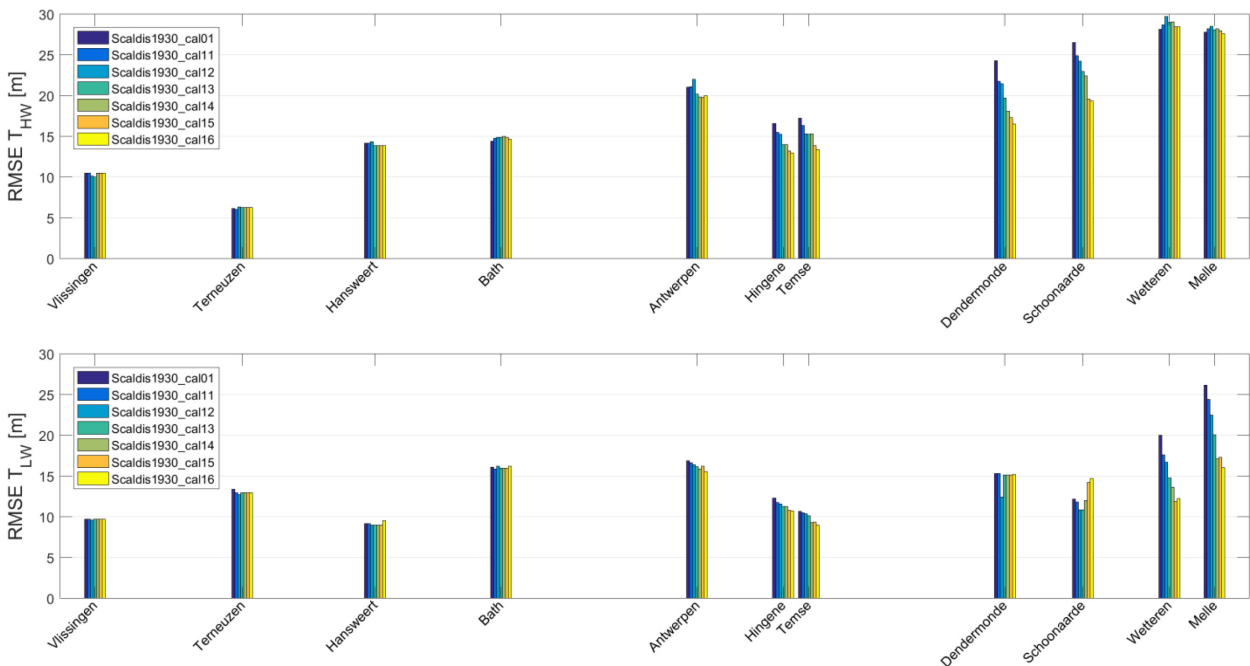


Figure 86 – HWL RMSE (top) and LWL RMSE (bottom) for calibration runs cal01 and cal11-cal16 with the 1960 model.

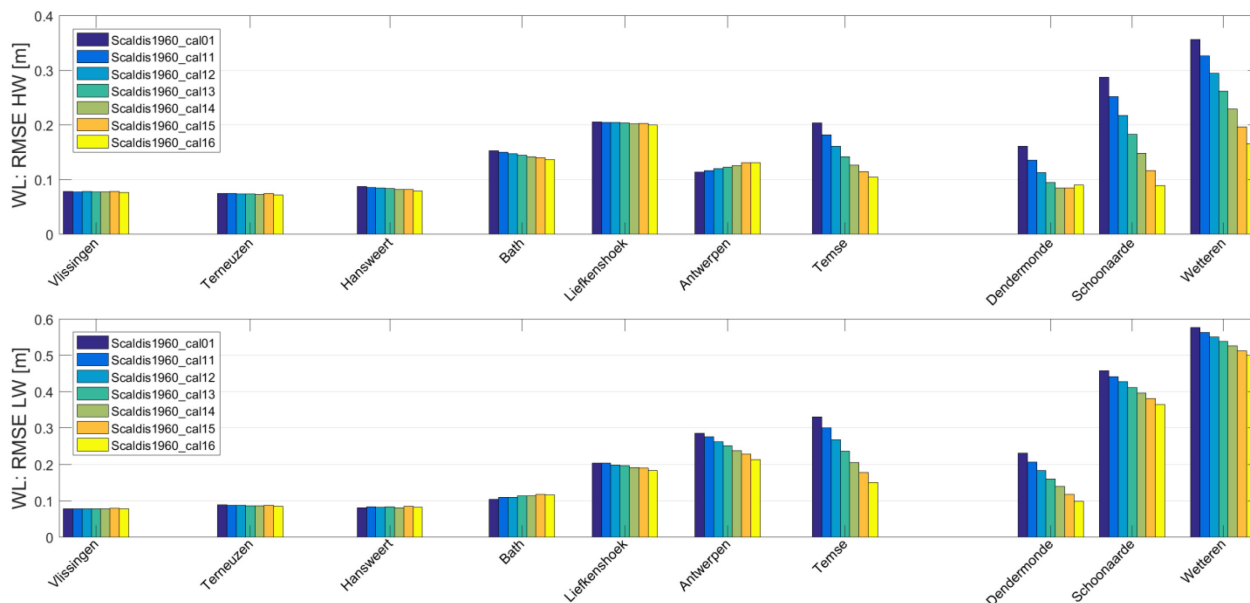


Figure 87 – THW RMSE (top) and TLW RMSE (bottom) for calibration runs cal01 and cal11-cal16 with the 1960 model.

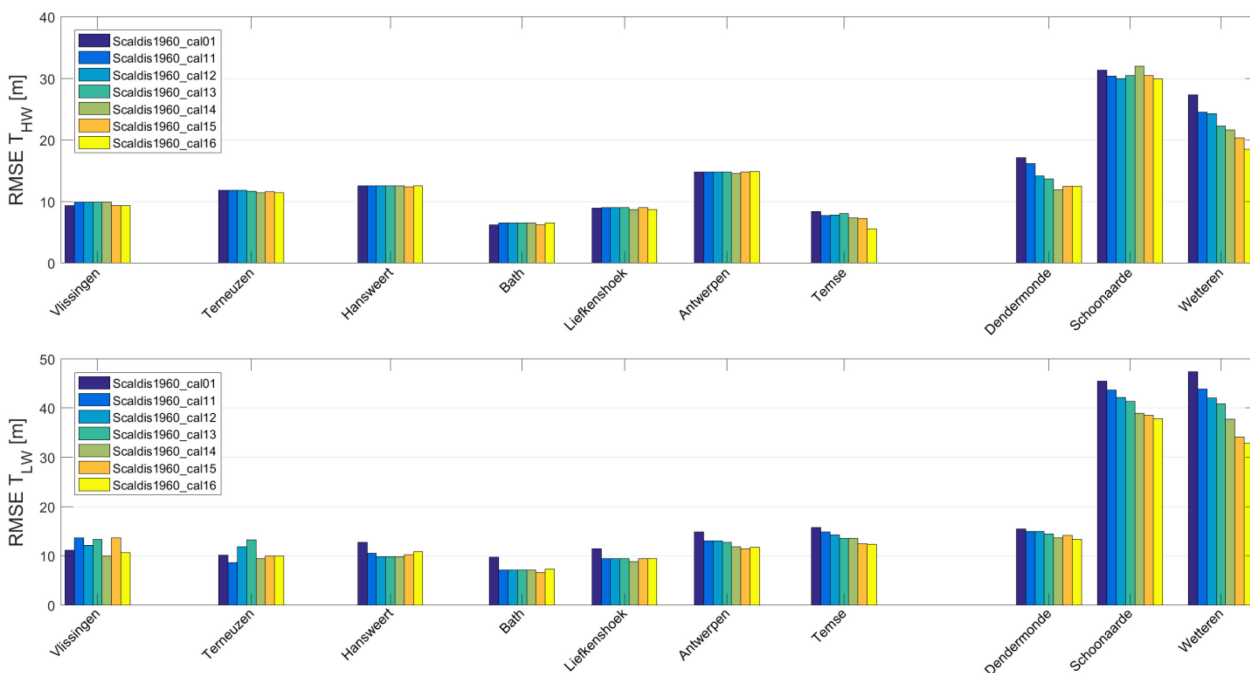


Figure 88 – HWL RMSE (top) and LWL RMSE (bottom) for calibration runs cal01 and cal11-cal16 with the 1980 model.

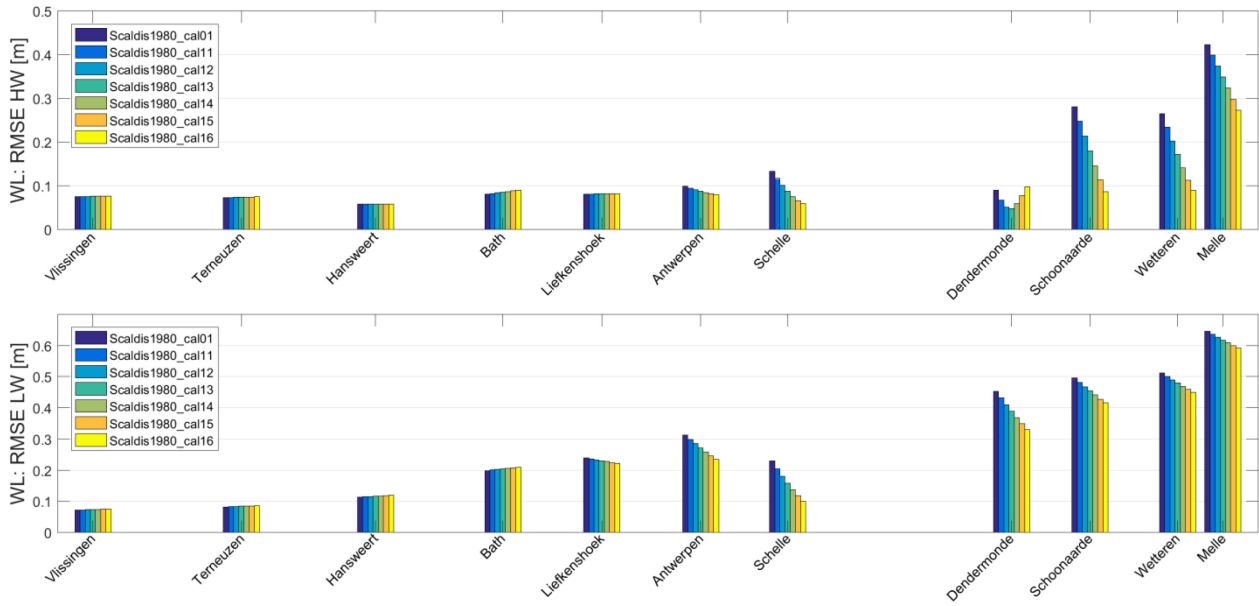


Figure 89 – THW RMSE (top) and TLW RMSE (bottom) for calibration runs cal01 and cal11-cal16 with the 1980 model.

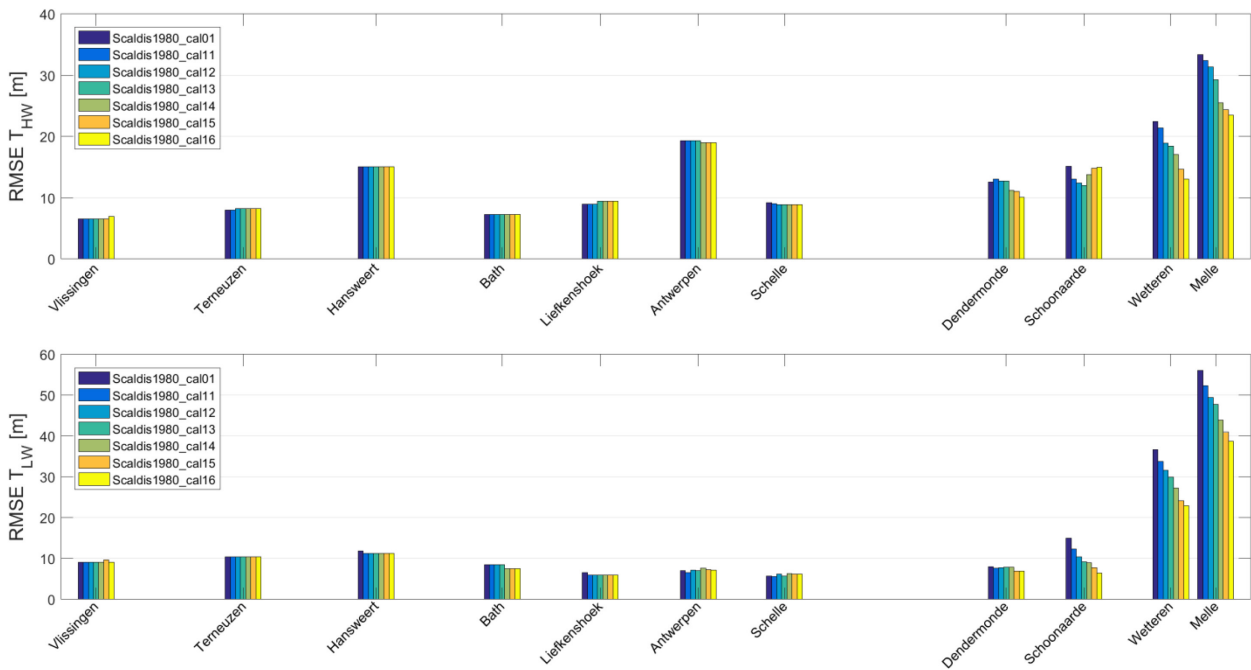


Figure 90 – HWL RMSE (top) and LWL RMSE (bottom) for calibration runs cal01 and cal11-cal16 with the 2001 model.

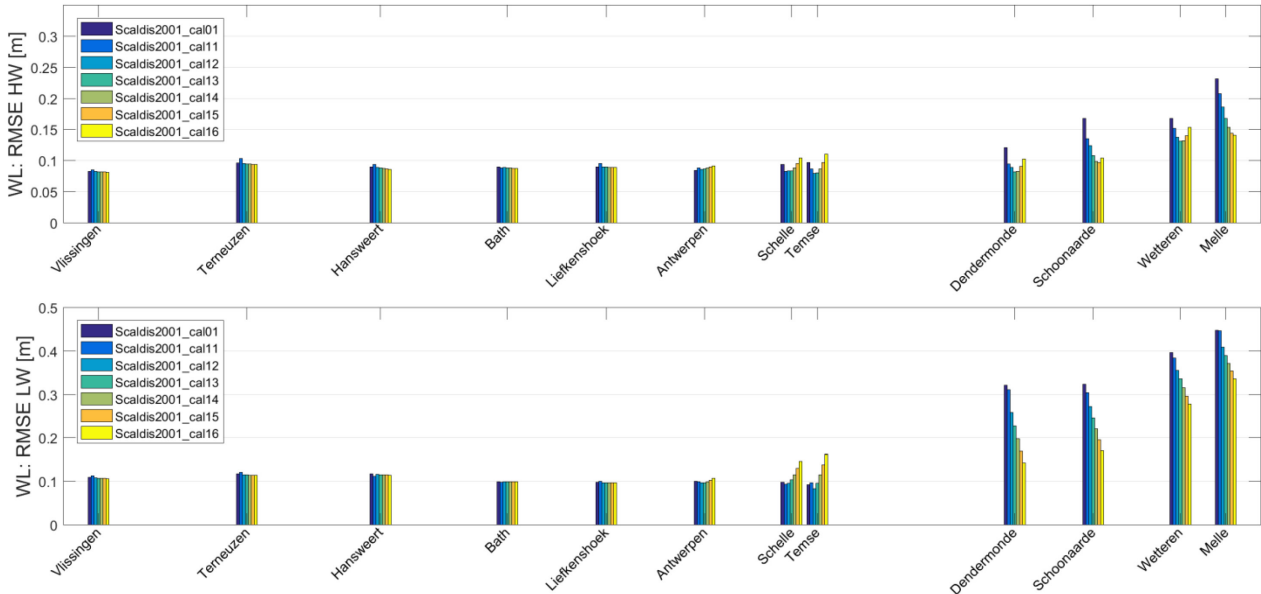


Figure 91 – THW RMSE (top) and TLW RMSE (bottom) for calibration runs cal01 and cal11-cal16 with the 2001 model.

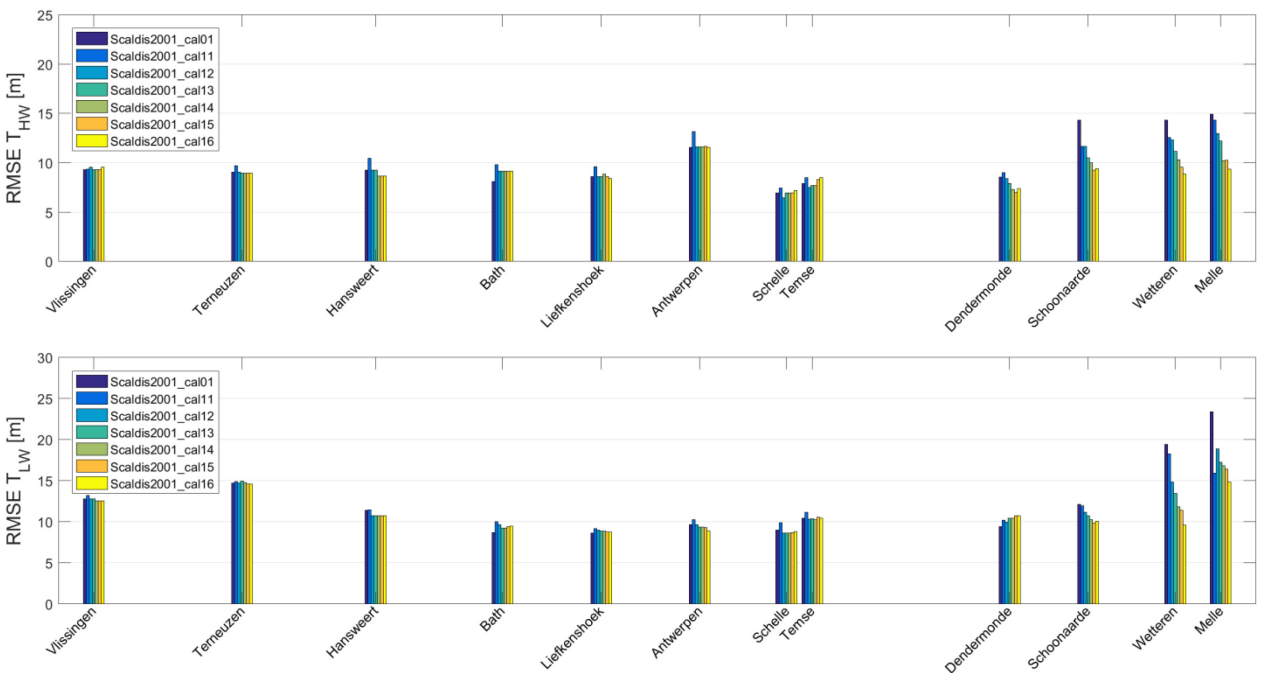


Figure 92 – HWL RMSE (top) and LWL RMSE (bottom) for calibration runs cal01 and cal11-cal16 with the 2013 model.

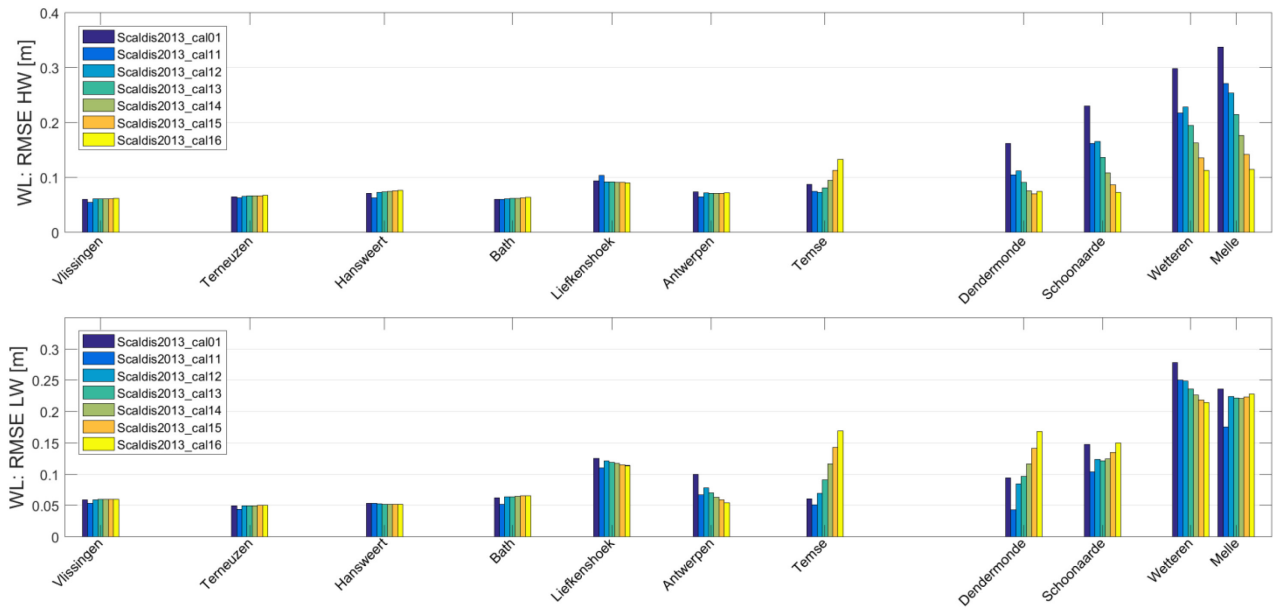
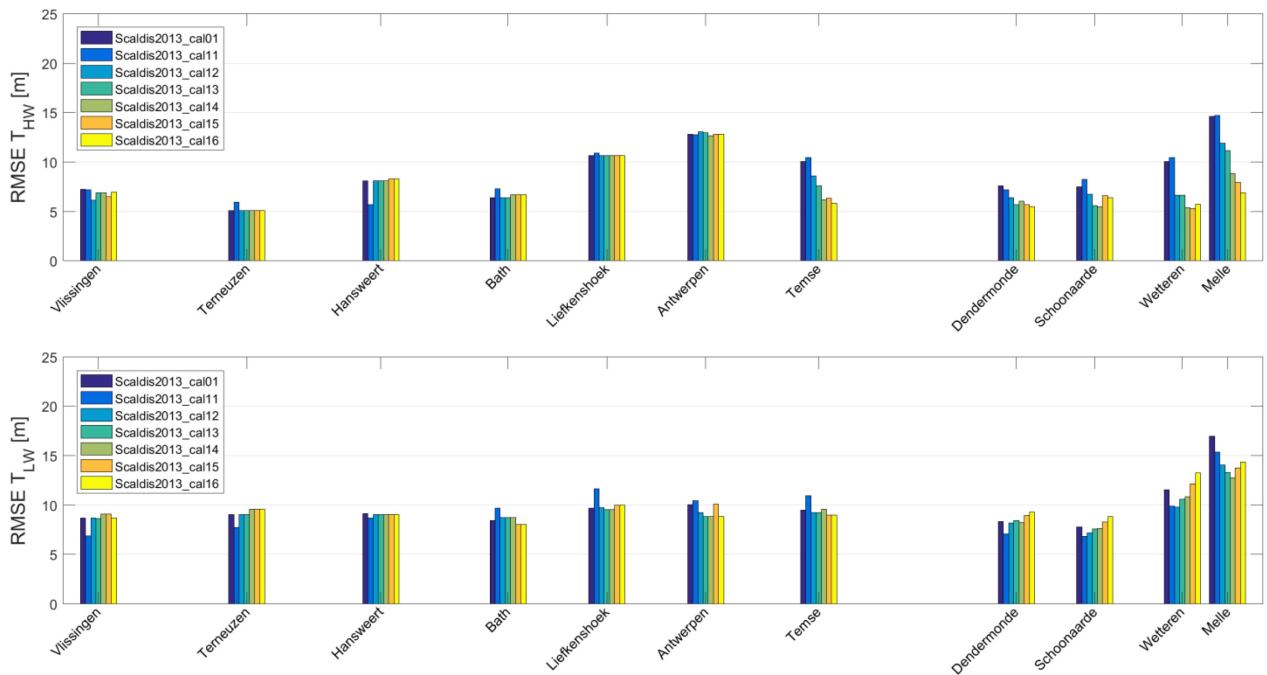


Figure 93 – THW RMSE (top) and TLW RMSE (bottom) for calibration runs cal01 and cal11-cal16 with the 2013 model.



### Calibration runs for Upper Sea Scheldt section (cal21, cal22, cal23, cal24 and cal25)

See Table 9 for an overview of the friction coefficients per estuarine section in each calibration run.

Figure 94 – HWL RMSE (top) and LWL RMSE (bottom) for calibration runs cal01, cal14 and cal21-cal25 with the 1930 model.

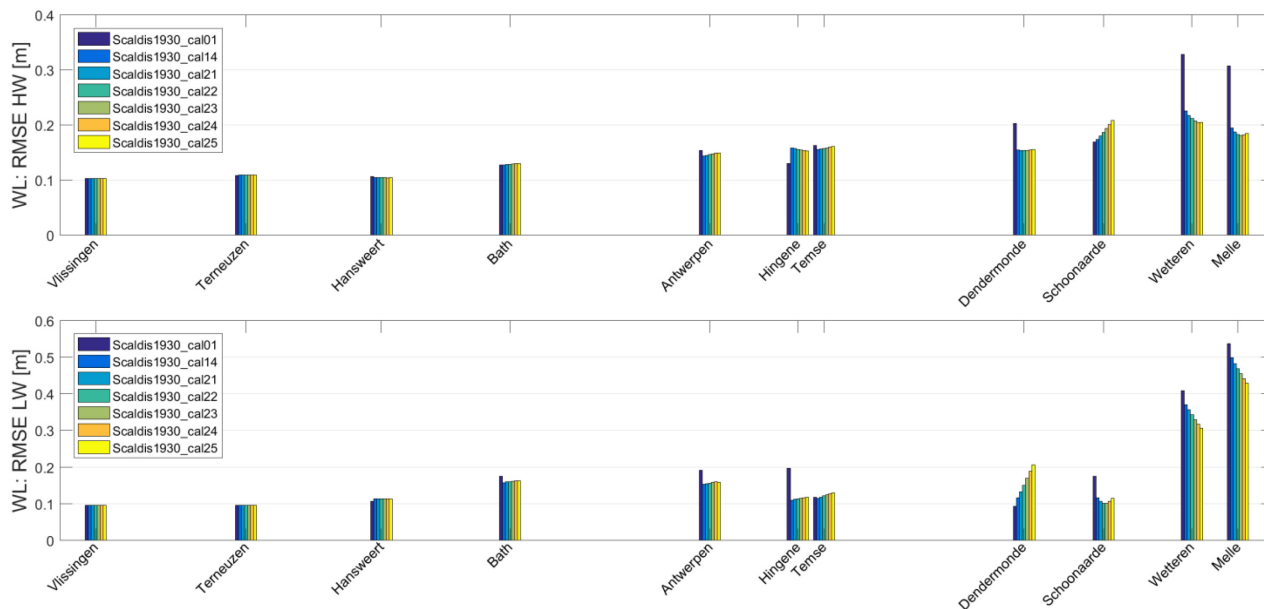


Figure 95 – THW RMSE (top) and TLW RMSE (bottom) for calibration runs cal01, cal14 and cal21-cal25 with the 1930 model.

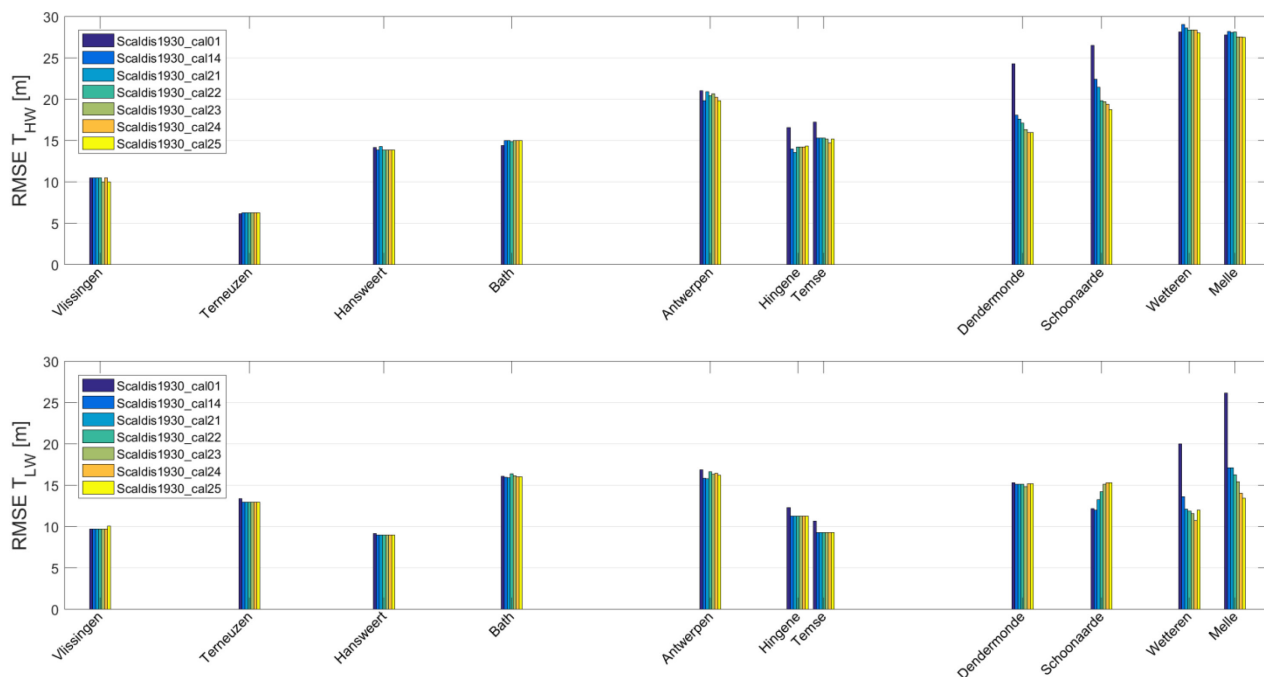


Figure 96 – HWL RMSE (top) and LWL RMSE (bottom) for calibration runs cal01, cal14 and cal21-cal25 with the 1960 model.

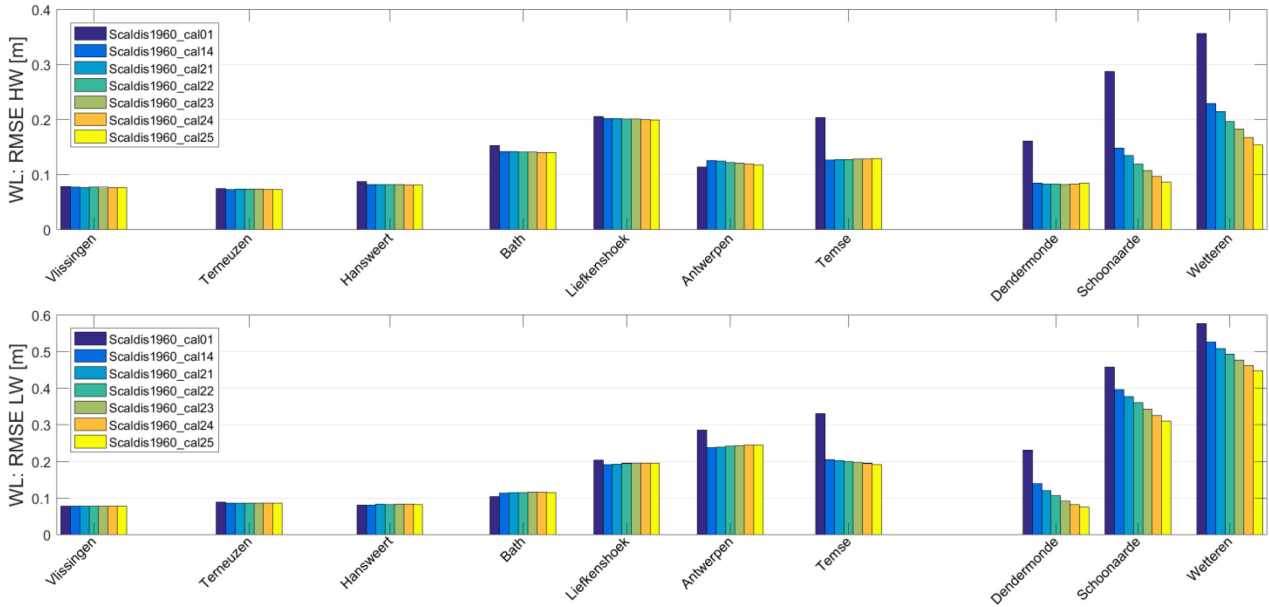


Figure 97 – THW RMSE (top) and TLW RMSE (bottom) for calibration runs cal01, cal14 and cal21-cal25 with the 1960 model.

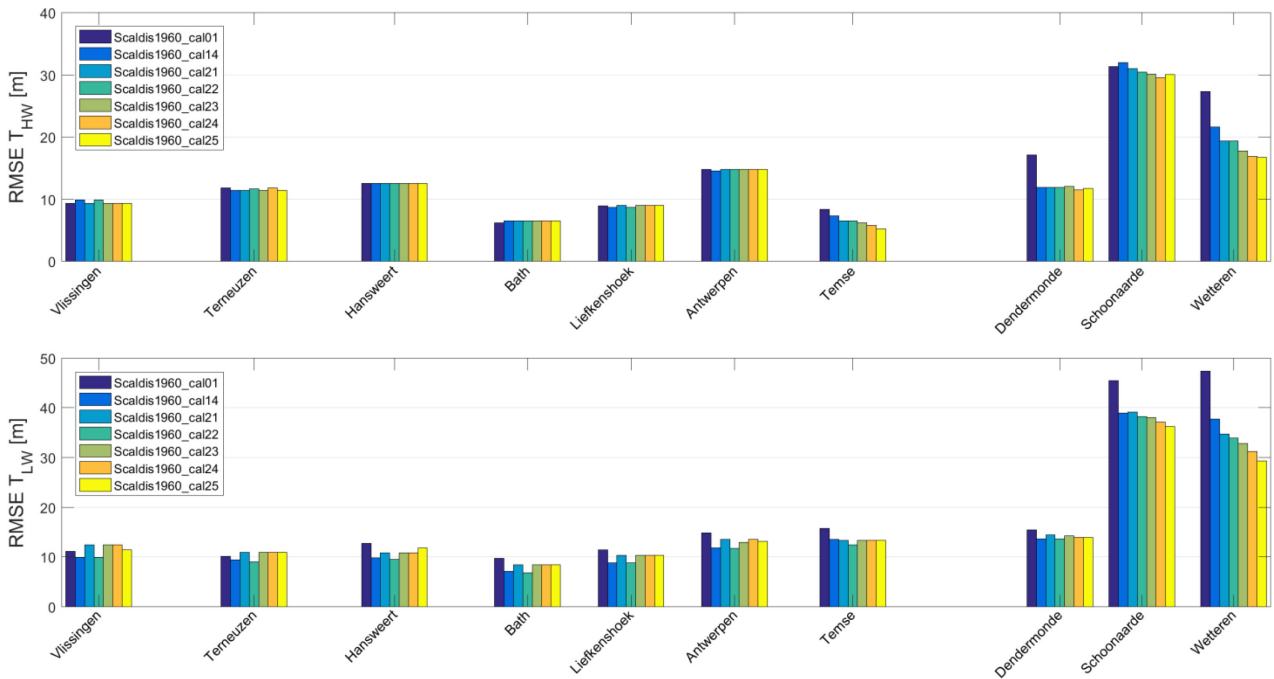


Figure 98 – HWL RMSE (top) and LWL RMSE (bottom) for calibration runs cal01, cal14 and cal21-cal25 with the 1980 model.

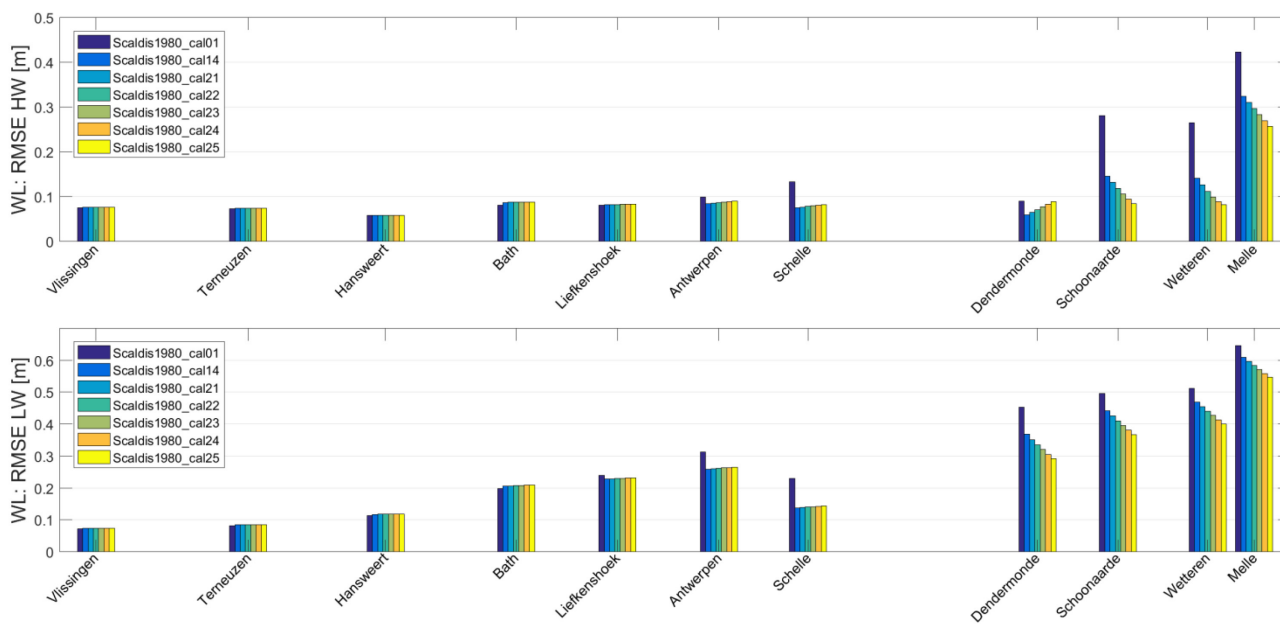


Figure 99 – THW RMSE (top) and TLW RMSE (bottom) for calibration runs cal01 and cal11-cal16 with the 1980 model.

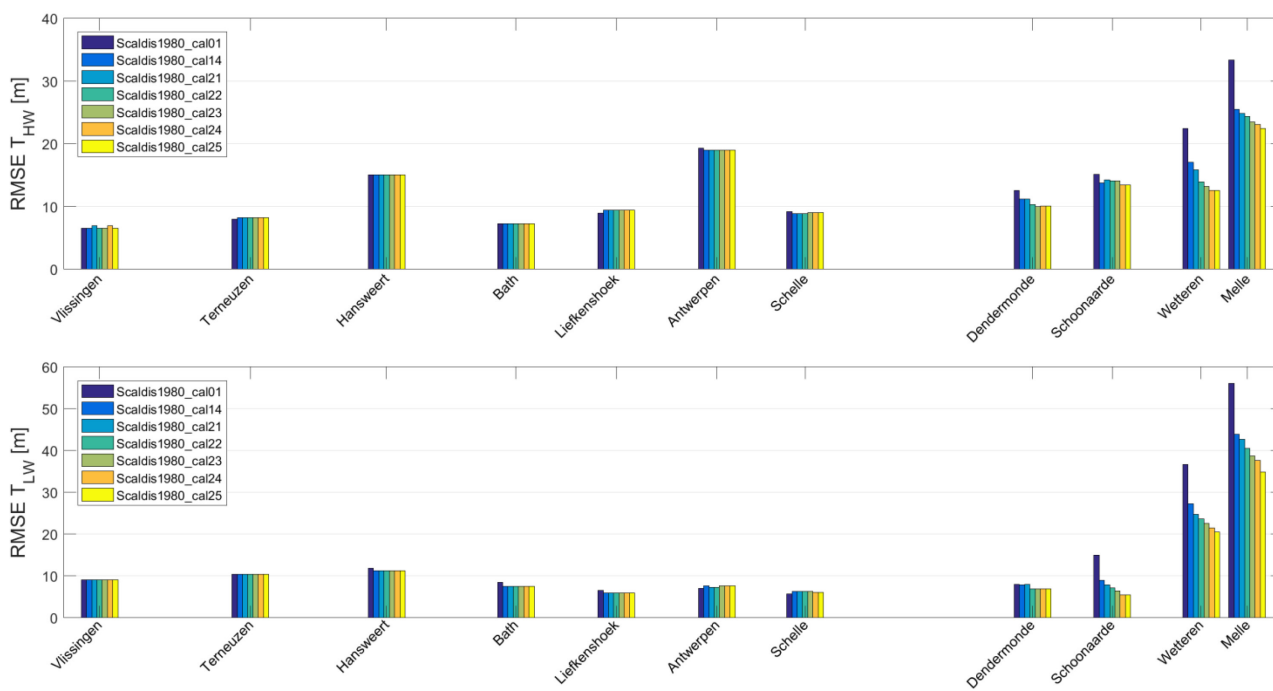


Figure 100 – HWL RMSE (top) and LWL RMSE (bottom) for calibration runs cal01, cal14 and cal21-cal25 with the 2001 model.

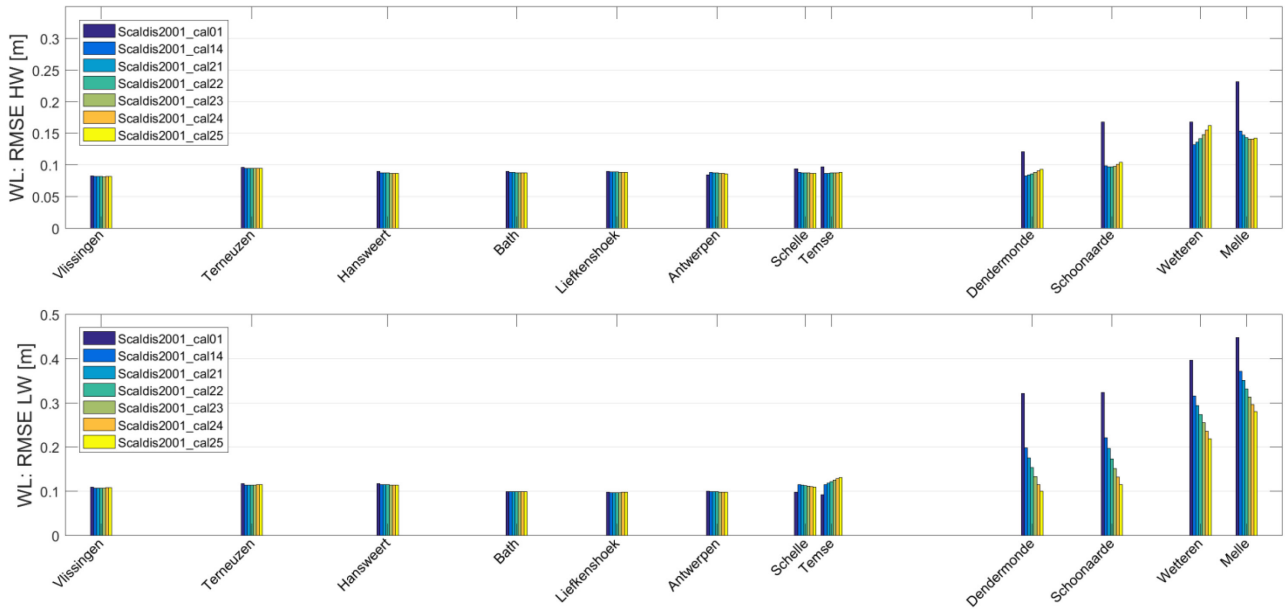


Figure 101 – THW RMSE (top) and TLW RMSE (bottom) for calibration runs cal01, cal14 and cal21-cal25 with the 2001 model.

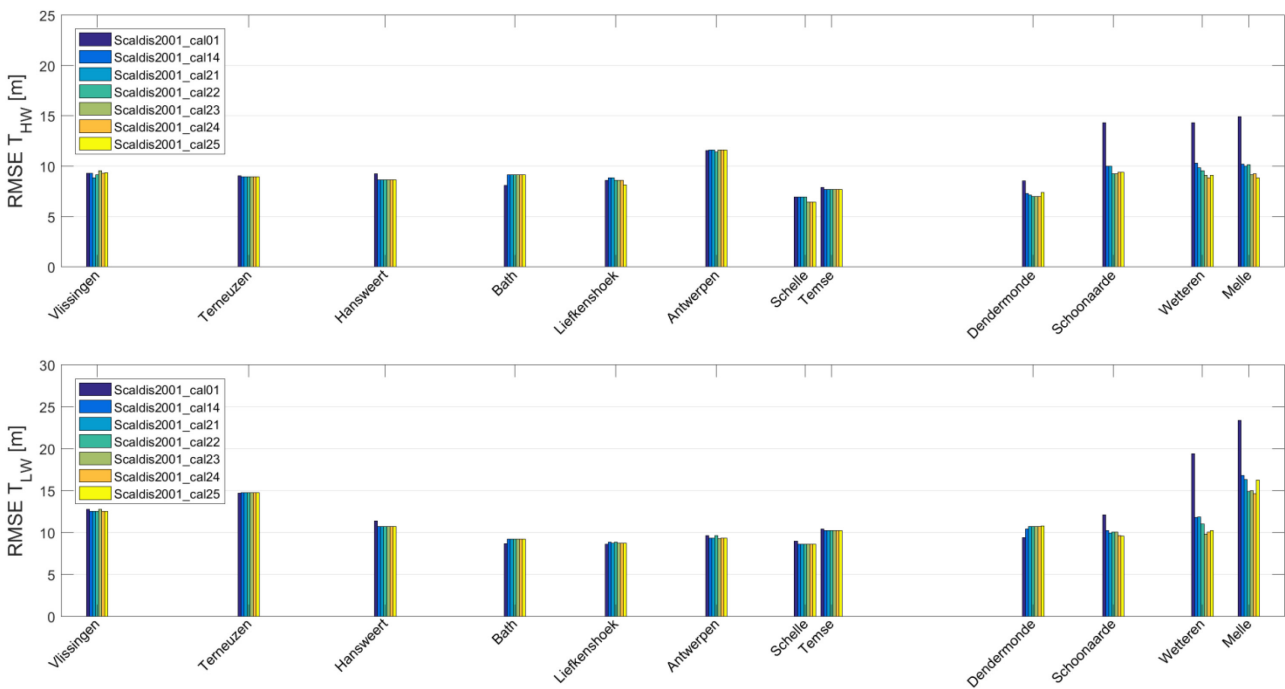


Figure 102 – HWL RMSE (top) and LWL RMSE (bottom) for calibration runs cal01, cal14 and cal21-cal25 with the 2013 model.

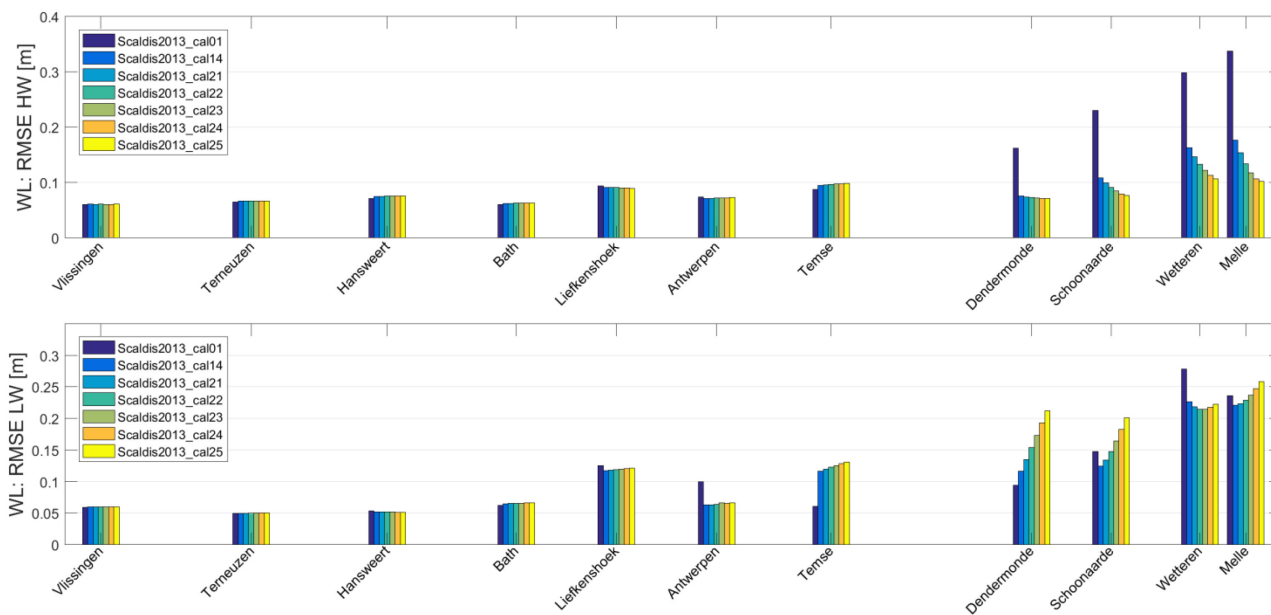
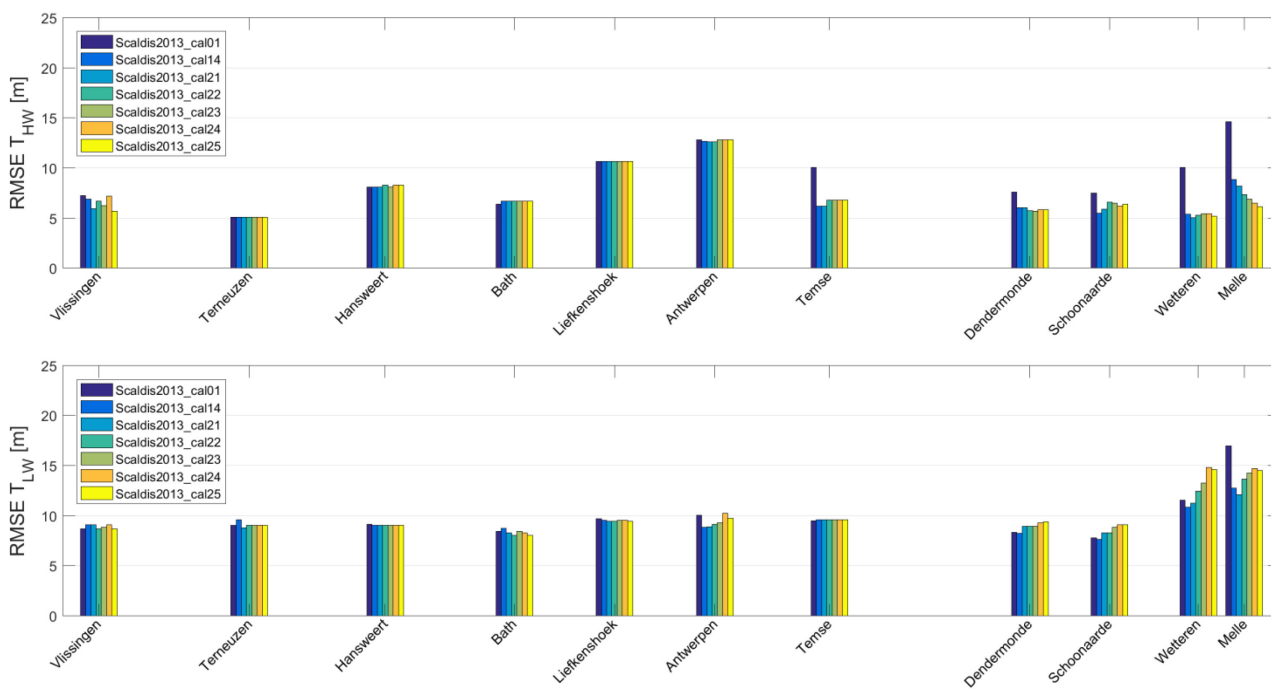


Figure 103 – THW RMSE (top) and TLW RMSE (bottom) for calibration runs cal01, cal14 and cal21-cal25 with the 2013 model.



## 10.7 Sensitivity analysis: viscosity coefficient

A brief explanation of the implementation of horizontal and vertical viscosity in TELEMAC-3D is given below (after Smolders et al., 2016), after which the sensitivity runs are described and their results are discussed.

For more detailed information regarding the selection of the turbulence models for the Scaldis3D model, we refer to Smolders et al. (2016).

### Vertical turbulence model

The vertical diffusivity of velocities or vertical turbulent viscosity is automatically computed by TELEMAC-3D by means of the selected mixing length model. The mixing length model expresses the turbulent viscosity as a function of the mean velocity gradient and the mixing length (Prandtl's theory) (EDF-R&D, 2013). For the 3D Scaldis model, the Nezu and Nakagawa mixing length model is selected (Smolders et al., 2016), in which the vertical turbulent viscosity is calculated as follows:

$$v_t = k u^* z \left(1 - \frac{z}{h}\right)$$

- $v_t$       turbulent viscosity;
- $k$         von Karman parameter (equal to 0.41);
- $u^*$      the shear velocity;
- $z$         the distance from the bed;
- $h$         water depth.

In TELEMAC-3D, the calculated turbulent viscosity is then added to the laminar viscosity ( $v_{tot} = v_t + v_l$ ) specified in the simulation's input file as the "Coefficient for vertical diffusion of velocities" (i.e.,  $v_l$ ). The impact of this latter coefficient is assessed in the sensitivity runs in this section.

### Horizontal turbulence model

For the 3D Scaldis model, the Smagorinsky horizontal turbulence model is used. This scheme is particularly recommended in the presence of a highly non-linear flow (EDF-R&D, 2013). The Smagorinsky model can be categorized as a sub-grid turbulence model. The horizontal turbulent viscosity in the Smagorinsky model is deduced as follows (Hervouet, 2007):

$$v_t = C_s^2 \Delta^2 \sqrt{2D_{ij}D_{ij}}$$

with:  $D_{ij} = \frac{1}{2} \left( \frac{\partial \bar{U}_i}{\partial x_j} + \frac{\partial \bar{U}_j}{\partial x_i} \right)$

- $v_t$       turbulent viscosity;
- $C_s$      a dimensionless coefficient (hardcoded as  $C_s = 0.1$  in the TELEMAC-3D routines);
- $\Delta$      the mesh size derived in 2D or 3D from the surface or from the volume of the elements;
- $D_{ij}$     the strain rate tensor, which involves velocity gradients.

As for the vertical viscosity, the turbulent viscosity calculated in the Smagorinsky formula is added to the laminar viscosity ( $v_l$ ), which is now defined by the "Coefficient for horizontal diffusion of velocities" specified in the TELEMAC-3D input file. The impact of this latter coefficient is again assessed in the sensitivity runs in this Appendix.

## Numerical diffusion

In addition to the above-described diffusion as a result of turbulent and laminar viscosity, numerical diffusion may also affect the simulation results. Numerical diffusion is an "uncontrolled" diffusion that is automatically introduced in the calculation due to the coarseness of the mesh and the numerical scheme that is used. In a 1Dh model, the numerical diffusion can be estimated by  $U \cdot DX/2$ , while this formula only gives an order of magnitude for a 3D case. In general, the effect of the artificial diffusion coefficients given in the user input file (i.e., imposed laminar viscosity) is only significant if the imposed coefficients are large compared to the numerical diffusion. Similarly, the effect of the computed turbulent viscosity is only significant if the turbulent viscosity is large compared to the numerical diffusion.

## Overview of sensitivity runs

Four model simulations (sa31-sa34) are performed in addition to the calibrated model simulation (cal25). The coefficient for diffusion of horizontal velocities and the coefficient for diffusion of vertical velocities (i.e., the horizontal and vertical laminar viscosity) are simultaneously varied between  $10^{-6}$  and 1.0 in these simulations (see Table 14). All other model settings and parameters are kept equal to the cal25 run. The sensitivity runs are only performed for the 1930 model, as this historical model performs fairly well up until Dendermonde and is most strongly influenced by shallow and intertidal areas in the most upstream part of the estuary where grid sizes are smallest.

Table 14 – Overview of model simulations for sensitivity analysis of diffusion coefficients.

Simulation	Coefficient for vertical diffusion of velocities	Coefficient for horizontal diffusion of velocities
cal25	0.01	0.01
sa31	$10^{-6}$	$10^{-6}$
sa32	$10^{-4}$	$10^{-4}$
sa33	0.1	0.1
sa34	1	1

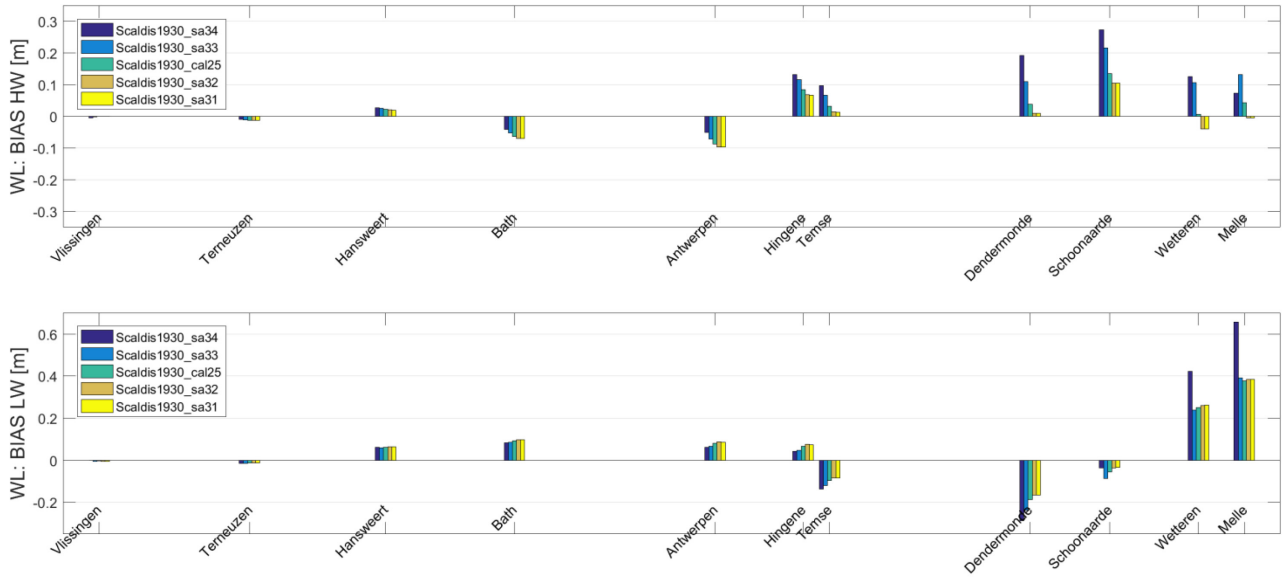
## Results and discussion

The effect of the user-defined velocity diffusivity coefficient (or viscosity coefficient) on high and low water levels along the estuary is depicted in Figure 104. Its impact appears to be rather small in the Western Scheldt where differences between the sensitivity runs remain within a few centimeters. However, differences are larger further upstream and are most pronounced in the Upper Sea Scheldt. In particular, using high horizontal and vertical diffusion coefficients of 1.0 leads to an increase in modelled high water levels of up to 0.15 m in Schoonaarde compared to the cal25 run with diffusion coefficients of 0.01. The effect on low water levels is more variable. Using high diffusion coefficients of 1.0 leads to reduced low water levels up until Dendermonde, whereas modelled low water levels increase strongly by up to 0.20 m at Wetteren and Melle. Lowering the horizontal and vertical diffusion coefficients to  $10^{-4}$  or  $10^{-6}$  (i.e., equal to the molecular viscosity) has limited effects for the modelled low and high waters. In these cases, the artificial diffusion or imposed laminar viscosity is probably small compared to the computed turbulent viscosity and numerical diffusion.

Overall, it can be concluded that changing the coefficient for vertical diffusion of velocities or the coefficient for horizontal diffusion of velocities does not lead to a better model performance in the most upstream part of the Upper Sea Scheldt. Using higher diffusion coefficients appears to increase both high-

and low water levels in this section of the estuary, but it does not lead to the increase in tidal range needed to improve the model performance. Therefore, it seems most appropriate to use lower diffusion coefficients of  $10^{-6}$  to  $10^{-2}$ , as these coefficients do not impose any additional or unwanted artificial diffusion to the model simulation.

Figure 104 – Impact of variations in the viscosity coefficient on HWL BIAS (top) and LWL BIAS (bottom) for calibration runs cal25 and sa31-sa34 with the 1930 model.



DEPARTMENT **MOBILITY & PUBLIC WORKS**  
Flanders hydraulics Research

Berchemlei 115, 2140 Antwerp

**T** +32 (0)3 224 60 35

**F** +32 (0)3 224 60 36

[waterbouwkundiglabo@vlaanderen.be](mailto:waterbouwkundiglabo@vlaanderen.be)

[www.flandershydraulicsresearch.be](http://www.flandershydraulicsresearch.be)